THE ASTROPHYSICAL JOURNAL, 453:100–138, 1995 November 1

THE INTERACTION BETWEEN SPIRAL GALAXIES IC 2163 AND NGC 2207. I. OBSERVATIONS

DEBRA MELOY ELMEGREEN,[1] MICHELE KAUFMAN,[2] ELIAS BRINKS,[3]
BRUCE G. ELMEGREEN,[4] AND MARIA SUNDIN[5]
Received 1994 November 28; accepted 1995 May 2

ABSTRACT

High-resolution H I observations taken at the VLA of the interacting pair of galaxies NGC 2207 and IC 2163 are presented, compared with optical and radio continuum images, and analyzed with detailed computer simulations (in Paper II) in order to determine the orbits and study the effects of in-plane and out-of-plane tidal forcing during a recent, close, nonmerging encounter between galaxies of comparable mass.

IC 2163 has an ocular shape (an eye-shaped central oval with a sharp apex at each end) and a double-parallel arm structure on the side opposite NGC 2207. Our observations of IC 2163 find (1) an intrinsically oval shape to the disk, (2) large streaming motions along the oval, (3) H I tidal arms located symmetrically on opposite sides of the nucleus (even though one side is obscured by NGC 2207 at optical wavelengths), and (4) a line-of-sight velocity difference of 70–100 km s^{-1} between the two components of the double-parallel arm. Optical surface photometry of IC 2163 indicates that most of the stars in the interarm region have been cleared away and put into the central oval and tidal arms. The kinematic and structural anomalies of IC 2163 are consistent with the predictions of *N*-body galaxy encounter simulations if NGC 2207 moved approximately in the plane of IC 2163 in a prograde sense.

The companion, NGC 2207, shows different types of disturbances. The main body of H I gas in NGC 2207 forms a broad, clumpy ring that contains relatively thin stellar arms and corresponds to a plateau in the radial distribution of optical light. The most massive H I clouds in the ring do not always coincide with the stellar arms. The ring is broken in the south, and a filamentary pool of H I extends 40 kpc farther south. The velocity field in the main disk of NGC 2207 is highly distorted with isovelocity contours that are shaped like an open trailing spiral, and the H I line profiles in this region are very broad with Gaussian dispersions of 40–50 km s^{-1}. The kinematic disturbances in NGC 2207 suggest that the main tidal force on NGC 2207 was perpendicular to its disk. The companion side of the H I ring is unusually bright in $\lambda 20$ cm radio continuum emission, perhaps indicating a shock front.

There is no significant excess of star formation in these galaxies, but there are several 10^8 $M_\odot$ gas clouds in each disk, some of which may eventually become detached dwarf galaxies.

Subject headings: galaxies: individual (IC 2163, NGC 2207) — galaxies: interactions — galaxies: kinematics and dynamics — galaxies: structure — radio continuum: galaxies

1. INTRODUCTION

The spiral galaxies IC 2163 and NGC 2207, shown in Figure 1 (Plate 1), are involved in a close tidal encounter. They partially overlap along the line of sight and have nearly the same systemic velocity. IC 2163, in the east, has an *ocular* shape (an eye-shaped central oval with a sharp apex at each end), intense star formation along the eyelid regions, and a double-parallel arm structure on the side opposite the companion, NGC 2207. In *N*-body simulations by Elmegreen et al. (1991, hereafter ESES; see also Struck-Marcell 1990; Sundin 1993; Donner, Engstrom, & Sundelius 1991), this type of morphology arises as a transient phase when a galaxy disk is sufficiently perturbed by a companion galaxy moving in a prograde orbit that lies within a few degrees of the plane of the disk. In such simulations, the perturbed galaxy first forms tidal arms located symmetrically on opposite sides of the disk, and then the ocular morphology develops as stars and gas from the companion side of the galaxy stream around on elliptical orbits toward the opposite arm. Angular momentum conservation bends this stream outward when it reaches the other arm, resulting in a double arm structure on the side opposite the companion. The ocular plus double-parallel arm morphology occurs during the first half-rotation after closest approach; the structure subsequently mixes and disappears.

Figure 2 shows a diagram (from ESES) of a typical ocular galaxy. The component of the double arm that continues smoothly from the inner oval is the original tidal tail; it has a symmetric counterpart on the other side of the galaxy. The other component (the upper component on the left in Fig. 2) is the stream of tidally perturbed stars and gas from the companion side. The simulations in ESES predict large streaming motions around the oval and a velocity difference of 50 to 100 km s^{-1} between the two components of the double arm. Such star-stream structures are *caustics* (Struck-Marcell 1990; Donner et al. 1991).

We observed the galaxy pair IC 2163/NGC 2207 in H I with the VLA in order to look for the predicted streaming motion on the oval and the velocity jump between the two components of the double arm. Few galaxies have such a clean ocular shape

[1] Vassar College Observatory, Poughkeepsie, NY 12601.
[2] Department of Physics, Ohio State University, 174 West 18th Avenue, Columbus, OH 43210.
[3] National Radio Astronomy Observatory, P.O. Box O, Socorro, NM 87801. (The National Radio Astronomy Observatory is operated by Associated Universities, Inc., under cooperative agreement with the National Science Foundation.)
[4] IBM Research Division, T. J. Watson Research Center, P.O. Box 218, Yorktown Heights, NY 10598.
[5] Department of Astronomy/Astrophysics, Chalmers University of Technology, S-412 96 Göteborg, Sweden.

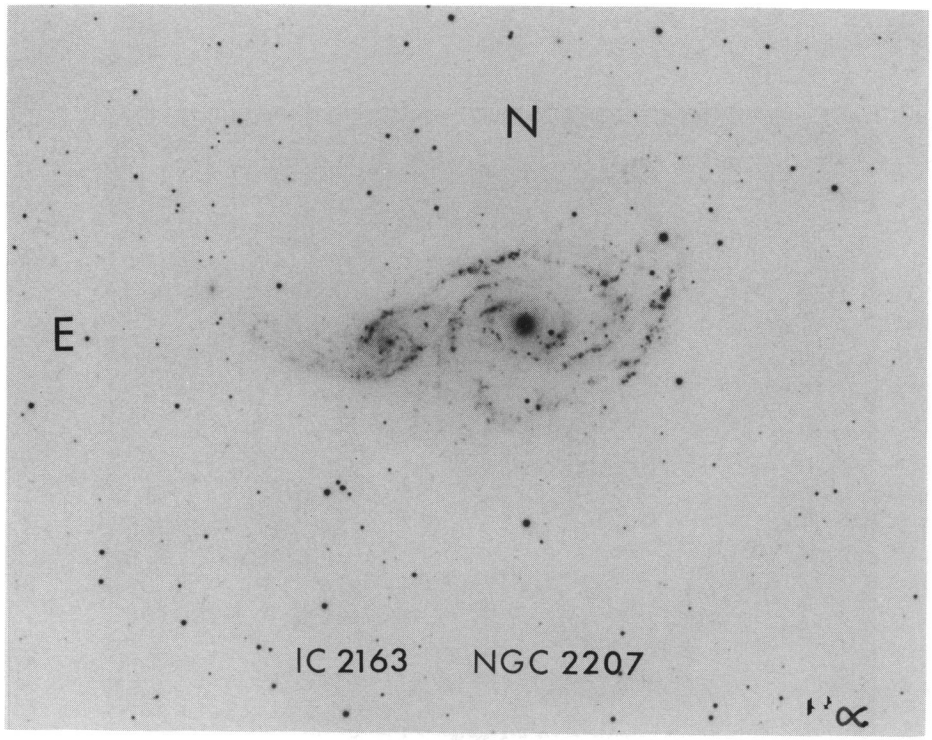

FIG. 1*b*

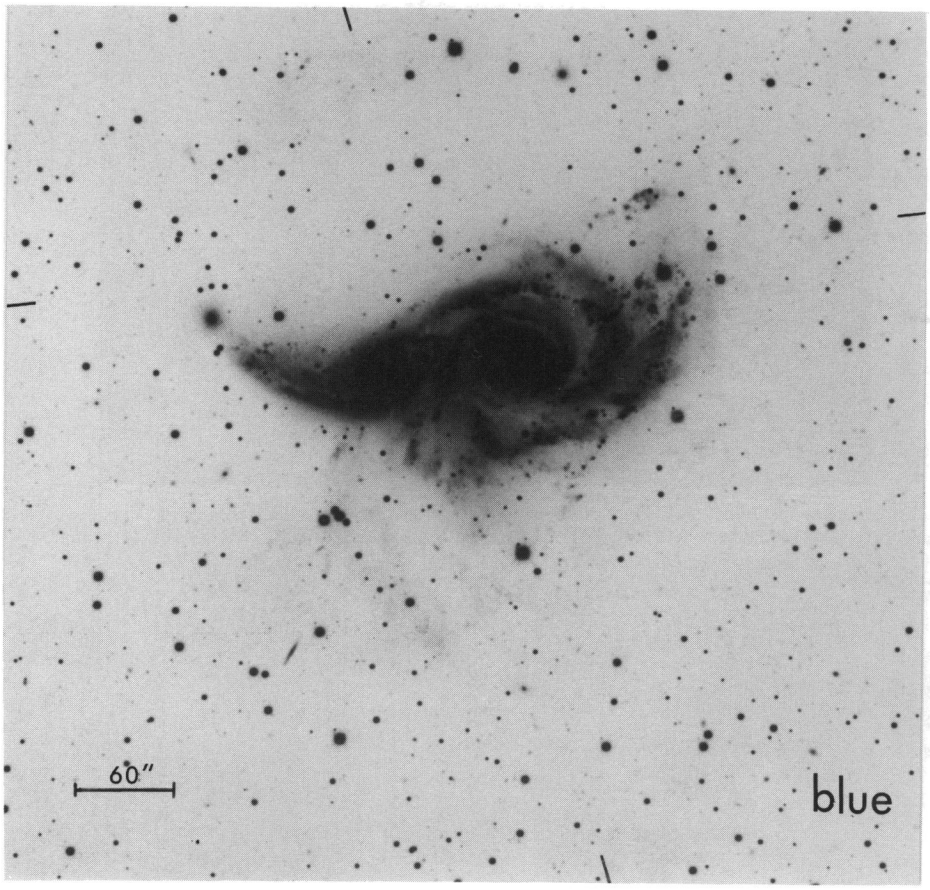

FIG. 1*c*

ELMEGREEN et al. (see 453, 100–101)

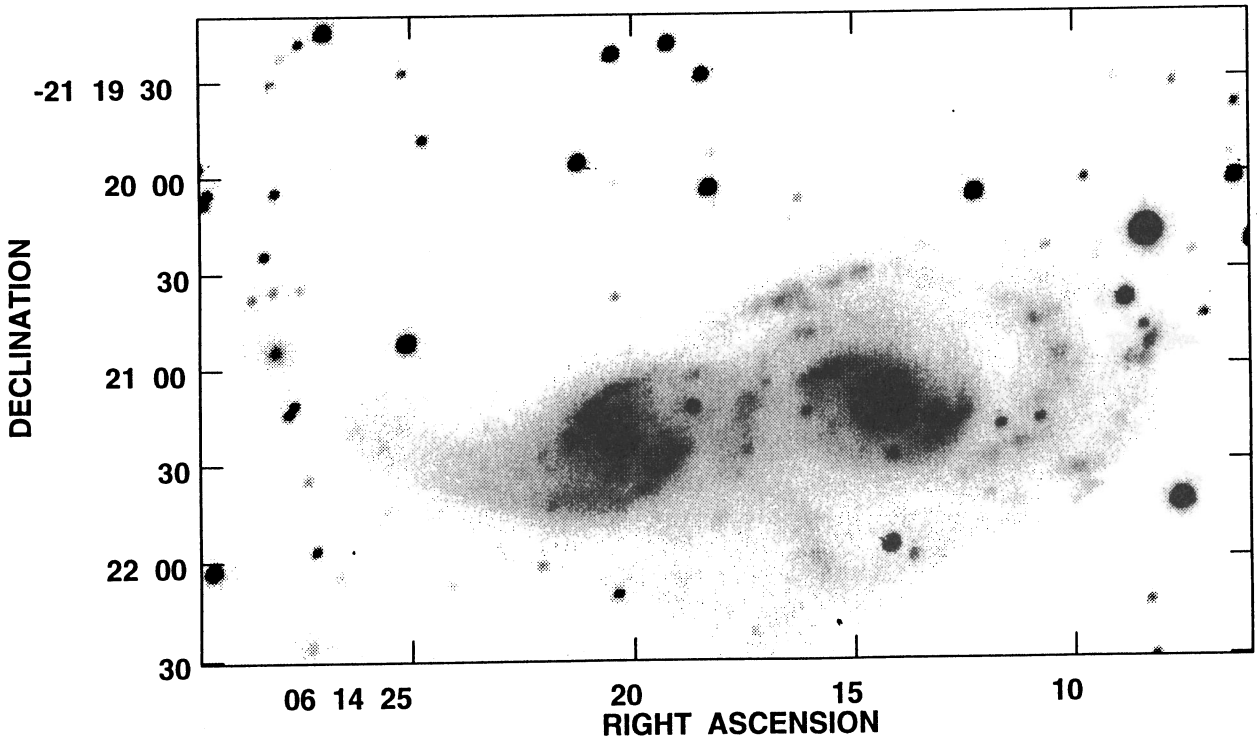

FIG. 1*a*

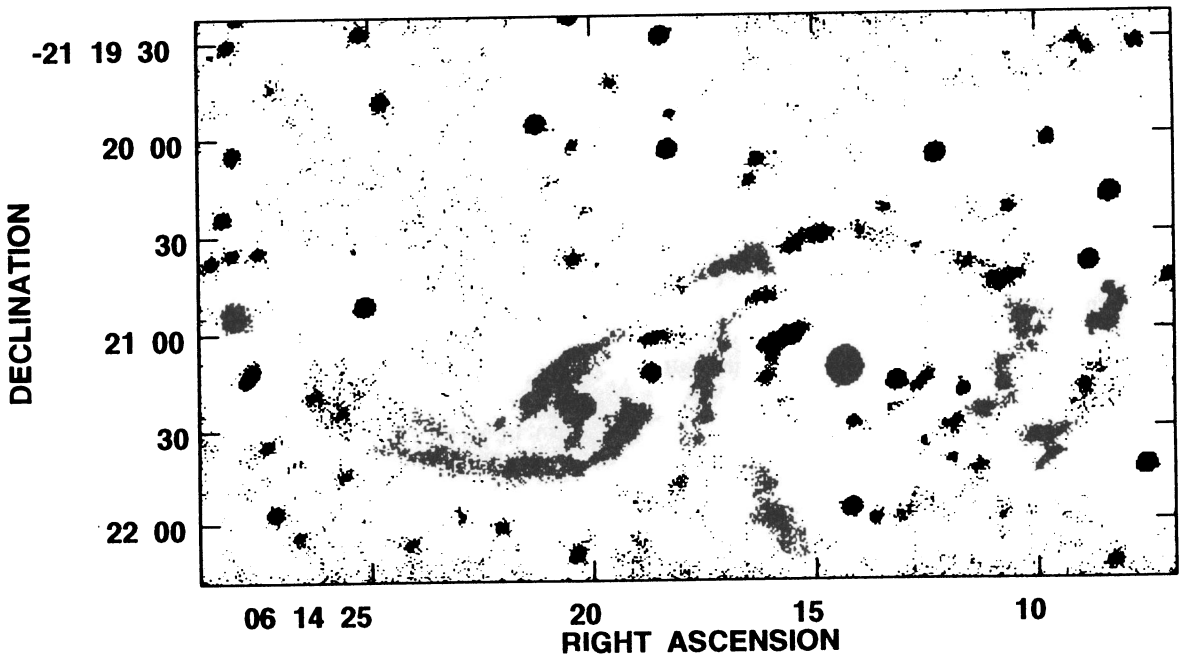

FIG. 1*d*

FIG. 1.—Optical images of IC 2163 (*left*) and NGC 2207 (*right*): (*a*) *R*-band image from H.-J. Deeg; (*b*) Hα photograph from Rubin & Ford (1983); (*c*) Blue-band photograph from V. Rubin (see Plate 1 for [*b*] and [*c*]); (*d*) unsharp-masked version of (*a*) that illustrates the double-parallel arm in the east of IC 2163 (*left*).

as IC 2163 (see list in ESES), so it was an obvious first choice. The kinematic and morphological data were then used to study the effects of tidal forcing on both galaxies. The ocular morphology makes it relatively easy to deduce the orbits of the two galaxies because this structure generally occurs soon after a prograde collision that has a strong in-plane component of the tidal force.

Our most useful H I data have a velocity resolution of 5.25 km s^{-1} and an angular resolution of 13″.5 × 12″, which, at an adopted distance of 35 Mpc (see below), corresponds to 2.3 × 2.0 kpc. The predicted streaming motions on the oval and the large velocity difference between the two components of the double arm in IC 2163 are easily seen in these data. Although the tidal arm on the companion (western) side of the

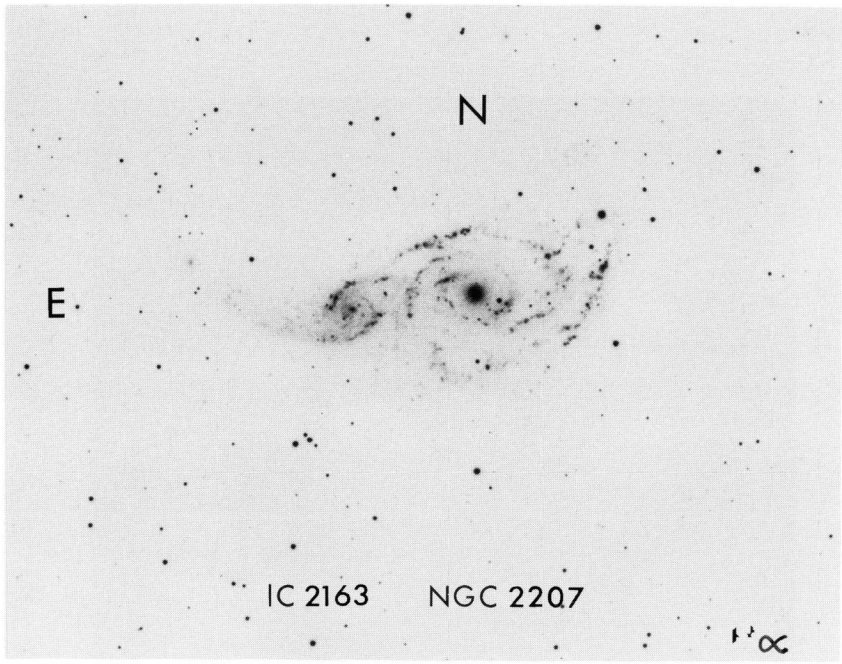

FIG. 1*b*

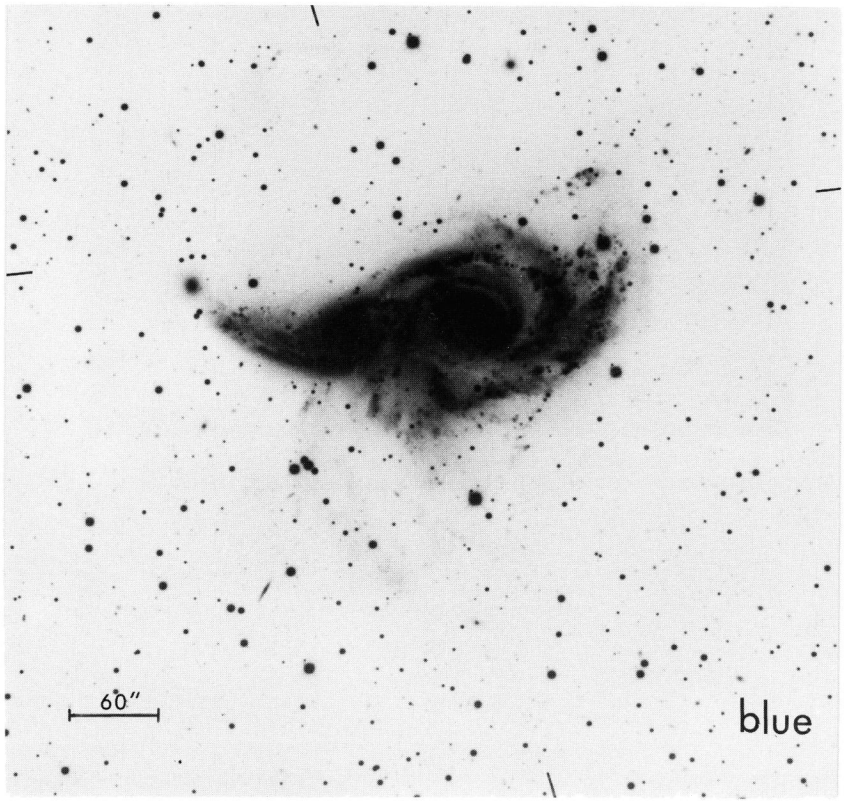

FIG. 1*c*

ELMEGREEN et al. (see 453, 100–101)

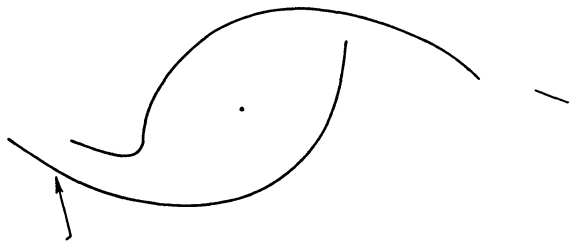

FIG. 2.—Schematic diagram of an ocular galaxy showing the first response of a galactic disk to a companion that moves in the plane of the disk in the prograde sense (from ESES). The companion is at the position of the line on the right.

ocular is obscured optically by NGC 2207, we find H I tidal arms on both sides of IC 2163, as predicted by the models.

The H I data are also compared with CCD images in *B* and *R* bands taken by Hans-Jörg Deeg. The *B*- and *R*-band images show that nearly all the stars have been cleared out of the interarm regions of IC 2163 by the interaction and put into the central oval and the arms. This is also consistent with the model.

The companion galaxy, NGC 2207, shows no peculiar structure in short-exposure optical photographs (see Fig. 1*a*); it has a normal spiral pattern and a small, weak central bar. A deep *B*-band exposure (Fig. 1*c*) reveals an extended, asymmetric outer disk with faint optical streamers in the south. This southern extension, also visible in H I, along with a smaller, faint optical counterpart in the north (Fig. 1*c*), suggests that short-range tidal forces are stretching the disk asymmetrically. The H I kinematics in the main disk of NGC 2207 also indicate that strong tidal forces are present. The isovelocity contours in NGC 2207 have an S-shaped distortion with unusually large velocity dispersions. Such a distortion is the signature of a large-scale warp (Paper II).

We suggest that the differences in morphology and velocity structures of these two galaxies result from a difference in the orientation of the tidal forces relative to the disks. In IC 2163, these forces are primarily in the plane, where they amplify by disk self-gravity into giant spirals and oval distortions. In NGC 2207, they are primarily perpendicular to the plane, and there is no analogous amplifier in this direction. Our simulations in Paper II show that such perpendicular perturbations propagate inward in the form of an open spiral of z displacement and then propagate outward as a tight spiral in z. By fitting the observed velocity field, we find that NGC 2207 now has the inward propagating spiral of z displacement. The fits to the velocity field of NGC 2207 and to the ocular structure of IC 2163 give consistent relative orbits for the galaxies.

Both galaxies contain unusually massive H I clouds, with H I masses several times 10^8 $M_\odot$. Elmegreen, Kaufman, & Thomasson (1993) attribute these clouds to gravitational instabilities in the tidally agitated gas disks and suggest that some of them may eventually form independent dwarf galaxies.

In what follows, § 2 describes the optical morphology of this interacting pair; § 3, the H I observations and the VLA data reduction procedure; § 4, the H I properties of IC 2163; § 5, the H I properties of NGC 2207; § 6, the broadband optical surface photometry; and § 7, the radio continuum images and Hα velocities. Section 8 summarizes the observational results. Dynamical simulations of the galaxy interaction are then compared to the kinematic and morphological data in Paper II, along with a summary of the results from the models and the overall conclusions.

2. OPTICAL MORPHOLOGY OF IC 2163 AND NGC 2207

In this study we use the following optical images of IC 2163/NGC 2207 (see Fig. 1): (*a*) CCD images with 10 minute exposures in *B* and *R* bands taken by Hans-Jörg Deeg on 1990 October 16 at the 24″ Capilla Peak telescope in New Mexico, (*b*) an Hα plate from Rubin & Ford (1983), and (*c*) a blue-band plate with a 90 minute exposure obtained by Vera Rubin with the CTIO 4 m telescope in the early 1970s. Deeg, Rubin, and Ford have kindly made their observations available to us. The CCD has a 3.′5 × 5.′5 field. The seeing is estimated to be 3″, and the pixel size is 0.″658. Secondary standard field stars (from Condon 1983) with positions derived from SAO standards were used to determine the absolute coordinate systems of the optical images and to register the CCD and the radio images to the same coordinate grid.

Table 1 lists some basic parameters of the galaxies taken from the Third Reference Catalogue (de Vaucouleurs et al. 1991, hereafter RC3) and the NASA Extragalactic Database (NED). We adopted $H_0 = 75$ km s^{-1} Mpc^{-1}, which leads to a distance of 35 Mpc; then 1″ = 170 pc.

The ocular structure of IC 2163 is visible in Figure 1 in the *R*-band and the Hα images. The eastern arm of IC 2163 is broad and appears split into two components, as illustrated in Figure 2. Bright H II regions delineate the eyelid regions while fainter star-forming regions lie along the double-parallel arm. The two components of the double arm are separated in declination by 6″ to 12″ with a valley between. From cuts across the arm at fixed values of right ascension, we find that the average difference in *R*-band surface brightness between the northern ridge and the valley is 0.2 mag and between the southern ridge and the valley is 0.3 mag.

IC 2163 is classified as SB in RC3. The bar in IC 2163 is shown in Figure 3*a*, which displays an enlarged portion of the *R*-band image. The bar ends at 16″ distance from the nucleus, where it joins the eyelid of the oval, and has its major axis close to the isophotal minor axis of the eye-shaped oval (see values listed in Table 2). A prominent optical clump occurs on the eyelid at the northeastern end of the bar. From the *B* and *R*-band CCD images, we find that this clump is bluer than most of the eastern arm and thus is a region of enhanced star formation.

The spiral arm structure of NGC 2207, as seen in the CCD images and the Hα photograph, consists of two very bright,

TABLE 1

BASIC DATA ON IC 2163/NGC 2207

CHARACTERISTIC	GALAXY	
	IC 2163	NGC 2207
Morphological type	SB(rs)c pec	SAB(rs)bc pec
Right ascension (1950)	$6^h14^m20^s.0$	$6^h14^m14^s.4$
Declination (1950)	−21°21′24″	−21°21′14″
Isophotal major radius (R_{25})	1.51′	2.13′
Axis ratio	2.45	1.55
m_B	12.55	11.59
Corrected *B* magnitude, B_T^0	11.26	10.90
f(60 μm) (Jy)	14.6	
f(100 μm) (Jy)	38.0	
Distance	35 Mpc	

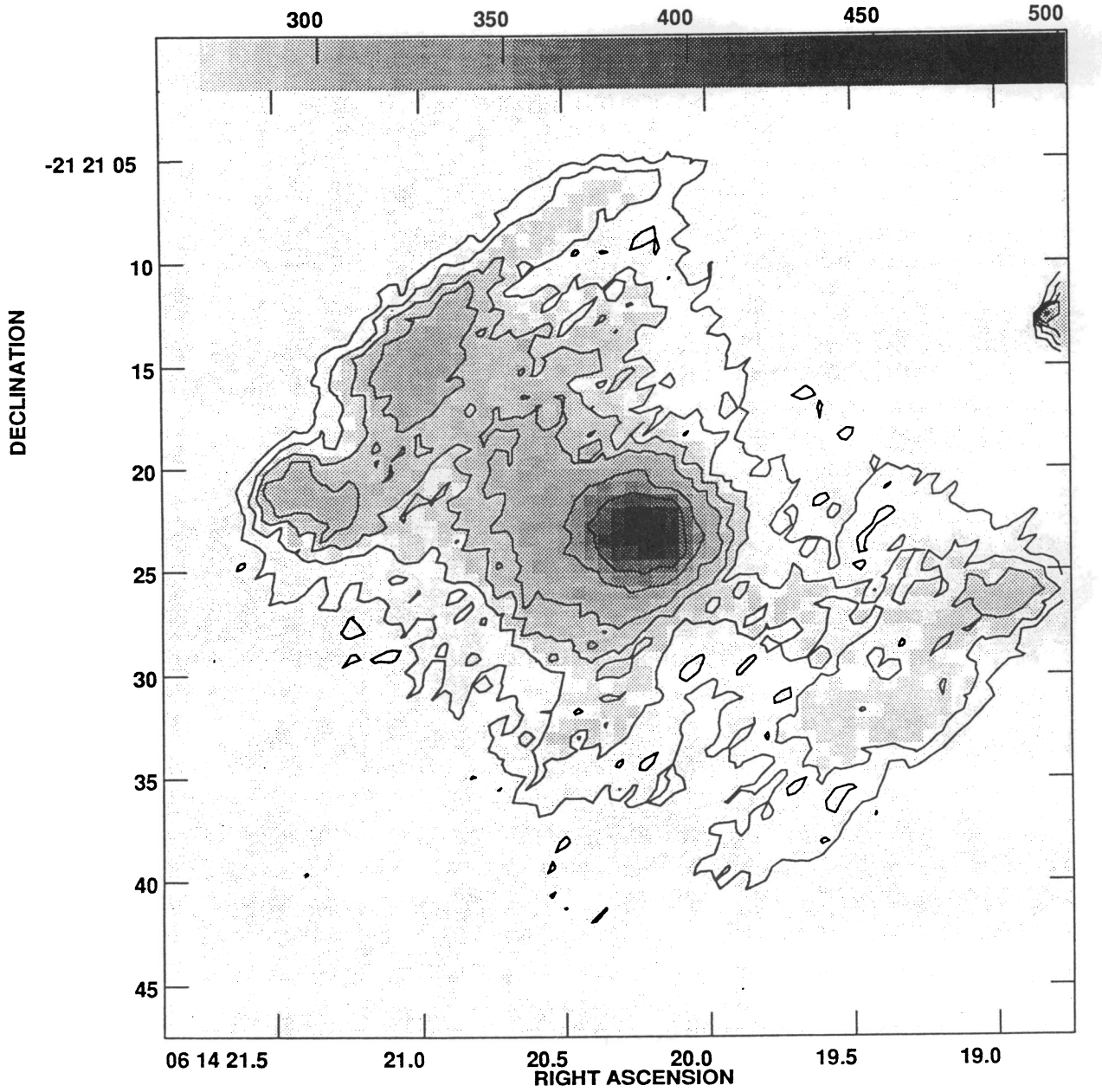

FIG. 3a

FIG. 3.—The inner bar/barlike regions for (*a*) IC 2163 and (*b*) NGC 2207 in the *R*-band image. Notice the optical clump at the northeastern end of the bar in IC 2163.

short spiral arm stubs that emerge from the nuclear region and two long grand-design spiral arms that dominate much of the main disk. The H II regions are particularly prominent in the northeastern part of the outer arm (nearest IC 2163) and in the westernmost outer arm. The dust lane from the easternmost arm of NGC 2207 crosses IC 2163 just south of its nucleus; this indicates that NGC 2207 is in front and overlaps the western part of IC 2163 (Wray 1988). Thus NGC 2207 may optically obscure a western tidal arm in IC 2163. In the deep *B* photograph there is a southern extension to NGC 2207, with long streamers that arc to the south nearly 3′ (30 kpc in the plane of the sky) beyond the brightest part of the disk. The easternmost southern streamer appears to be a continuation of the brighter easternmost optical arm. There are also several other southern streamers that branch off from the main spiral arms. The presence of faint wispy structures is consistent with the idea that this is tidally disturbed material. In the north, there is a faint extension of the westernmost main spiral arm ending in blue knots, which also appear faintly on the Hα image.

NGC 2207 is the larger and the more luminous of the two galaxies. Based on the values of m_B listed in RC3, it is 2.4 times brighter than IC 2163. The values of the "face-on" corrected magnitude B_T^0 in RC3 imply a luminosity ratio of only 1.4, but

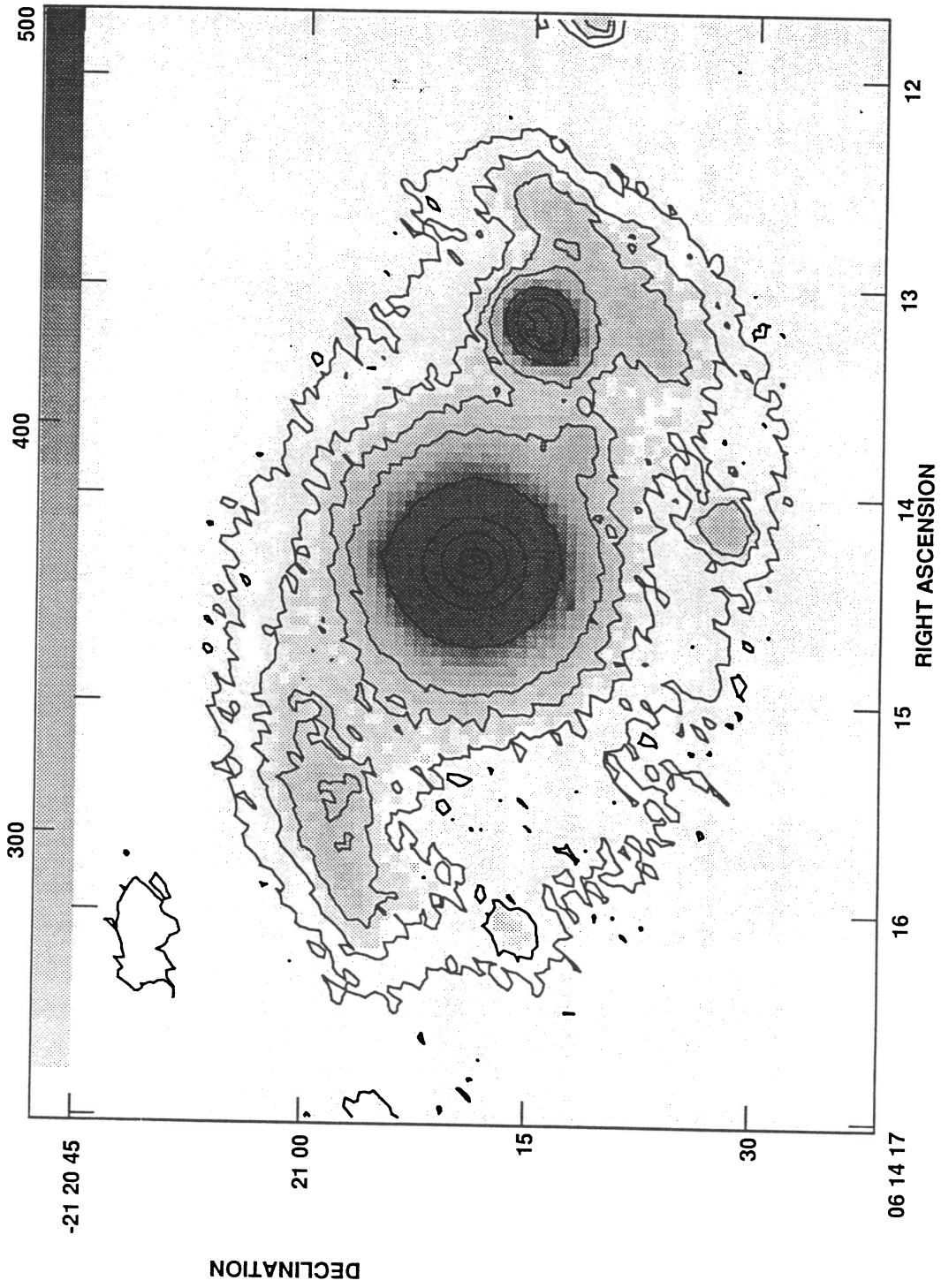

FIG. 3*b*

TABLE 2

ORIENTATION PARAMETERS AND SYSTEMIC VELOCITIES

Parameter	Value
IC 2163	
Systemic velocity (km s^{-1}):	
Nucleus (optical)	2756 ± 15
H I velocity field (minor axis)	2775 ± 10
Major axis of bar	52° ± 5°
Minor axis position angle of disk:	
Optical and H I isophotes on apparent oval	38° ± 3°
H I kinematic	155° ± 10°
Preferred position angle of projection line of nodes	65° ± 10°
Disk inclination from ocular model fits	40° ± 5°
NGC 2207	
Systemic velocity (km s^{-1}):	
Nucleus (optical)	2745 ± 15
H I kinematic minor axis in central region	2750 ± 20
Major axis of bar	65° ± 5°
H I kinematic minor axis position angle of disk:	
In the central region	60° ± 3°
At 80″ on the southwest side	95° ± 5°
Major axis position angle of disk:	
Optical isophotes of main disk	110° ± 7°
N(H I) isophotes on H I ring	100° ± 5°
H I kinematic (tilted-ring fit):	
North receding: varies over range	330°–342°
South approaching: varies over range	150°–177°
Outermost N(H I) contour:	
Northern side	330° ± 3°
Southern side	160° ± 5°
Preferred position angle of projection line of nodes	140° ± 5°
Inclination of central disk from model fits	35° ± 5°

their adopted internal extinction correction for IC 2163 is questionable because this is a disturbed galaxy and its inclination cannot be simply deduced from the isophotal minor to major axis ratio.

NGC 2207 is classified as SAB in RC3. The barlike feature in NGC 2207 is shown in Figure 3*b*, which displays the nuclear region in detail in *R*-band. The major axis of the barlike feature is displaced about 45° from the photometric major axis of the central disk of NGC 2207 (see values listed in Table 2). The barlike feature in NGC 2207 ends at 28″ = 0.22 R_{25}, where R_{25} is the radius at which the blue surface brightness reaches 25 mag arcsec^{-2}. This bar is relatively small compared to the structures we discuss in this galaxy.

Although NGC 2207/IC 2163 is an interacting system, it is not currently undergoing a starburst. From the values of the *IRAS* flux densities in Table 1, the combined system has a 60 μm to 100 μm flux density ratio of 0.38, which is typical for normal galaxies (see Bothun, Lonsdale, & Rice 1989), and a FIR luminosity equal to $3.6 \times 10^{10}\ L_{\odot}$. The combined system has the same value of f_{60}/f_{100} as M51, twice the FIR luminosity of M51, and 3.5 times the blue luminosity of M51. Since NGC 2207 is a large galaxy with $R_{25} = 22$ kpc, the system is not overluminous. However, the bright patches of star formation along the eyelid of IC 2163 are unusual.

There is possibly a third galaxy in this system: an apparent dwarf elliptical galaxy with a red color and an unknown redshift (not detected in our H I data) at $\alpha = 6^{h}14^{m}28^{s}.014$, $\delta = -21°20'54''.26$, near the tip of the eastern tidal arm of IC 2163 in the deep *B*-band photograph in Figure 1. It is also visible in the other images and noted in the Southern Galaxy Catalogue (Corwin, de Vaucouleurs, & de Vaucouleurs 1985).

3. VLA H I OBSERVATIONS

3.1. *Observations and Data Reduction*

The VLA H I observations were made on 1990 October 11 in the hybrid CnB array, i.e., with an extended north arm to correct for the foreshortening due to the low declination of the source. The duration of the run was 7.5 hr. The observations were scheduled for the night to avoid solar interference during the current solar maximum and were performed under favorable weather conditions. In total, 6 hr were spent on the target, 40 minutes on the secondary calibrator 0607−157, and 20 minutes on 3C 48, which served as a flux standard and bandpass calibrator. We assumed a flux density of 16.17 Jy for 3C 48 on the Baars et al. (1977) scale and measured a flux density of 2.664 ± 0.005 Jy for source 0607−157. A summary of the observations is given in Table 3.

Our aim was to observe the interacting pair of galaxies at about 5 km s^{-1} velocity resolution. The velocity range over which H I emission is present is some 550 km s^{-1}, requiring a total bandwidth of at least 3 MHz. Since no single correlator mode accommodates these requirements, we chose a 4IF mode and used a highly nonstandard correlator configuration. As this is likely to be the first article describing this option, we feel it is justified to elaborate on some of the technical aspects of this run. The VLA employs a system whereby for each polarization, right and left circular (RC and LC), the incoming radio frequency (RF) is down-converted to intermediate frequencies (IFs) that are at that stage split to double the frequency coverage (see e.g., Napier, Thompson, & Ekers 1983). This results in two IF pairs, IFs A and C and IFs B and D, each pair measuring both senses of polarization. Also, each IF pair is independently tunable within the specified observing band. Usually, the full bandwidths of the IFs *within* an IF pair are set at the same value. The bandwidth of each IF pair and the central frequency can be selected independently. For example, the two IF pairs can be employed to observe two different transitions simultaneously in both RC and LC polarization, or the two pairs can be set in such a way that their bandpasses overlap so as to cover a wider range of frequencies while retaining a

TABLE 3

SUMMARY OF THE VLA OBSERVATIONS

Parameter	Value
Date of observation	1990 Oct 11
Configuration	CnB
Primary beam at half-power (FWHM)	~ 30′
FWHM of synthesized beam (natural weighting)	13″.5 × 12″.0
Total bandwidth (MHz)	
IFs A and B	1.5625
IFs C and D	3.125
Number of channels	
IFs A and B	64
IFs C and D	32
Channel width (km s^{-1})	
IFs A and B	5.25
IFs C and D	21.0
rms noise in channel maps (mJy beam^{-1})	
IFs A and B	1.3
IFs C and D	0.73
Central velocity, heliocentric (km s^{-1})	
IFs A and C	2885.0
IFs B and D	2617.359
Conversion factor: 1 mJy beam^{-1} corresponds to Kelvin	3.74
Largest scale size visible to VLA	7′

higher frequency resolution than would otherwise be possible (see, e.g., the VLA Observational Status Summary, which is updated on a yearly basis).

In addition to what is described above, it is also possible to choose a different total bandwidth *within* one IF pair. There is a penalty, though, because the VLA fringe rotator system, which removes from the interferometer output the rapidly varying sinusoidal component owing to the rotation of the Earth, has only one local oscillator per IF pair. At the VLA the "fringe stopping" is done for the beginning (low-frequency side) of the band. This implies that when different bandwidths are specified, the fringe rate of, for example, IF C is in error with respect to IF A by an amount that is proportional to the difference in frequency of the respective band edges within the pair. This can be expressed as follows:

$$\Delta f = \omega_o \Delta v_D B/c (1) ,$$

where Δf is the error in the fringe rate, ω_o is the angular rotation frequency of Earth, B is the projected baseline in meters, and c is the velocity of light in meters per second. The frequency difference Δv_D is one-half the difference in total bandwidth of the RC and LC IF within the IF pair. Because of the way the IFs are being mixed with Local oscillator signals at the VLA, this means that IFs A and D are fringe-stopped correctly. IFs B and C are off by the amount specified by equation (1). This has two consequences. First, because of the phase winding that is introduced, the correlation within the specified integration interval, which is usually in the range of 20 to 120 s, is degraded. Second, the phase can wind over as much as several radians when going from one secondary calibrator observation to the next.

We selected for our run the following setup for IFs A and B: a total bandwidth of 1.5625 MHz with 64 channels after Hanning smoothing, resulting in 24.414 kHz or 5.25 km s^{-1} wide channels. IFs C and D cover 3.125 MHz with 32 channels at a resolution of 21.0 km s^{-1}. The central velocity for IFs A and C is set at 2885 km s^{-1} and for IFs B and D at 2617.359 km s^{-1}. This choice ensures an overlap of exactly 12 channels between IFs A and B, which together cover at the required high velocity resolution exactly the range of velocities over which H I emission is seen in IC 2163/NGC 2207. IFs C and D cover an additional 200 km s^{-1} on either side of the line emission, providing an ample range of channels for measuring the continuum emission in our field. The low and high velocity resolution observations were done simultaneously with the same antennae and thus cover the same spatial frequencies. We can therefore subtract the continuum maps derived from IFs C and D directly from the high velocity resolution IFs to create maps with line emission only. With this choice of IF mode, the de-correlation which occurs for IFs B and C within a 60 s integration time is only about 5% for the longest baselines and is corrected for automatically when applying the standard complex gain calibration. The phase winding introduced by the frequency offset mentioned above causes the phases for the longest baselines to move up to 4 rad from one observation of the secondary calibrator to the next. The amount of phase winding can be calculated via equation (1) and was removed from the data via the Astronomical Image Processing System (AIPS) routine CLCOR. In retrospect, a marginally better setup would have been possible in which the polarization characteristics (the beam "squint") are taken into account. This is discussed by Mehringer (1992).

After removal of the phase term, the data were calibrated via the standard routines in the AIPS package, with each of the four IFs treated independently. The high velocity resolution IFs (A and B) differ in central velocity by an integer number of channels. We applied the AIPS task CVEL to shift the central velocity of IF D by 5.25 km s^{-1} so that the low velocity resolution IFs (C and D) would also differ in central velocity by an integer number of channels. The calibrated data were mapped, one IF at the time, using the task HORUS to produce sets of naturally weighted and uniformly weighted cubes. The 21 km s^{-1} naturally weighted cubes, which have the highest signal-to-noise ratio, were inspected to determine the range over which H I was detected. The edge channels were discarded, and the line-free channels were averaged to create continuum maps for IFs C and D. These were subtracted from the original cubes of IFs C and D and subtracted from the higher velocity resolution data of IFs A and B. Both the uniformly and naturally weighted continuum maps were averaged and CLEANed.

The continuum-subtracted cubes were CLEANed as well, and subcubes encompassing all the emission were extracted and appropriately merged so that for each of the two velocity resolutions, we have one final cube with natural weighting and one with uniform weighting. The cubes measure 256 × 256 pixels (pixel size = 3″) on a side and are 110 channels and 40 channels deep for the high and low velocity resolution data, respectively. These cubes, which are used for all subsequent analysis, were not corrected for primary beam attenuation since the drop in sensitivity over the field of interest is less then 3%. Except where noted, the radio data shown in the figures here are all from the cubes made with natural weighting.

In addition, the low-velocity, naturally weighted cubes were smoothed to a circular beam of 30″ to enhance the sensitivity to low-level extended emission and then were clipped at a level of 3 mJy beam^{-1}, corresponding to twice the rms noise. In this blanked cube only those areas which contain genuine H I emission were retained. This was done by visual inspection, requiring continuity in velocity when going from one channel to the next. The resulting "masking" cube was applied to the other low velocity resolution cubes and, after interpolation in velocity, to the high velocity resolution cube also.

3.2. *Maps of the* H I *Emission*

Figure 4 displays the channel maps made from the naturally weighted, low velocity resolution (21 km s^{-1}), full spatial resolution (13.″5 × 12″) cube before we attempted to separate the contributions of the two galaxies. These maps are overlaid on *R*-band images, and the heliocentric velocities in kilometers per second are indicated to the side in the figure. Table 4 provides a short description of where emission is seen in each channel map of Figure 4. These features will be discussed again in §§ 4 and 5 below, where we refer to these channel maps as the "unseparated channel maps."

As is evident from Figure 4, the highest velocity channels (v = 3011–2948 km s^{-1}) contain H I emission that comes from the northern part of the eyelid in IC 2163, the tidal tail of IC 2163, and the northern ridge of the double arm. The highest velocity (3011 km s^{-1}) occurs at the eastern end of the northern eyelid, where the streaming arm leaves the oval. The southern ridge of the double arm appears at lower velocities (v = 2927–2780 km s^{-1}) than the northern ridge. This pattern of velocities suggests that the northern oval has rapid streaming motions and that the two parallel arms on the eastern side of IC 2163 have very different origins.

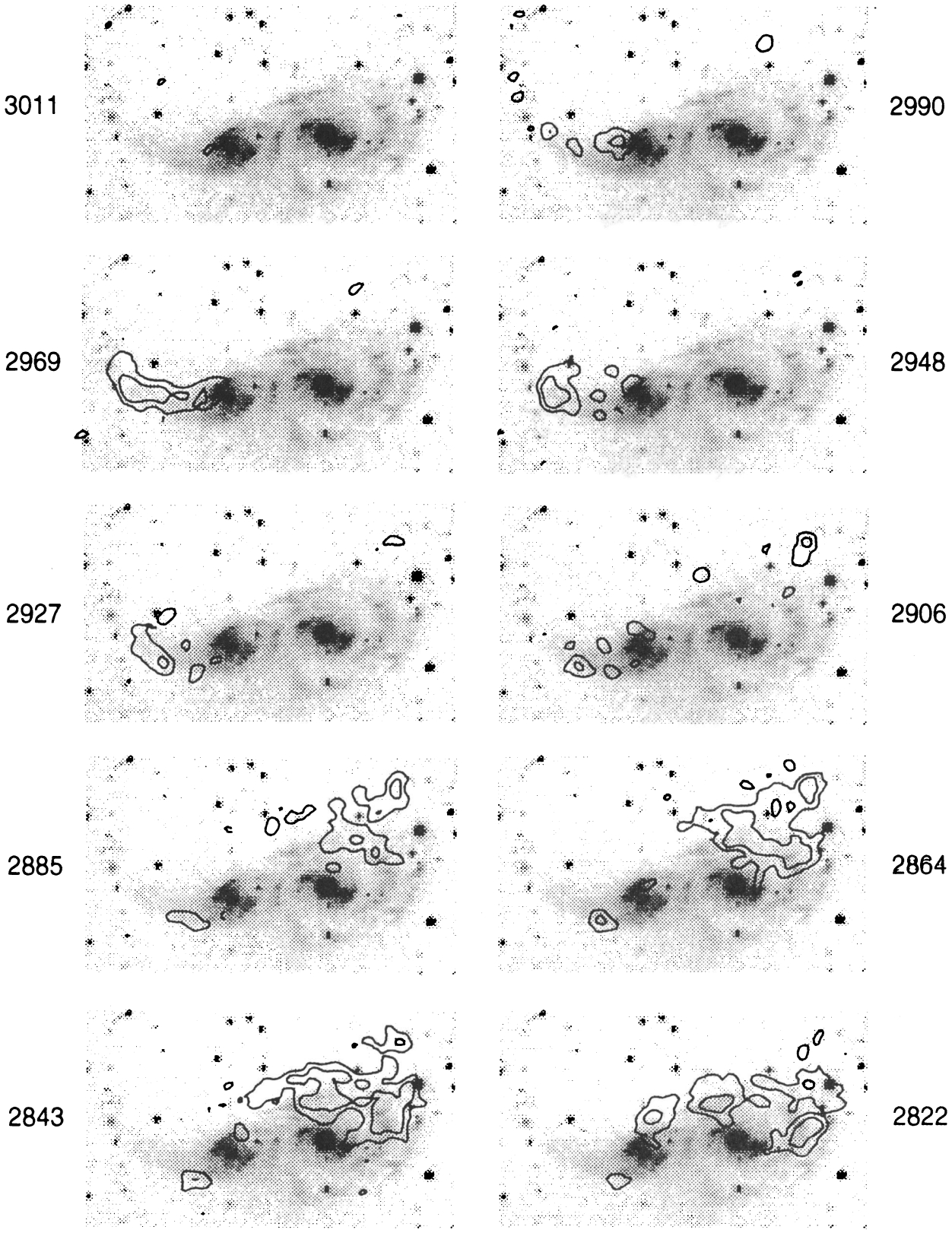

FIG. 4*a*

FIG. 4.—Channel maps showing the H I emission as contours overlaid on *R* band as gray scale. The channel maps are made from the naturally weighted cube with 21 km s^{-1} velocity resolution and 13″.5 × 12″ spatial resolution before we separated the H I contributions of the two galaxies. The heliocentric velocities are given in km s^{-1}. The contour levels are at 3, 6, 12 times the rms noise, and the lowest contour level is 2.2 mJy $beam^{-1}$, which corresponds to 8.2 K. All the H I emission outside of the optical images in some frames belongs to the frame above, i.e., this peripheral gas is always south of the galaxies.

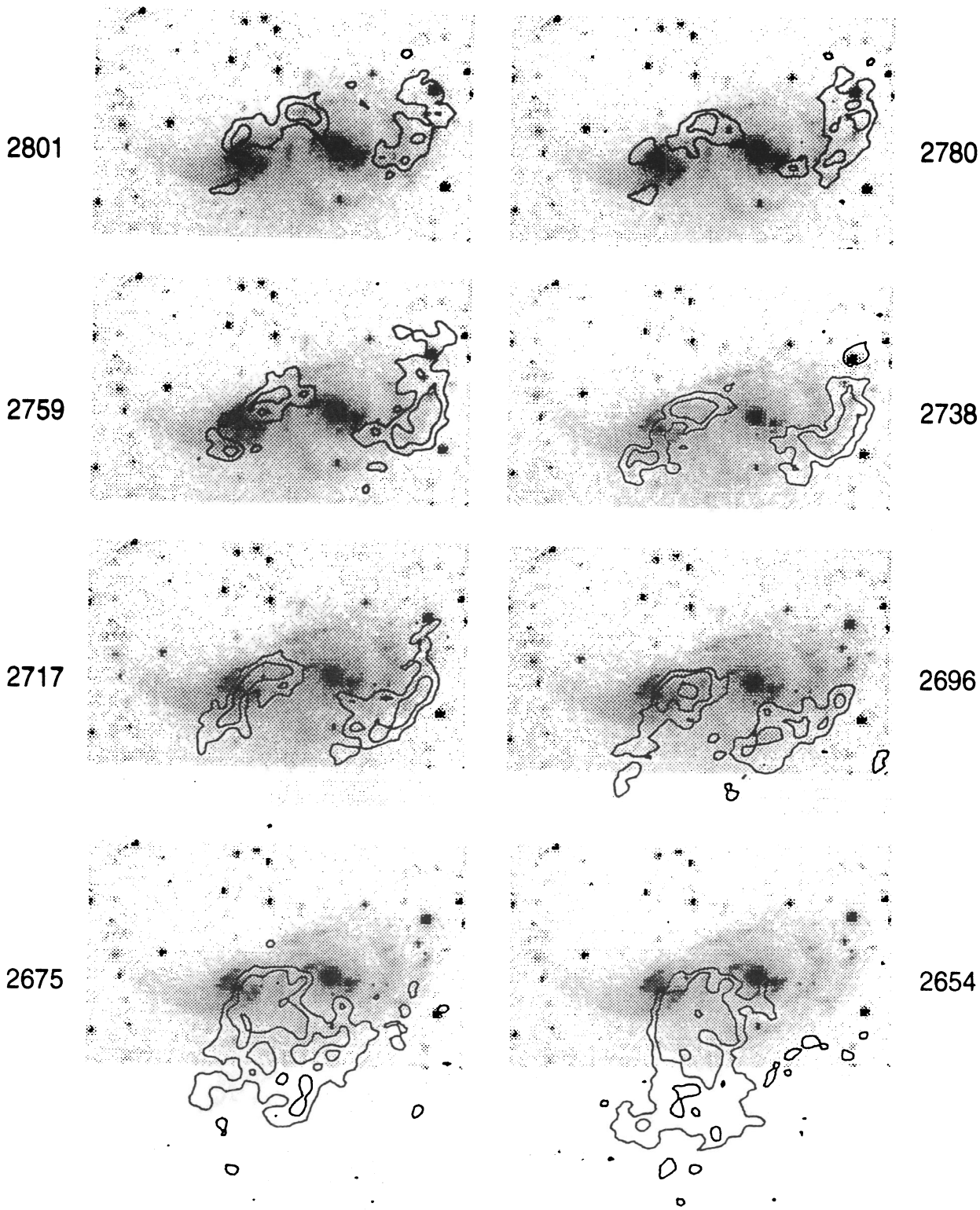

FIG. 4*b*

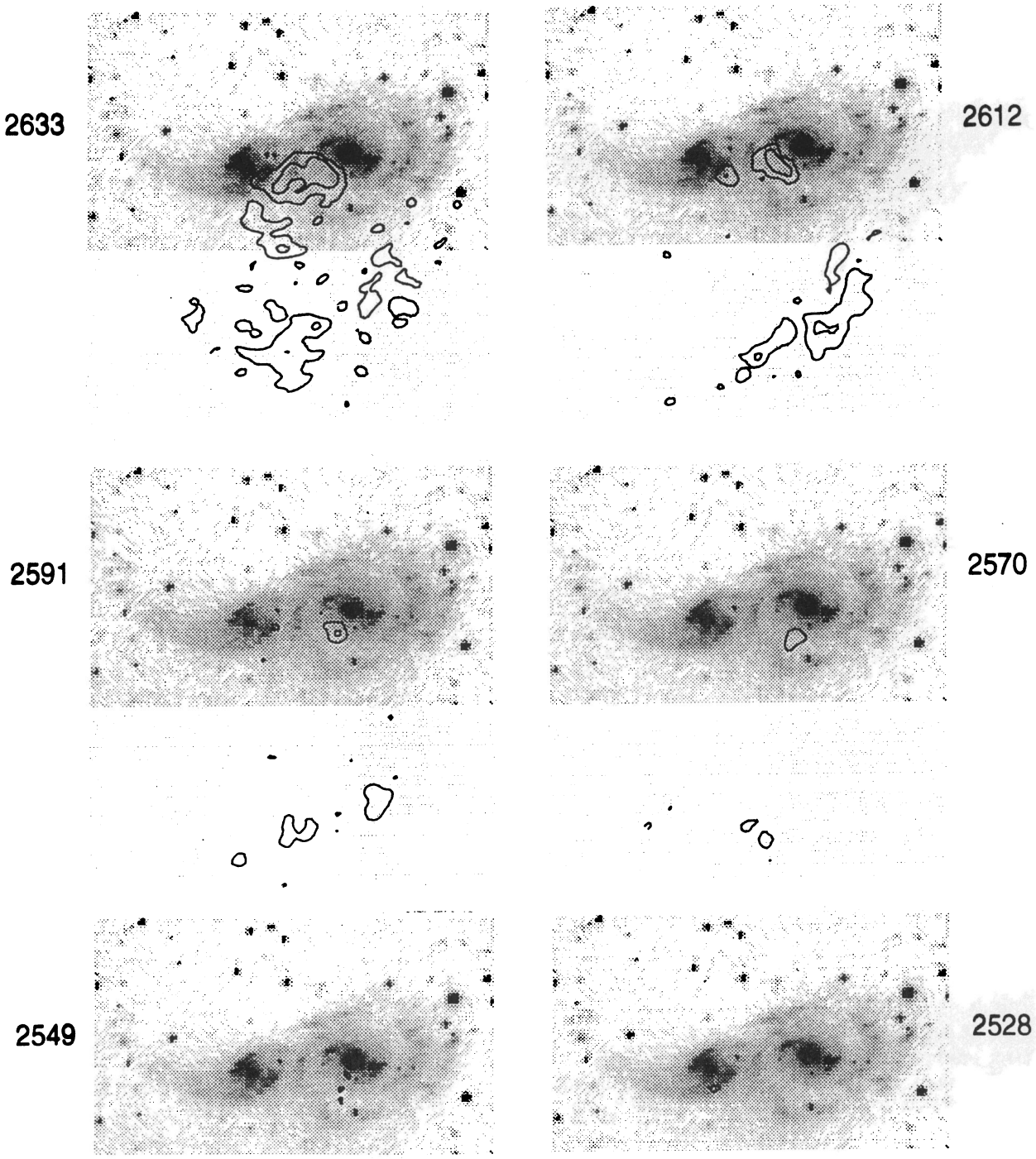

FIG. 4c

Figure 4 also indicates that the directions of the photometric and kinematic minor axes of IC 2163 differ by approximately 60°. On the kinematic minor axis, the emission in the channel map should have bilateral symmetry relative to the nucleus. Where the photometric minor axis of IC 2163 at P.A. = 38° crosses the northern eyelid of IC 2163, the channels with emission in excess of 3 times the rms noise have velocities of 2969–2948 km s^{-1} (clearly emission from IC 2163) and 2801–2780 km s^{-1} (blended with emission from NGC 2207), but where the photometric minor axis crosses the southern eyelid, the channels with bright emission have much smaller velocities of 2696–2633 km s^{-1} (all may have some blending with NGC 2207) and 2612 km s^{-1}. In fact, the kinematic minor axis appears as bilaterally symmetric features in the 2759–2780 km s^{-1} channel maps at a position angle of approximately 155°.

Figure 5 displays the total H I column densities for the two galaxies. For the naturally weighted map with full spatial resolution shown here, an H I surface brightness of 100 Jy $beam^{-1}$ m s^{-1} corresponds to a column density of 5.45 $M_{\odot}$ pc^{-2}. Several giant H I clouds are visible as dark, closed-

TABLE 4

H I Emission Features in the Unseparated, Low Velocity Resolution Channel Maps

Channel(s) (km s^{-1})	Location of Emission in Excess of 3 Times the rms Noise
3011:	
IC 2163	Eastern end of northern eyelid, where northern component of the double-arm leaves the oval.
2990–2948:	
IC 2163	Extended tidal tail, northern ridge of double arm, northern eyelid (includes northern photometric minor axis but no emission from southern photometric minor axis at this velocity).
NGC 2207.....	Outer northern region.
2927–2906:	
IC 2163	Southern ridge of double arm, western part of northern eyelid.
NGC 2207.....	Outer northwestern and northern regions.
2885–2822:	
IC 2163	Southern ridge of double arm, western end of northern eyelid (blended with NGC 2207 at 2822 km s^{-1}).
NGC 2207.....	Northern, northwestern, and western portions. Notice emission jutting down from the outer galaxy to southwestern end of bar; this indicates rapid streaming at bar end.
2801–2738:	
IC 2163	Symmetric emission from western end of northern eyelid (blended with NGC 2207) and eastern end of southern eyelid (particularly symmetric in the 2780 and 2759 km s^{-1} channels). Bilateral symmetry is expected on the kinematic minor axis, but notice that the axis of symmetry is nearly along the photometric major axis of the oval. Emission on eastern part of northern eyelid is most likely from NGC 2207 since IC 2163 has emission here at 2948–2990 km s^{-1}.
NGC 2207.....	Eastern and western portions of main disk, with surprisingly little variation in the location of emission over this range of velocities. This emission is from the H I ring. Notice the S-shape to the distribution of emission in these channels. The kinematic minor axis, with nearly symmetric emission on each side in the central part of the disk, shows up in the 2759–2738 km s^{-1} channels; this axis of symmetry differs by 63° ± 4° from the photometric minor axis of the disk.
2717–2696:	
IC 2163	Southern eyelid (blended with NGC 2207).
NGC 2207.....	Eastern and western portions of main disk, with streamers to the south.
2675–2633:	
IC 2163	Southern eyelid (blended with NGC 2207). Western tidal arm (just southwest of NGC 2207 nucleus) is present but blended with NGC 2207 and easier to distinguish in the 2612 km s^{-1} channel map.
NGC 2207.....	Eastern part of main disk and long southern extension to galaxy.
2612–2570:	
IC 2163	Western end of southern eyelid, western tidal arm (just south and southwest of NGC 2207 nucleus).
NGC 2207.....	Outer part of southern extension.

contour regions in each galaxy. We show in §§ 4.5 and 5.5 that these clouds contain over $10^8\ M_\odot$. Figure 6 displays the mean velocity field derived from the total data cube. The kinematic minor axis of each galaxy is evident, although for IC 2163 there is considerable blending with NGC 2207.

3.3. *Separation of the* H I *Contributions of the Two Galaxies*

Despite the fact that the two systems partially overlap in projection and share a range of radial velocities, it is possible to identify how much H I emission belongs to one system and how much to the other. In order to separate the two galaxies, we followed the method described by Brinks & Burton (1984). We first inspected the various cubes in different ways. We used the AIPS task TVMOVIE to display in rapid succession the channel maps in a movie-like fashion. We produced sets of position-velocity (PV) maps made parallel to the principal kinematic axes of NGC 2207 and displayed these as a movie. Lastly, we inspected the data in a solid-body three-dimensional rendering mode. In our case, displaying the cubes channel by channel in movie mode was most useful. For example, starting with the highest velocity channels (v = 3011–2948 km s^{-1}) in Figure 4, one sees emission in IC 2163 from the tidal tail and the northern eyelid of the oval quite distinct from any emission from NGC 2207. We chose the blanked naturally weighted cube at full spatial resolution and 21 km s^{-1} velocity resolution, as it exhibits the best compromise between sensitivity and resolution, and isolated both galaxies by drawing polygons on a TV display. The resulting set of masks (interpolated in velocity for the high velocity resolution cubes) were applied to the various final cubes to produce separate cubes for each galaxy. Those areas that we could not separate in this fashion were initially included in both galaxies. We then constructed total surface brightness maps and velocity fields for each galaxy separately and for the region of overlap. Assuming that the ratio of gas in IC 2163 compared to NGC 2207 in the overlap region is similar to the global ratio, we

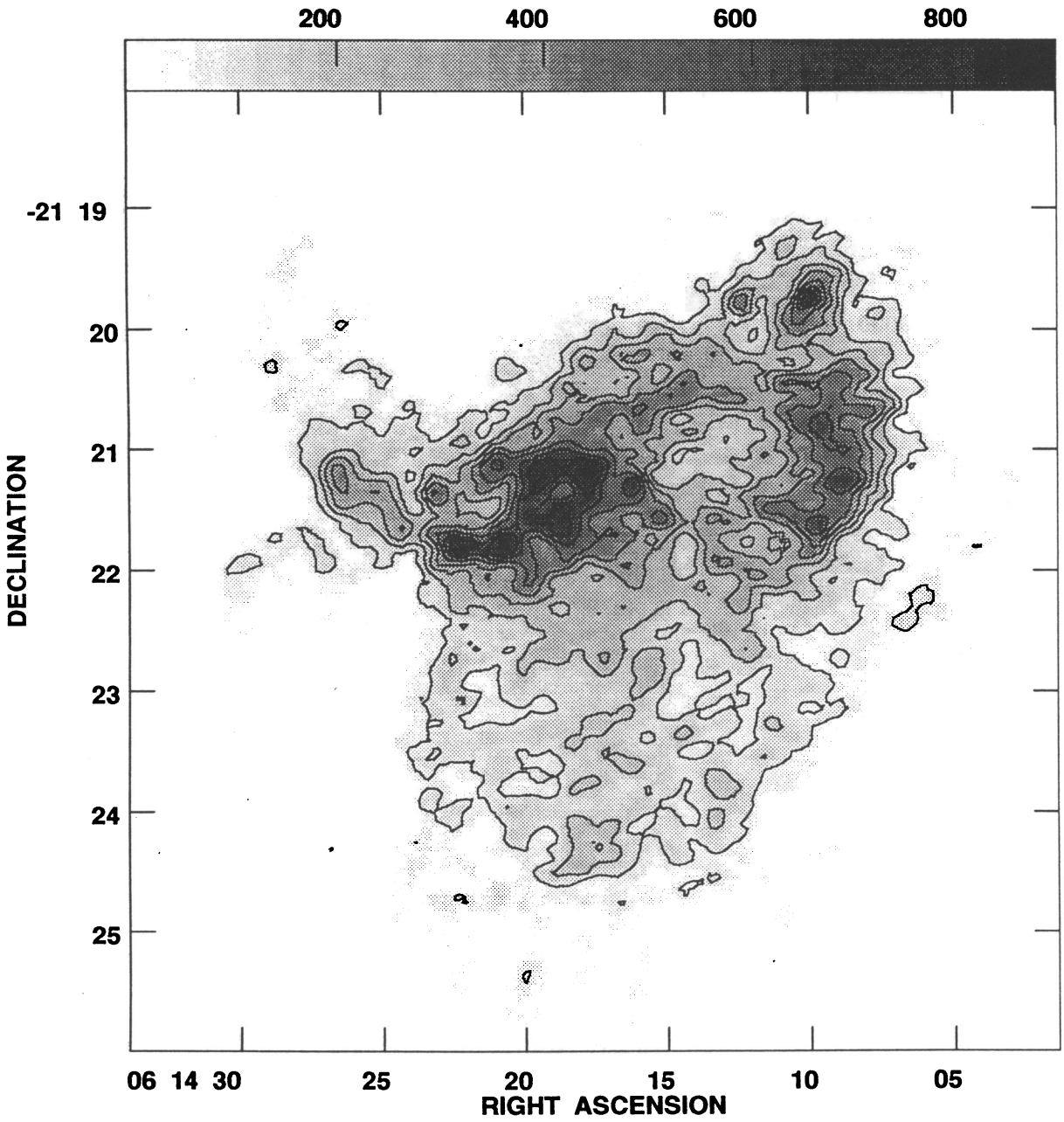

FIG. 5.—Contour plus gray scale display of N(H I) in the unseparated column density image derived from the same cube as the channel maps in Fig. 4. The contour interval is 100 Jy beam^{-1} m s^{-1} or 374 K km s^{-1}, which corresponds to a column density of 5.45 $M_{\odot}$ pc^{-2}. The contour levels are 100, 200, 300, 400, 500, 600, and 700 Jy beam^{-1} m s^{-1}.

attributed about 80% of gas in the overlap region to NGC 2207 and applied this final correction to the total surface brightness maps that show the two galaxies separately.

The H I surface brightness and velocity displays in § 4 are based on the emission assigned to IC 2163, while those in § 5 are derived from the emission assigned to NGC 2207. We find for NGC 2207 a total line flux of 76.0 Jy km s^{-1} and for IC 2163 a total line flux of 16.5 Jy km s^{-1}, corresponding to H I masses of $2.2 \times 10^{10}(75/H_0)^2\ M_{\odot}$ and $4.8 \times 10^{9}(75/H_0)^2\ M_{\odot}$, respectively. Our total H I mass is in fair agreement with the Nançay single-dish observations by Bottinelli, Gougenheim, & Paturel (1982), who measure an H I mass for the system of $2.0 \times 10^{10}(75/H_0)^2\ M_{\odot}$.

4. H I PROPERTIES OF IC 2163

4.1. *General* H I *Morphology of IC 2163*

The result of our separation of the H I contributions from the two galaxies is shown in color in Figure 7 (Plate 2), which overlays the CCD R-band image in red, the CCD B-band image in blue, and the H I column density N(H I) image in green. The top display shows the H I associated with IC 2163; the bottom display, the H I associated with NGC 2207.

Figure 8 is a contour plus gray-scale display of N(H I) from IC 2163 and reveals the clumpy structure of the H I gas. Boxes are drawn around five giant clouds that will be discussed in § 4.5. Relative to the nucleus, the western H I arm is symmetric

PLATE 2

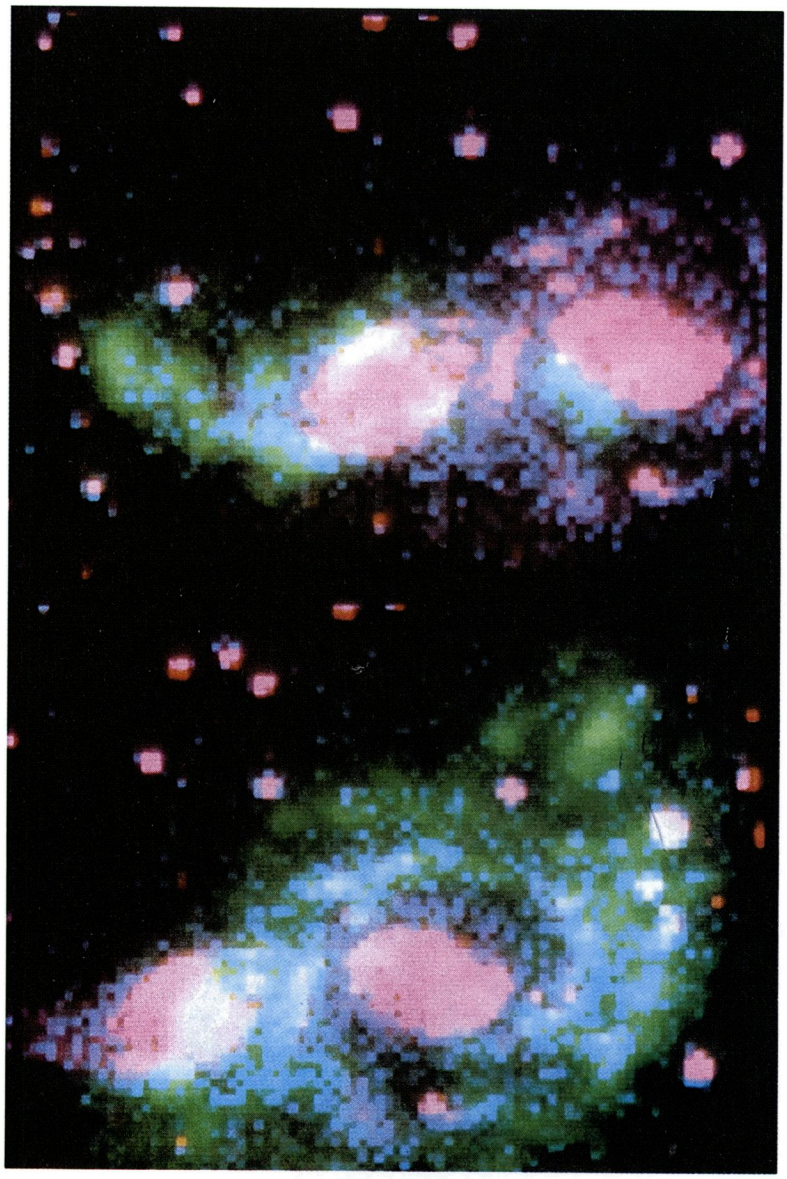

FIG. 7.—Overlay of the CCD *R*-band image in red, the CCD *B*-band image in blue, and the *N*(H I) images in green. *Top*: *N*(H I) in IC 2163. *Bottom*: *N*(H I) in NGC 2207. The separation between the two components of the double arm on the anticompanion side of IC 2163 is visible in the bottom display.

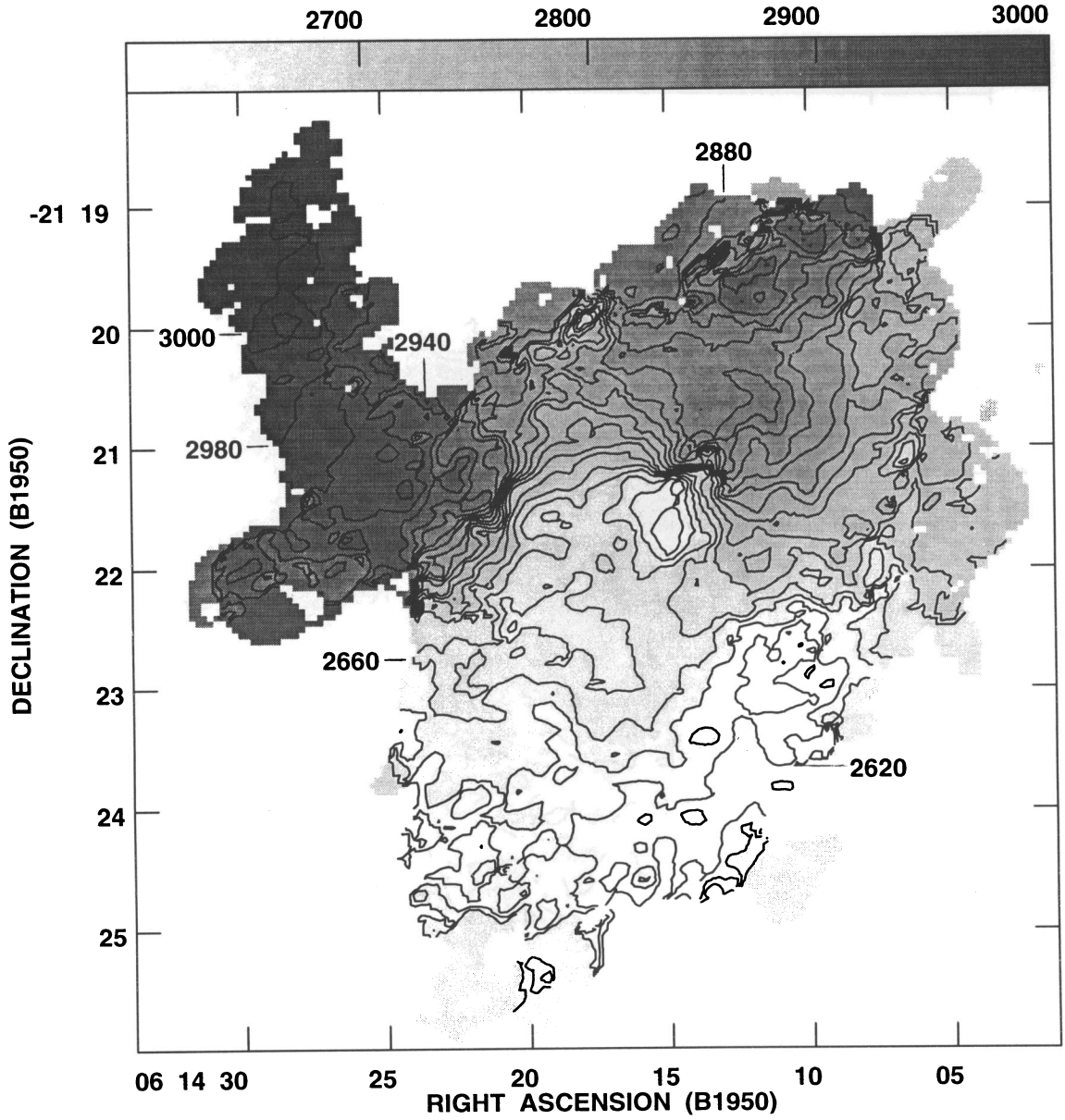

FIG. 6.—Contour plus gray scale display of the unseparated velocity field derived from the same cube as the channel maps in Fig. 4. The contour interval is 20 km s^{-1}, and the contour levels range from 2600 to 3000 km s^{-1}. Notice that the highest velocities occur on the eastern side of IC 2163.

to the eastern tidal arm. In the unseparated channel map displays in Figure 4, H I emission from the western tidal arm appears clearly as a feature just southeast of the nucleus of NGC 2207 at $v = 2612$ km s^{-1} and in neighboring channels. This western tidal arm is predicted by the models of ocular galaxies (ESES), but it is obscured by NGC 2207 in the optical images. The central hole in the H I distribution coincides with the optical nucleus of IC 2163. The H I column density image reveals ocular structure similar to that in the optical, but with the H I ridge along the eyelid regions clearly displaced to the outer side of the optical eyelid (see Fig. 7). The bright part of the eastern arm in H I corresponds well with the double arm in the optical images. The tidal tail is longer in H I than in the optical images; in the plane of the sky, the faint outer end of the H I tidal tail extends to a distance of 190″ (=32 kpc) from the nucleus.

Our method for separating the H I contributions for the two galaxies is subjective, but it was done without reference to the optical images or computer models and without imposing any symmetries. The resulting images are nevertheless symmetric relative to the nucleus, and this lends credibility to the method. Our most secure results are from regions where it is easy to distinguish between the contributions from the two galaxies, i.e., the eastern tidal arm and the outer end of the western tidal arm in IC 2163 and the western and northern portions and the far southern extension in NGC 2207.

One puzzling feature is the faint H I extension heading southeast from the southern part of the eastern tidal arm on the IC 2163 map. This H I streamer has no obvious optical counterpart, although it is roughly similar and parallel to the optical streamers that jut south from NGC 2207 in Figure 1*c*. It has velocities of 2930–2960 km s^{-1}, similar to those on the

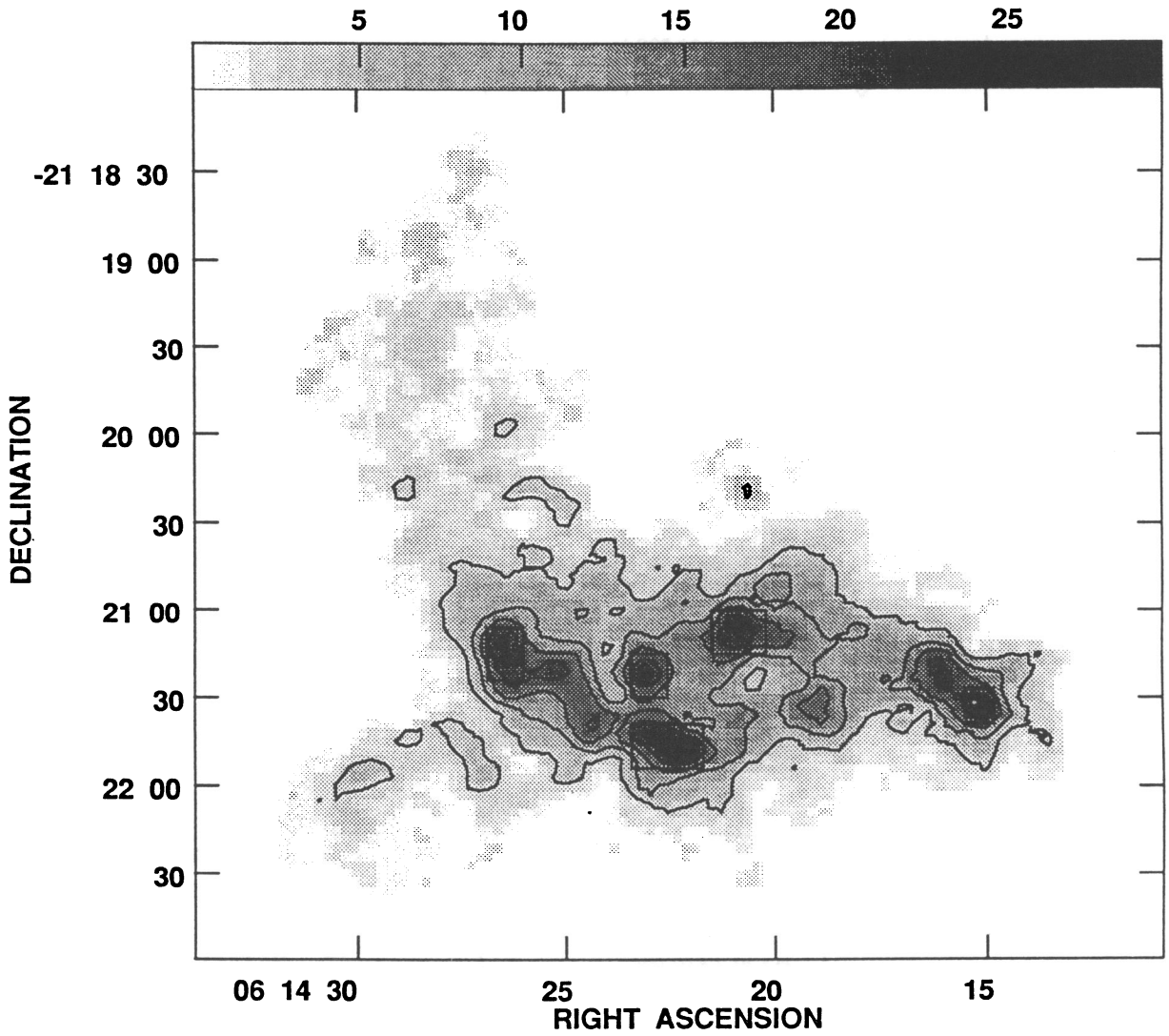

FIG. 8.—Contour plus gray scale display of N(H I) for the total H I emission associated with IC 2163, i.e., after the separation of the emission from the two galaxies (see text). The data are from the naturally weighted cube with 13″.5 × 12″ spatial resolution and 21 km s^{-1} velocity resolution. The contour levels are 5, 10, 15, 20, and 25 $M_{\odot}$ pc^{-2} and the gray-scale wedge is in $M_{\odot}$ pc^{-2}. Boxes are drawn around the five IC 2163 massive clouds listed in Table 6 below.

eastern arm of IC 2163 (see Fig. 12) but 200 km s^{-1} greater than that of the closest gas that we attribute to NGC 2207. One possibility is that this H I streamer is from NGC 2207, and the gas is now moving rapidly toward IC 2163.

4.2. *The Eastern Tidal Arm in IC 2163*

If the tidal arm in IC 2163 is trailing, then the galaxy rotates counterclockwise and the southern component of the double tidal arm is leading. Such double-arm structure is consistent with simulations in ESES and in Paper II below. The two components of the eastern arm of IC 2163 are then as follows: (1) in the south, a broad tidal arm which has a gradual increase in density toward the leading edge, and (2) in the north, a thin, shorter arm (a "streaming arm") produced when material streaming from the companion side of the disk intersects the trailing part of the tidal arm. The streaming arm could be preceded by a shock front in the gas, which may produce a dust lane between the two components. Such double-arm structure should be formed in interacting galaxies with in-plane tidal forces but should be very short-lived; thus, few interactions are likely to show it unless the epoch is favorable.

The numerical simulations in ESES for ocular galaxies predict a velocity difference of approximately 100 km s^{-1} between the two components of the double arm. Although these simulations were for collisionless particles, we find a similar velocity jump in the H I gas. Figure 9 shows H I emission contour diagrams of declination versus velocity for cuts across the double arm at fixed values of the right ascension (α). For each value of α, there are two main velocity components from the double arm. The component with the higher velocity coincides with the streaming arm in the north, and the component with lower velocity coincides with the tidal arm in the south. The velocity of the streaming arm is nearly constant with α. The typical line-of-sight velocity difference between the two arms is approximately 100 km s^{-1} and decreases systematically from 150 km s^{-1} at the apex of the oval to 40 km s^{-1} near the outer end of the streaming arm, as shown in Figure 10. Over this same range of α, the separation in declination

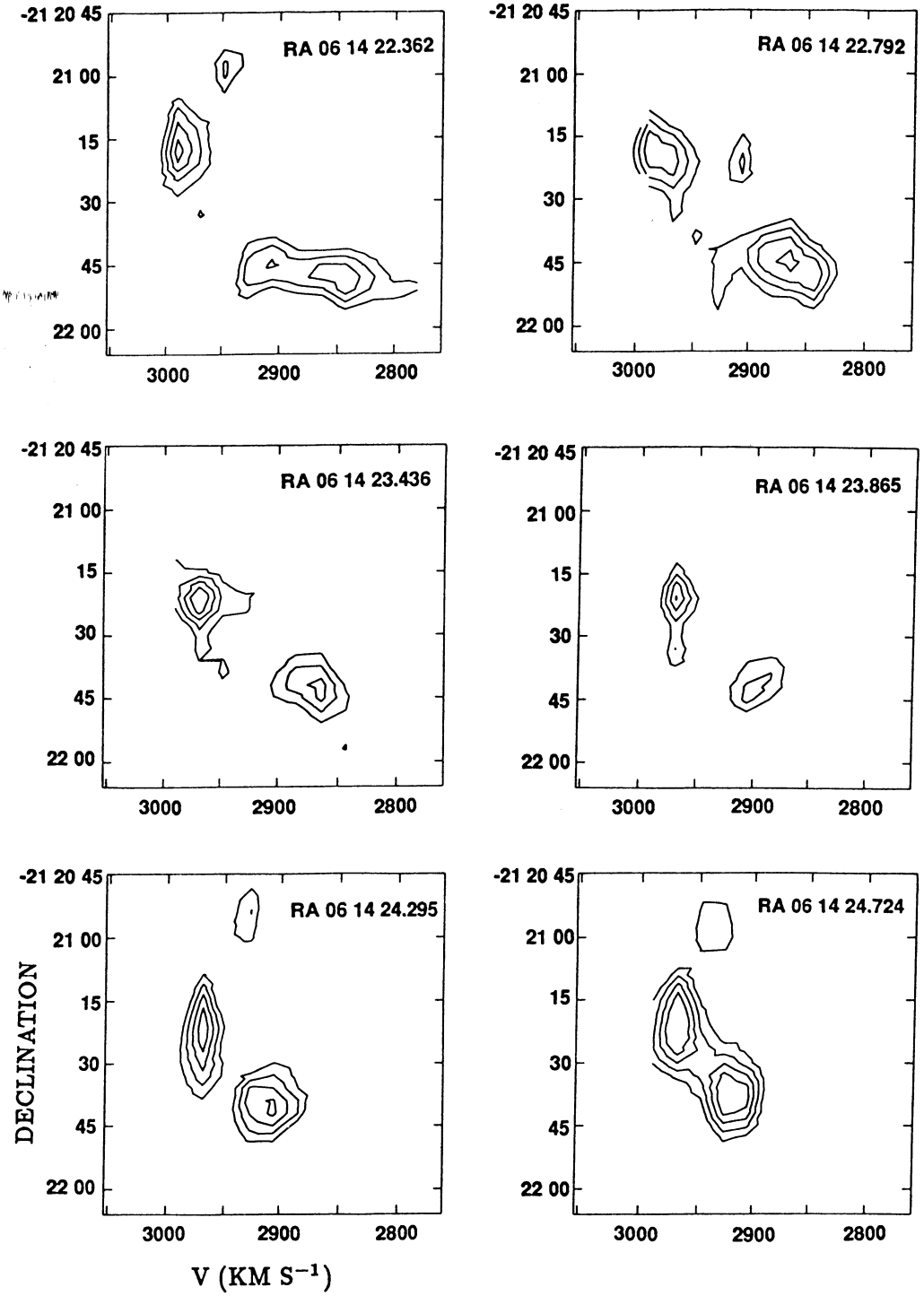

FIG. 9.—The two components of the double arm in IC 2163: contours of H I surface brightness in a declination vs. velocity display for cuts across the arm at six different values of right ascension. The data are from the naturally weighted cube with 13.″5 × 12″ spatial resolution and 21 km s^{-1} velocity resolution. The contour levels are at 3, 4, 5, and 6 times the rms noise, and the lowest contour level is 2.2 mJy beam^{-1}, or 8.2 K.

decreases (Fig. 10) from 33″ to 18″ as the two streams converge toward the outer end of the arm. The velocity jump between the northern and southern components of the double arm can also be seen in the unseparated channel maps (Fig. 4), where emission from the northern part of the double arm appears in the 2990 and 2969 km s^{-1} channels and emission from the southern part of the double arm appears from 2927 to 2780 km s^{-1}.

The high-velocity and the low-velocity components of the double arm are each spatially resolved in declination in our H I data (see Fig. 9), and the streaming arm appears broader than in the ESES simulations, which assume an initial velocity dis-

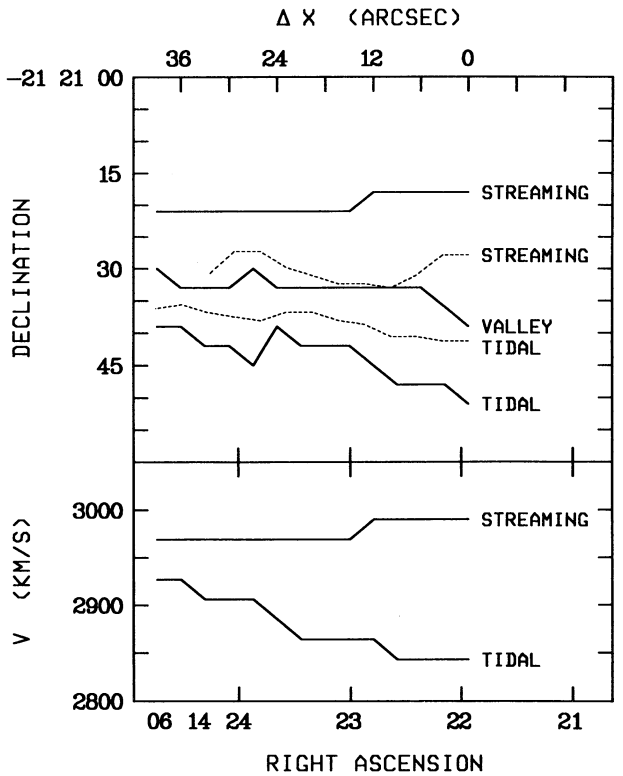

FIG. 10.—Solid curves showing the position of the H I valley and the positions and velocities of the two main H I velocity components in each declination vs. velocity diagram along the double arm. The component with the higher velocity is labeled the streaming ridge; the other component, the tidal ridge. Dashed curves show the locations of the optical ridges. The displacement $\Delta x = \Delta\alpha \cos(\delta)$ is measured eastwards from the apex of the oval at $\alpha = 06^h14^m21^s.933$.

persion of zero. We define the H I valley as the division in declination between the high-velocity ($v > 2938$ km s^{-1}) and the low-velocity ($v < 2938$ km s^{-1}) features in the declination-velocity diagrams of Figure 9. In the H I valley, emission is relatively weak in each channel. It is significant that the H I valley, defined in terms of separate velocity components, coincides with the optical valley defined in terms of *R*- and *B*-band surface brightness (see § 2). Table 5 shows the variation in the ratio of ridge-to-valley surface brightness in H I as a function of position $\Delta\alpha \cos\delta$ measured eastward from the eastern apex of the oval, so as to correspond to Figure 10. The surface brightness integrations were done on the H I cube at the H I ridge and valley positions shown in Figure 10, and the high- and low-velocity ranges were defined as above. By "total," we

TABLE 5

RIDGE-TO-VALLEY CONTRAST RATIOS IN H I SURFACE BRIGHTNESS ON THE EASTERN TIDAL ARM OF IC 2163

	STREAM RIDGE/VALLEY		TIDAL RIDGE/VALLEY	
$\Delta\alpha \cos\delta$[a]	Total	High Velocity	Total	Low Velocity
0″–12″	1.2	2.0	2.5	5.2
12″–24″	1.7	2.8	1.9	2.6
24″–36″	0.85	1.6	1.3	1.9
36″–42″	0.79	1.3	1.0	1.4

[a] Measured eastward from the eastern apex of the oval at $6^h14^m21^s.933$.

mean the summation over the total range of velocities at that position. As indicated in Table 5, the streaming arm is distinct at high velocities out to 42″ (=7 kpc) east of the apex, but without this velocity information the streaming arm would appear to blend with the tidal arm much sooner. In maps of the total H I column density, the streaming arm becomes just a shoulder on the tidal arm beyond 30″ from the apex, because in the valley the total H I emission includes a significant contribution from low-velocity gas associated with the brighter tidal arm. While this is probably the result of limited spatial resolution, it may also suggest that the streaming and the tidal arms are not exactly in the same plane. The maximum column density of H I occurs in the tidal arm, which is also brighter optically than the northern ridge (see Table 5 and Figs. 1 and 26, below).

The H I velocity dispersion is high throughout the region where the two components of the double arm are distinguishable, decreasing eastward along the tidal arm from approximately 60 km s^{-1} to approximately 30 km s^{-1} for the range of α in Figure 10. In noninteracting galaxies, typical H I velocity dispersions (Dickey, Hanson, & Helou 1990) are less than 10 km s^{-1}. The high velocity dispersion is most likely turbulence produced by the tidally generated gas flows. Beyond this point, the dispersion continues to decrease; in the long, faint part of the H I tidal tail that heads north from $\delta = -21°20'30''$ to $-21°18'30''$, the velocity dispersion is only 7 to 17 km s^{-1}.

Figures 7 and 8 show that the tidal arm has an S-shaped wiggle, which is also present in the *N*-body simulations of ESES at time steps 1650 and 1700 of their Figure 3. It occurs where the velocity components from the tidal and streaming arms merge and could be caused by the ram pressure of the streaming arm.

4.3. *Mean Velocity Field of IC 2163*

Figures 11 and 12 display the mean velocity field of IC 2163 with full spatial resolution (13″.5 × 12″) and high velocity resolution (5.25 km s^{-1}) after the H I emission of IC 2163 was separated from that of NGC 2207. In Figure 11, the isovelocity contours are overlaid on the *R*-band CCD image, and in Figure 12, on the *N*(H I) image in gray scale. The high-velocity side is on the east and northeast, and the low-velocity side is on the west and southwest.

The optical velocity in the nucleus of IC 2163 is 2756 ± 15 km s^{-1}, according to V. Rubin, K. Borne, and C. Peterson (unpublished). The kinematic minor axis of the mean H I velocity field in Figures 11 and 12 gives $v_{sys} = 2775 \pm 10$ km s^{-1}. In Figure 4, the bilaterally symmetric features in the unseparated channel maps suggest that v_{sys} for IC 2163 lies in the 2759–2780 km s^{-1} channels. All of these values are reasonably close. The optical value for v_{sys} is sensitive to the placement of the spectroscope slit on the nucleus; the H I values are sensitive to the separation procedure for the emission from the two galaxies. Splitting the difference, we adopt 2765 km s^{-1} with an uncertainty of ±20 km s^{-1}.

As mentioned in § 4.1, the low-velocity H I emission from the outer end of the western (optically obscured) tidal arm of IC 2163 is easily distinguished from the H I gas in the companion. From the emission above 3 times the rms noise in the H I cube with 5.25 km s^{-1} velocity resolution, we find that the lowest velocity gas in the clump at the outer end of the western tidal arm (72″ from the nucleus) has $v = 2560$ km s^{-1} and that the highest velocity gas at the diametrically opposite location on the eastern arm has $v = 2980$ km s^{-1}. The average of these two

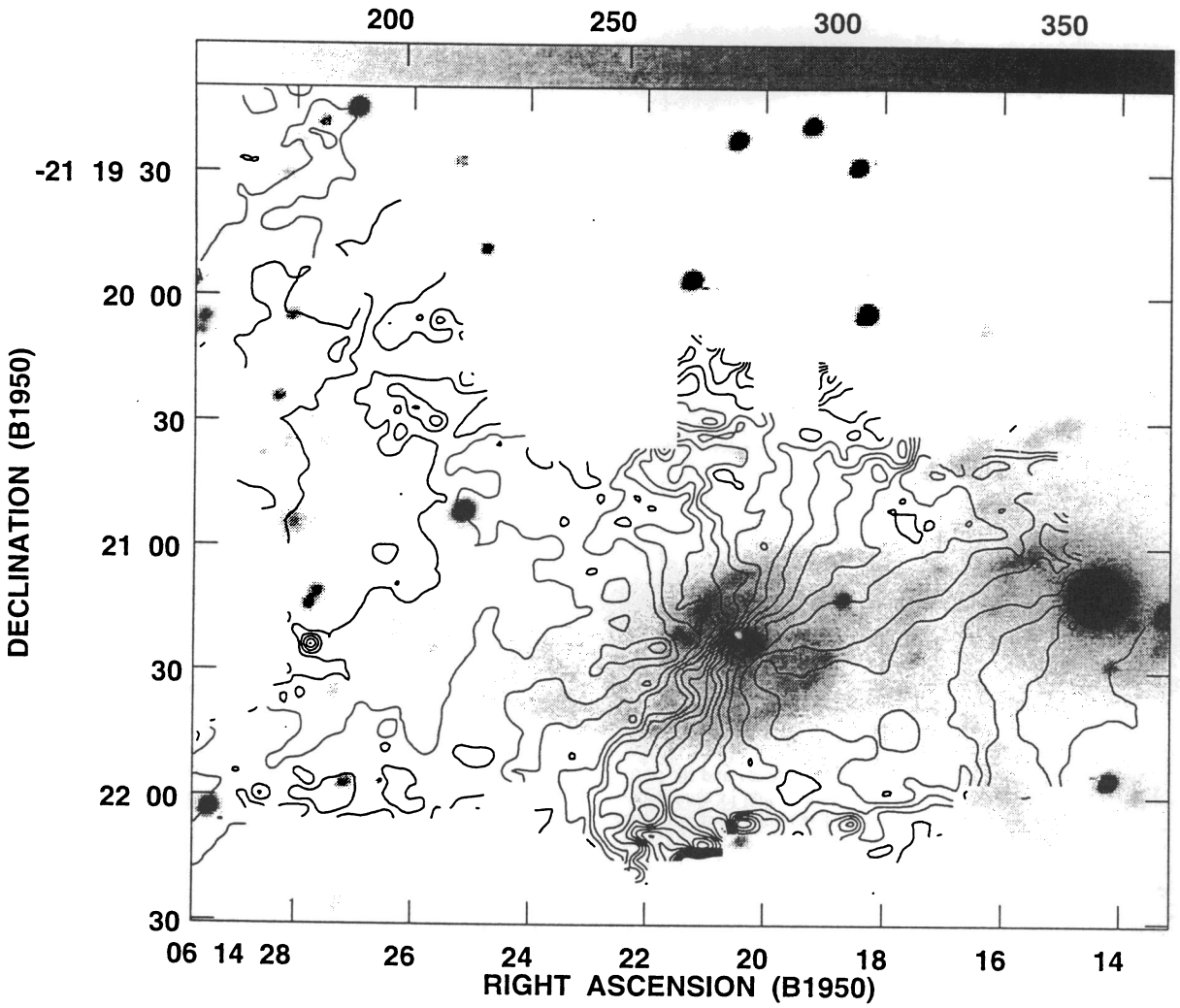

FIG. 11.—Velocity field of IC 2163 obtained from data with 13".5 × 12" spatial resolution and 5.25 km s^{-1} velocity resolution superposed on the *R*-band image in gray scale. The eastern side of the galaxy is the receding side. The contour levels are 2600 km s^{-1} ... (20 km s^{-1}) ... 3000 km s^{-1}.

velocities is 2770 km s^{-1}, which is about the same as the systemic velocity. If we use the mean velocities at these two locations instead of the extremes, we obtain an average of 2775 km s^{-1}. Thus, the symmetry between the brighter portions of the eastern and western tidal arms is evident not only in the *N*(H I) image but also in the velocities. In their atlas of encounter simulations, Howard et al. (1993) point out that such symmetries between the tidal tail and the tidal bridge are expected in close tidal encounters only if the orbit of the companion lies within a few degrees of the plane of the disk.

An unusual feature of the velocity field, visible even in Figure 4, is that the straight velocity contours crossing the nucleus in IC 2163 are nearly parallel to the apparent major axis of the oval, i.e., *the kinematic minor axis* (with a position angle of 155° ± 10°) *lies close to the optical major axis of the oval* (with a position angle of 128° ± 3°). The unusual relative orientation of the photometric and kinematic minor axes in IC 2163 suggests that the intrinsic shape of the galaxy is oval. We adopt the terminology "line of nodes of the projection" to mean the intersection between the plane of the sky and the plane of the galaxy. If the disk were intrinsically circular and flat, and all of the motions circular, then the line of nodes of the projection would be both the photometric and the kinematic major axis. For IC 2163, the line of nodes of the projection is probably perpendicular to the kinematic minor axis, i.e., it has a position angle of 65° ± 10°, and the disk inclination is approximately 40° (a face-on disk would have inclination = 0°) from the model results in Paper II. This implies that the intrinsic shape of IC 2163 is an oval with a 2:1 axial ratio. The projection makes the oval look less eccentric and the isophotal major axis shorter than they really are. In this interpretation, the oval shape in the plane of the sky results mainly from highly elliptical orbits, not a high inclination of the galaxy.

The isovelocity contours show no evidence for a bar. The bar may be weak, but since the major axis of the bar differs by only 13° ± 10° from the line of nodes of the projection, the bar is close to the singular viewing angle for which streaming motions along the bar are not apparent in the velocity contours. It is possible also that there is no real bar in IC 2163. Our simulations in Paper II have an inner structure that resembles a bar at this same position angle even though there is no bar in the face-on projection.

Figure 13 shows a slice of the mean H I velocity field through the nucleus of IC 2163 along the line of nodes of the projection at P.A. = 65°. On the eastern side of IC 2163, this slice stays on the northern side of the double arm and shows velocities con-

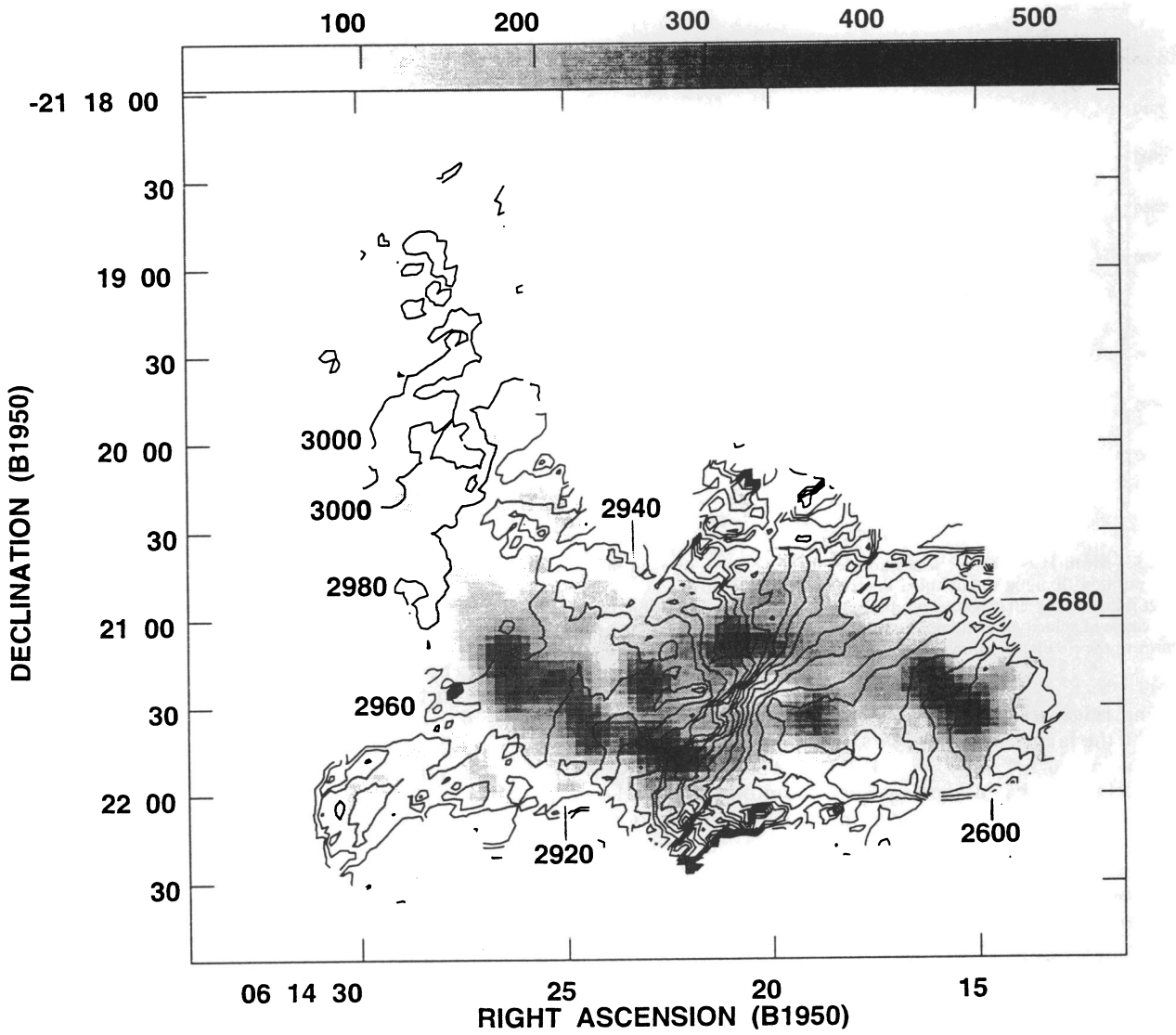

FIG. 12.—The isovelocity contours from Fig. 11 superposed on a gray-scale image of the H I column density from Fig. 8. The gray-scale wedge is in units of Jy beam^{-1} m s^{-1}. The contour levels are 2580 km s^{-1} ... (20 km s^{-1}) ... 3000 km s^{-1}.

tinuously rising in the outer part of the galaxy. (The plateau in Fig. 13 at 2880 km s^{-1} is probably the result of some residual blending with emission from NGC 2207.) Rubin & Ford (1983) plotted optical emission-line velocities v sin (i) versus position along a slit at P.A. = 97° (see Fig. 29 below, where the H I and optical velocities are compared), which passes through the nuclei of both galaxies and then cuts across the double arm from north to south. The velocity difference between the streaming and tidal arms makes the "rotation curve" appear to be falling on the eastern side. Rubin & Ford (1983) call attention to the decrease in rotational velocity with increasing nuclear distance in both galaxies, and Reshetnikov (1992) then cites both galaxies as examples of interacting galaxies with falling rotation curves. The difference in the behavior of v sin (i) as a function of radial distance for P.A. = 65° and P.A. = 97° illustrates the complexity of the velocity field resulting from the interaction with NGC 2207. With much of the galaxy in highly noncircular motion, no single slice across the velocity field can represent the rotation curve.

In the long faint part of the tidal tail that heads north from $\delta = -21°20'30''$ to $-21°18'30''$, the velocity field has very little variation with position, the isovelocity contours in Figure 12 take values between 2980 and 3000 km s^{-1} with no systematic trend along the arm, and the H I velocity dispersion is typical of values found in undisturbed spiral galaxies. The constant velocity here agrees with the models in Paper II below.

4.4. *Velocity Streaming in IC 2163*

In a disk with pure circular rotation, the locations with the highest absolute values of ($v_{obs} - v_{sys}$) should lie on the line of nodes of the projection. Along the oval in IC 2163, the gas with the highest value of v_{obs} is at the eastern end (P.A. = 92°) of the northern eyelid, and the gas with the lowest value of v_{obs} is at the western end of the southern eyelid (see the channel maps for 3011 km s^{-1} and 2591 km s^{-1} displayed in Fig. 4). These two positions are displaced 27° counterclockwise from the line of nodes of the projection, which implies that the orbit speed is not constant with azimuth at this radius. We refer to the high-velocity feature at the eastern end of the northern eyelid as the launch point for the streaming arm, since this is where the

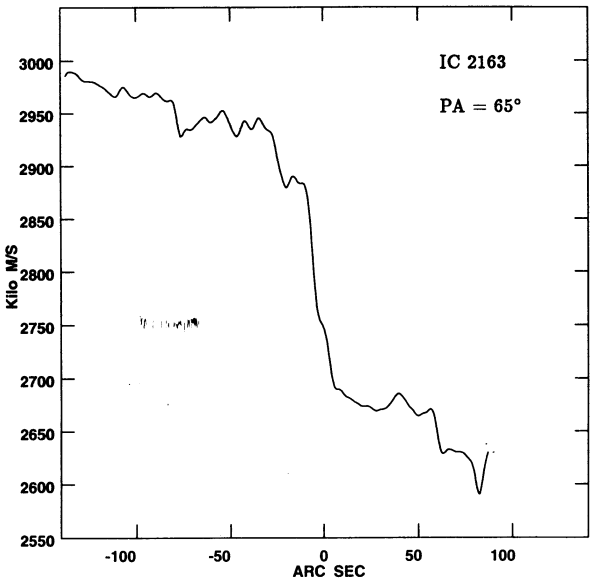

FIG. 13.—Mean H I velocity vs. position for a slice passing through the nucleus (position 0) along the adopted line of nodes of the projection. The northeast side is on the left (negative positions) and the southwest side is on the right. Because of velocity streaming, the values of v sin (i) in this diagram do not represent the circular rotation curve.

streaming ridge described in § 4.2 departs from the oval. In Figure 11 the launch point appears as a closed, high-velocity contour at $\alpha = 6^h14^m22^s$, $\delta = -21°21'24''$. The backward-C–shaped deformations in the isovelocity contours along the northern optical eyelid culminate at the launch point and indicate high-velocity material streaming away from us along the northeastern side of the eyelid and into the northern part of the eastern double arm.

From the data with 5.25 km s^{-1} resolution, we find that the value of ($v_{obs} - v_{sys}$) is 10–16 km s^{-1} greater at the launch point than at the line of nodes of the projection at the same radius. The lower value pertains if we use the mean velocities, and the higher value pertains if we use the highest velocities with significant emission at each position. Recall that, in general, if the motion is confined to the plane of the disk, then

$$(v_{obs} - v_{sys})/\sin(i) = v_c \cos(\theta) + \Delta v_t \cos(\theta) + v_r \sin(\theta), \quad (2)$$

where v_c is the circular velocity, Δv_t is the excess tangential velocity, v_r is the radial velocity, and θ is the azimuthal angle in the face-on image, set equal to 0 for the northern line of nodes. For pure circular rotation, the value of ($v_{obs} - v_{sys}$) should be 12% lower at the launch point than on the line of nodes, while in IC 2163, ($v_{obs} - v_{sys}$) is 5%–7% higher at the launch point. Thus, Δv_t and v_r are probably positive at the launch point. Positive Δv_t is expected from the conservation of angular momentum for material that has just crossed over the northern eyelid of the oval after falling in from larger radii (ESES); positive v_r is expected at the launch point, where the stream bends outward to produce the streaming ridge at larger radii on the double arm.

The following argument rules out values of the inclination $<25°$ because they would yield unreasonably large values for the excess tangential velocity. For an undisturbed spiral galaxy with the same B_T^0 luminosity as IC 2163, the luminosity-v_{max} relation in Persic & Salucci (1991) predicts a maximum v_c equal to 225 ± 25 km s^{-1} (where the uncertainty represents the uncertainty in the extinction correction for IC 2163). From the mean velocities on the northeastern part of the line of nodes in IC 2163 (see Fig. 13), we find ($v_{obs} - v_{sys}$) = 185 ± 20 km s^{-1}. If the inclination of IC 2163 were 25°, then ($v_{obs} - v_{sys}$)/sin (i) would be 440 ± 47 km s^{-1}, and the excess tangential velocity on the northeastern line of nodes would be 215 ± 54 km s^{-1}, which is unreasonably large for a nonmerging encounter. Thus, the observed values of the tangential velocity on the line of nodes of the projection rule out small values of i, while the position angle of the kinematic minor axis rules out large values of i. With $i = 40°$, the excess tangential velocity on the northeastern line of nodes is 65 ± 40 km s^{-1}.

4.5. *Massive* H I *Clouds in IC 2163*

The H I gas in IC 2163 contains several massive clumps, visible in Figures 7 and 8. As indicated in Figure 14, cloud I1 is near the outer end of the brighter part of the eastern tidal arm, clouds I2 and I3 are on the eastern tidal arm near the apex of the oval, and cloud I4 is near the outer end of the western tidal arm. Cloud I5, on the northern eyelid, is centered 9″ = 1.5 kpc north of the end-of-bar optical clump (pointed out in Fig. 3). In Figure 8, boxes are drawn around these giant cloud complexes in IC 2163. Table 6 lists the following properties of these clouds: the position of peak column density, the peak and the average H I column densities, in which the average is calculated inside the box, the total H I mass in the box, and the average velocity dispersion σ before and after correction for the veloc-

TABLE 6

GIANT H I CLOUDS

Cloud	α(1950)	δ(1950)	⟨N(H I)⟩ ($M_\odot$ pc^{-2})	N(H I)$_{peak}$ ($M_\odot$ pc^{-2})	⟨σ⟩$_{obs}$ (km s^{-1})	⟨σ⟩$_{corr}$ (km s^{-1})	Mass (× 10^8 $M_\odot$)
IC 2163:							
I1	06^{h}14^{m}26^s.4	−21°21′15″	20	24	20	19	1.8
I2	06 14 23.2	−21 21 21	18	24	56	55	1.4
I3	06 14 22.1	−21 21 48	19	29	56	51	2.6
I4	06 14 15.3	−21 21 33	19	23	36	34	1.0
I5	06 14 20.9	−21 21 06	16	21	55	48	1.8
NGC 2207:							
N1	06 14 09.9	−21 19 45	21	43	58	56	7.7
N2	06 14 09.5	−21 20 48	29	36	50	49	10
N3	06 14 08.8	−21 21 15	29	38	43	41	5.5
N4	06 14 09.7	−21 21 36	27	37	42	40	3.9
N5	06 14 20.6	−21 21 48	26	38	43	40	3.8
N6	06 14 17.9	−21 21 12	28	36	47	46	4.6

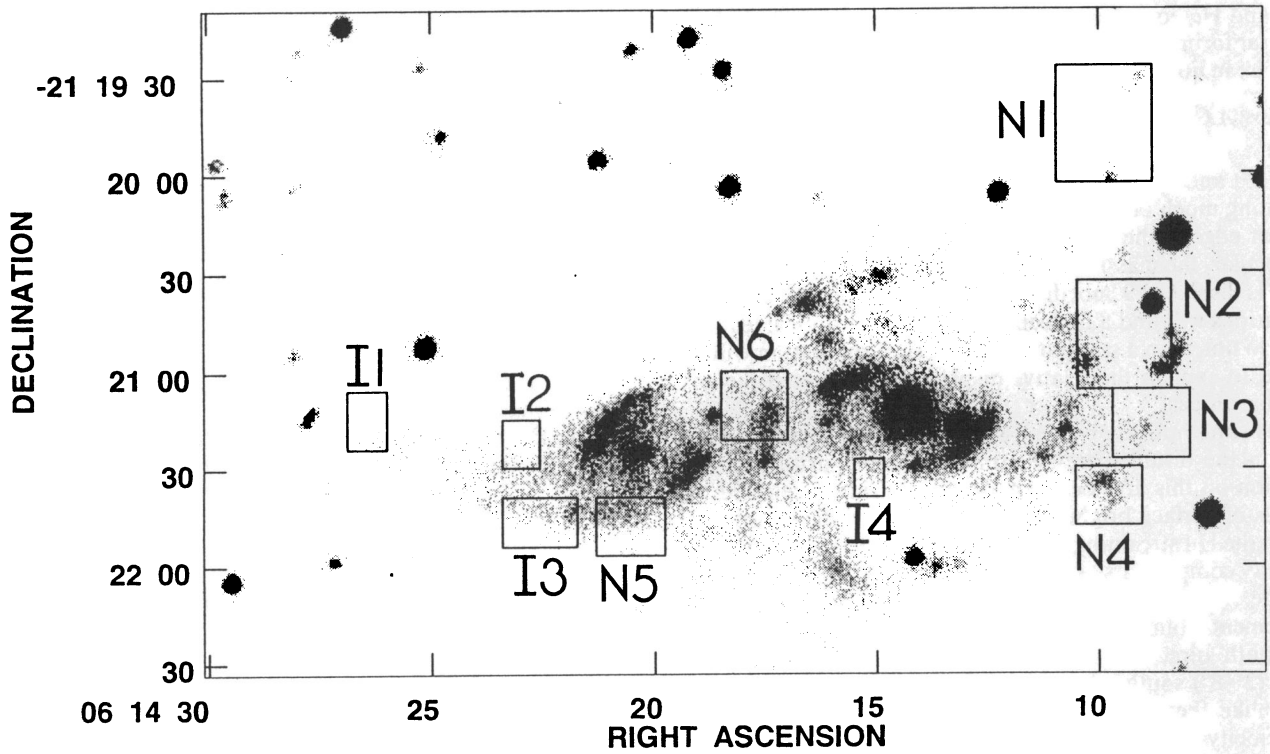

FIG. 14.—*B*-band image in gray scale with boxes marking the locations of four massive H I clouds on the tidal arms of IC 2163 and six massive H I clouds in NGC 2207.

ity gradient across the Gaussian radius of the synthesized beam. (The corrected velocity dispersion was obtained by subtracting in quadrature the change in the velocity field across the Gaussian radius.) Cloud I5 lies in the part of the northern eyelid that has a blending problem with NGC 2207 as noted in Table 4. To be conservative, we attribute only the gas with $v > 2817$ km s^{-1} to cloud I5.

These five clouds have extremely large masses, 10^8 $M_\odot$ or greater, even if an estimate for the intercloud H I in each box is subtracted from the total emission. They are comparable in mass to dwarf galaxies and to the clouds and star formation complexes at the outer ends of the tidal tails in the Antennae and Superantennae galaxies (Mirabel, Lutz, & Maza 1991; Mirabel, Dottori, & Lutz 1992). They are also similar to the massive H I clumps discovered by Hibbard et al. (1992) in five merging pairs of galaxies. From Figure 12, one can see that these clouds have the same mean velocities as the neighboring H I in the disk, so they must have formed there.

The H I velocity dispersions in these clouds and in the neighboring gas on the tidal arms are high, 20–55 km s^{-1}. For cloud I3, Figure 15 shows the H I line profile averaged over the cloud and smoothed to a velocity resolution of 10.5 km s^{-1}. Elmegreen et al. (1993) suggest that this high velocity dispersion is responsible for the large cloud sizes if the clouds formed by a gravitational instability in the disk. They also predict that cloud I1, on the anticollision side of IC 2163, may escape to form a future dwarf galaxy. NGC 2207 also contains massive H I cloud complexes with high internal velocity dispersions, as described in § 5 below.

Although there is blue-light emission from each of the massive clouds on the tidal arms, none is unusually bright in *B* band or in Hα. In Condon's (1983) λ20 continuum images, clouds I2, I3, and I4 are part of the tidal arms detected in the radio continuum, but none of these clouds appear as particularly bright clumps, and no radio continuum emission is detected from cloud I1. Optically, the brightest of the four clouds on the arms is cloud I3 on the southern ridge of the eastern arm near the apex of the oval; it contains a blue-light

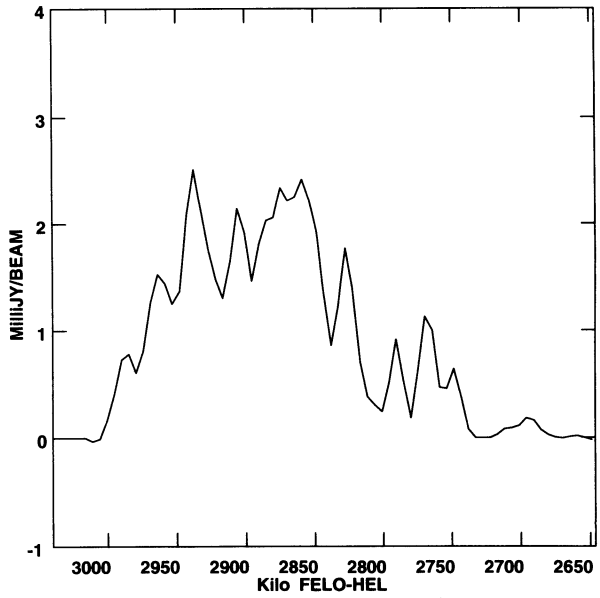

FIG. 15.—For giant cloud I3, the H I velocity profile averaged over the cloud and smoothed to a velocity resolution of 10.5 km s^{-1}. The rms noise is 0.54 mJy beam^{-1} per smoothed channel. The spectrum was obtained from the H I cube in which only regions of believable H I signal were retained, as described in § 3.1. This spectrum shows the high velocity dispersion in the gas.

clump and Hα emission typical of H II regions on spiral arms. Thus, star formation is occurring in cloud I3, but none of these clouds are major star formation regions yet.

4.6. *A Comparison between* H I *and Optical Features in IC 2163*

The H I and optical ridges in IC 2163 do not always coincide. Along much of the oval, the H I ridge is displaced toward the outer edge of the optical eyelid (compare Figs. 11 and 12). In particular, the massive H I clump at the northeastern end of the bar is displaced 9″ north of the optical clump. Perhaps CO observations will find a molecular clump at the optical feature. If they do not, then a star plus gas numerical simulation will be required to explain the relative displacement between the gas and stellar ridges.

The H I and optical observations agree on the location of the valley on the double-parallel arm (the eastern arm), but the separation on this arm between the optical ridges, selected on the basis of surface brightness, is smaller than the separation between the H I streaming and tidal ridges selected on the basis of velocity components. As shown in Figure 10, the H I streaming ridge lies 8″–12″ north of the northern optical ridge, a displacement comparable to the 12″ H I resolution in the north-south direction, and the H I tidal ridge is displaced slightly (2″–8″) south of the southern optical ridge. Since the stars, unlike the gas, form a collisionless system and have a high velocity dispersion, the gas stream may be partially decoupled from the stellar stream. A star plus gas numerical simulation is necessary to account for the minor differences in the spatial distributions described here.

5. H I PROPERTIES OF NGC 2207

5.1. *General* H I *Morphology of NGC 2207*

Figure 16 is a contour plus gray scale display of the total H I column density in NGC 2207 as derived from the naturally weighted data cube with 13″.5 × 12″ spatial resolution and 21 km s^{-1} velocity resolution. Boxes are drawn around massive clouds listed in Table 6 and discussed below.

NGC 2207 has a very different appearance in H I than in a short optical exposure. The brightest H I emission is concentrated in a broad clumpy ring or partial ring, which is 8 kpc thick on the eastern and western sides and opens to the south. The nucleus of NGC 2207 lies in an H I hole. For the region of the ring, Figure 17 overlays the H I column density contours on the *R*-band emission displayed in gray scale (see also Figure 7). The H I ring contains the stellar arms, but only in the northern part of the H I ring does the H I ridge consistently coincide with the stellar arm. In the eastern and western parts of the ring, *the* H I *ridge often lies in the interarm region between the stellar arms*, and the H I column density is higher than in the northern part of the ring.

Five of the six giant clouds in NGC 2207 with H I masses in excess of $10^8\ M_\odot$ are in the eastern or western portions of the H I ring (see Fig. 16 and Table 6). The largest of these (cloud N2) has a mass of $10^9\ M_\odot$ and sits in the interarm region between the two western stellar arms. On the eastern part of the ring, the center of cloud N6 and the H I ridge heading south from this cloud are also in the interarm region. Cloud N1 (see Figs. 14 and 16) lies north of the H I ring but appears to connect to the northwestern part of it. Other properties of these clouds will be discussed in § 5.5.

The lack of correspondence between the stellar spiral arms and the H I peaks is unusual for galaxies. One possible scenario is that the spiral arms were present before the perturbation and, aside from the wave propagation, were unchanged by IC 2163 because NGC 2207 was not strongly perturbed in the in-plane direction. Since the stars form a collisionless system, the stellar system may respond differently than the gas to a tidal perturbation, e.g., the gas may undergo shocks and be more prone to form clumps.

The H I ring and the main optical disk of NGC 2207 have about the same major axis position angle. If we assume these features are intrinsically circular, then the position angle of the line of nodes of the projection is 110° ± 7°. Actually, we believe that NGC 2207 is warped on the line of sight and that the true line of nodes is more like 140°, based on models in Paper II and on the orientation of the kinematic major axis.

The H I ring and the main optical disk are in the northern part of a large, elliptically shaped distribution of fainter H I emission. The position angles of the isophotal major axes of this fainter H I gas distribution are 330° in the north and 160° in the south and thus differ from the position angle of the line of nodes of the projection. The outermost H I contours in the long southern extension of this ellipse form an outer envelope for the faint *B*-band streamers that arc south of NGC 2207 and IC 2163 in Figure 1*c*. The faint optical emission has the same asymmetry relative to the nucleus and a similar radial extent as the H I emission. Although the H I distribution extends to greater radii in the south than in the north, the total H I mass south of the nucleus ($1.2 \times 10^{10}\ M_\odot$) is about the same as the total H I mass north of the nucleus ($1.0 \times 10^{10}\ M_\odot$). The H I ring comprises 73% of the total H I emission from NGC 2207, and the H I mass south of the ring is 3 times that north of the ring.

The H I ring in NGC 2207 looks similar to the incomplete H I ring in NGC 2273 (van Driel & Buta 1991). NGC 2273 also has a central bar, but the circumstances differ from NGC 2207 because the H I ring in NGC 2273 corresponds to the outermost of two outer stellar pseudorings and there is only one, pure gaseous ring in NGC 2207. Also, NGC 2273 does not appear to have a close companion, and NGC 2273 has an order of magnitude smaller H I surface density than the NGC 2207 ring and no detected elliptical extension.

5.2. *Channel Maps Reveal the Agitation of the Gas in NGC 2207*

Figure 4 shows large regions on the eastern and western portions of the H I ring that are essentially unchanged from channel map to channel map over a wide range of velocities (2696–2801 km s^{-1}). This gas must have a very large velocity dispersion to show up in such a wide range of channels (see § 5.4). Clearly, a lot of gas on the eastern and western lobes of the ring has been stirred up by the interaction. Removal of the H I emission associated with IC 2163 does not affect this result, since the western side of NGC 2207 is not contaminated by IC 2163.

Figure 18 shows H I line profiles in the H I ring and in the feature connecting the ring to cloud N1. These profiles were made from the data with 5.25 km s^{-1} velocity resolution and 13″.5 × 12″ spatial resolution. On the eastern and western portions of the ring, the velocity profiles are very broad and asymmetric, with no obvious pattern to the asymmetries (the rms noise = 1.33 mJy beam^{-1}). The asymmetries imply that this is not simply an isothermal disk in hydrostatic equilibrium with a large scale height. The line profiles in the southern H I exten-

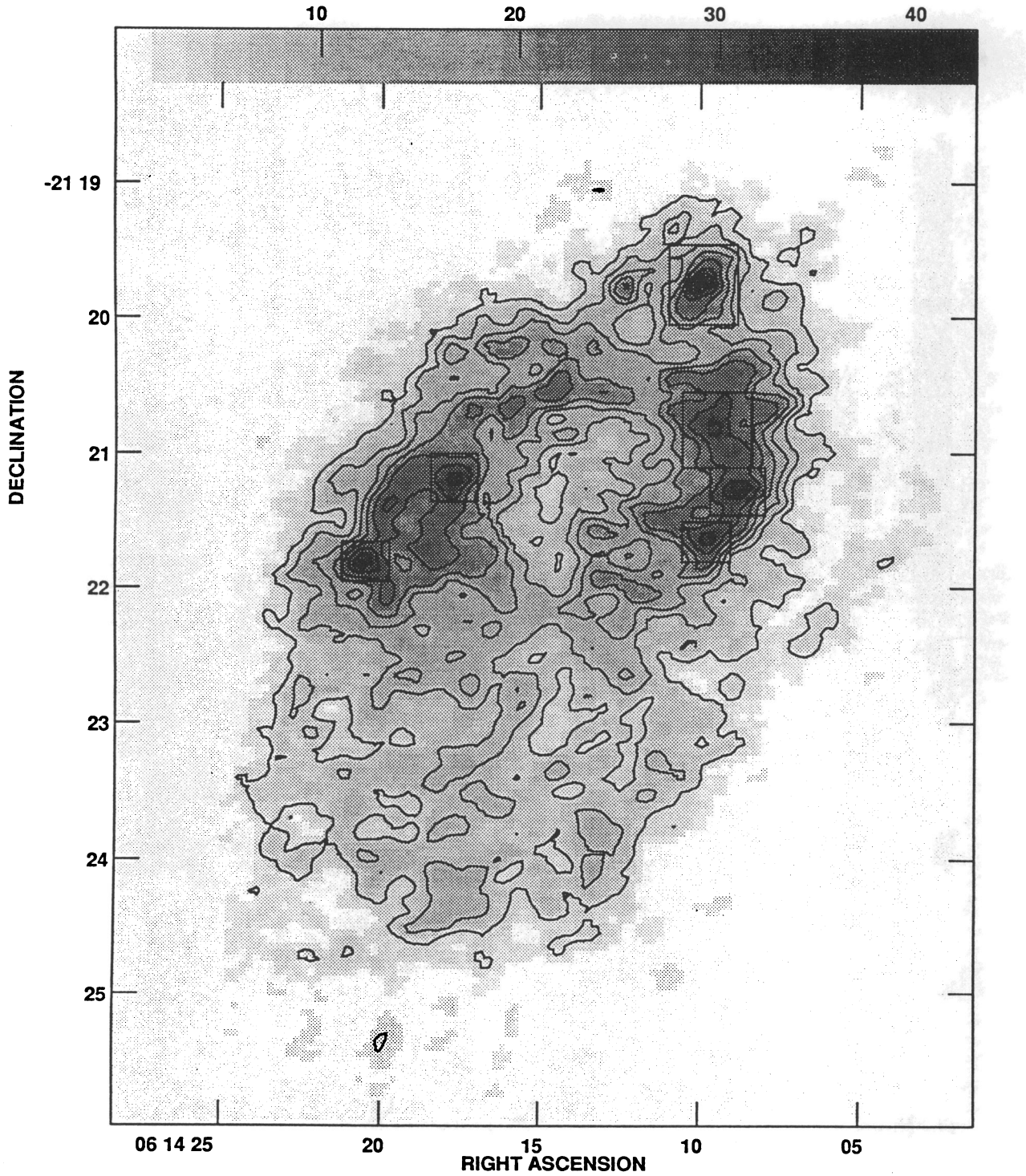

FIG. 16.—Contour plus gray scale display of N(H I) for the total H I emission associated with NGC 2207, i.e., after separation of the emission of the two galaxies. The data are from the naturally weighted cube with 13.″5 × 12″ spatial resolution and 21 km s^{-1} velocity resolution. Boxes are drawn around the clouds listed in Table 6. The contour levels are 5, 10, 15, 20, 25, 30, and 35 $M_{\odot}$ pc^{-2}, and the gray-scale wedge is labeled in units of $M_{\odot}$ pc^{-2}.

sion and in the northern part of the ring are less complex and not as broad.

5.3. *Mean Velocity Field in NGC 2207: Evidence for a Strong Warp*

Figure 19 displays the high velocity resolution (5.25 km s^{-1}), full spatial resolution (13.″5 × 12″) velocity field of NGC 2207 overlaid on the R-band image. There are small kinks almost everywhere on the velocity contours; the kinks do not show a clear association with the spiral arms even with unsharp masking of the mean velocity image. The failure to find strong density-wave streaming is probably a consequence of the limited spatial resolution (2.3 × 2.0 kpc) of our full spatial resolution image. On the other hand, our data do show evi-

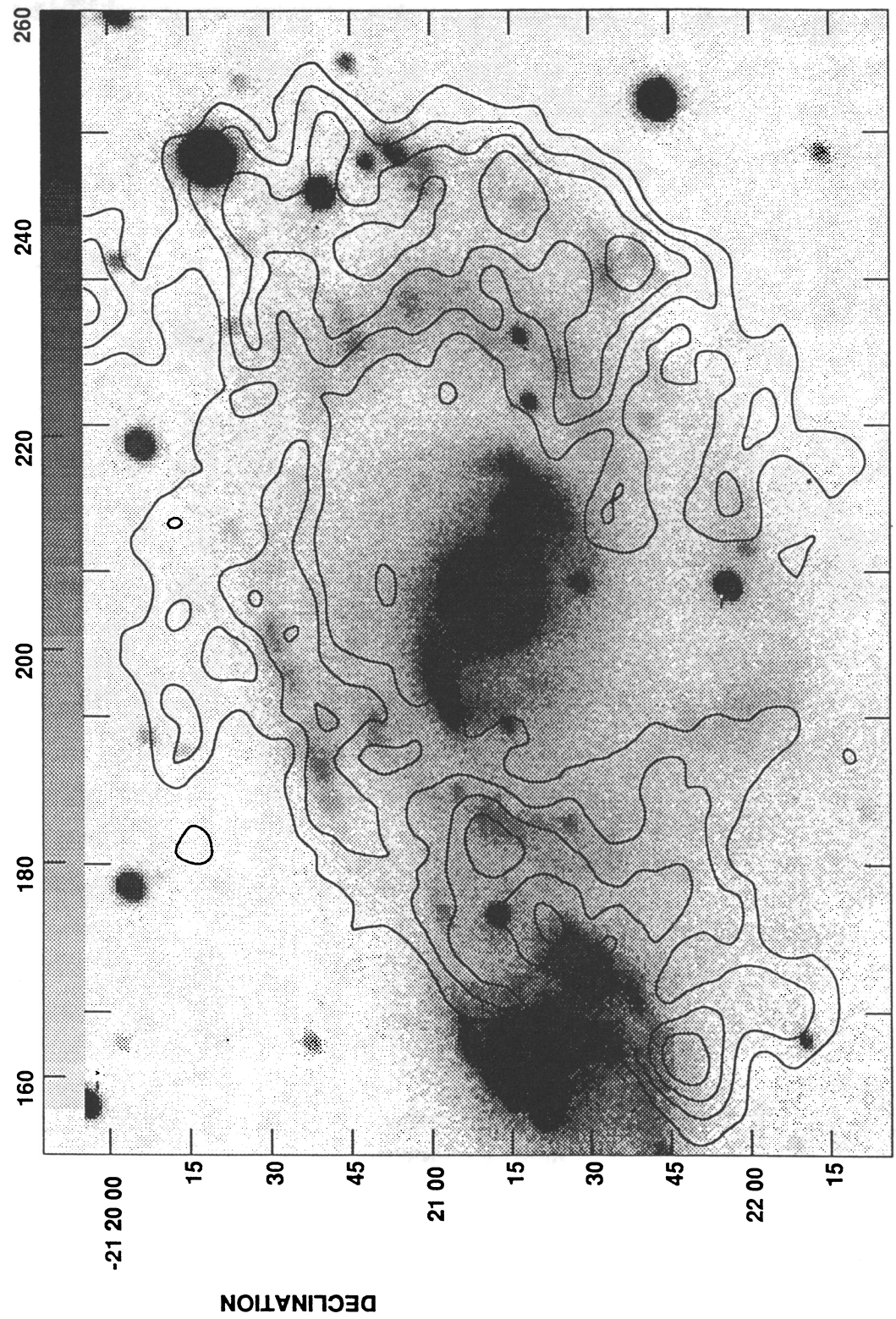

FIG. 17.—The H I ring in NGC 2207 compared with the optical emission. Contours of N(H I) are overlaid on the R-band CCD image in gray scale. The contour levels are 300, 400, 500, and 600 Jy beam^{-1} m s^{-1}, which correspond to H I column densities of 16.4, 21.8, 27.3, 32.7 $M_{\odot}$ pc^{-2}.

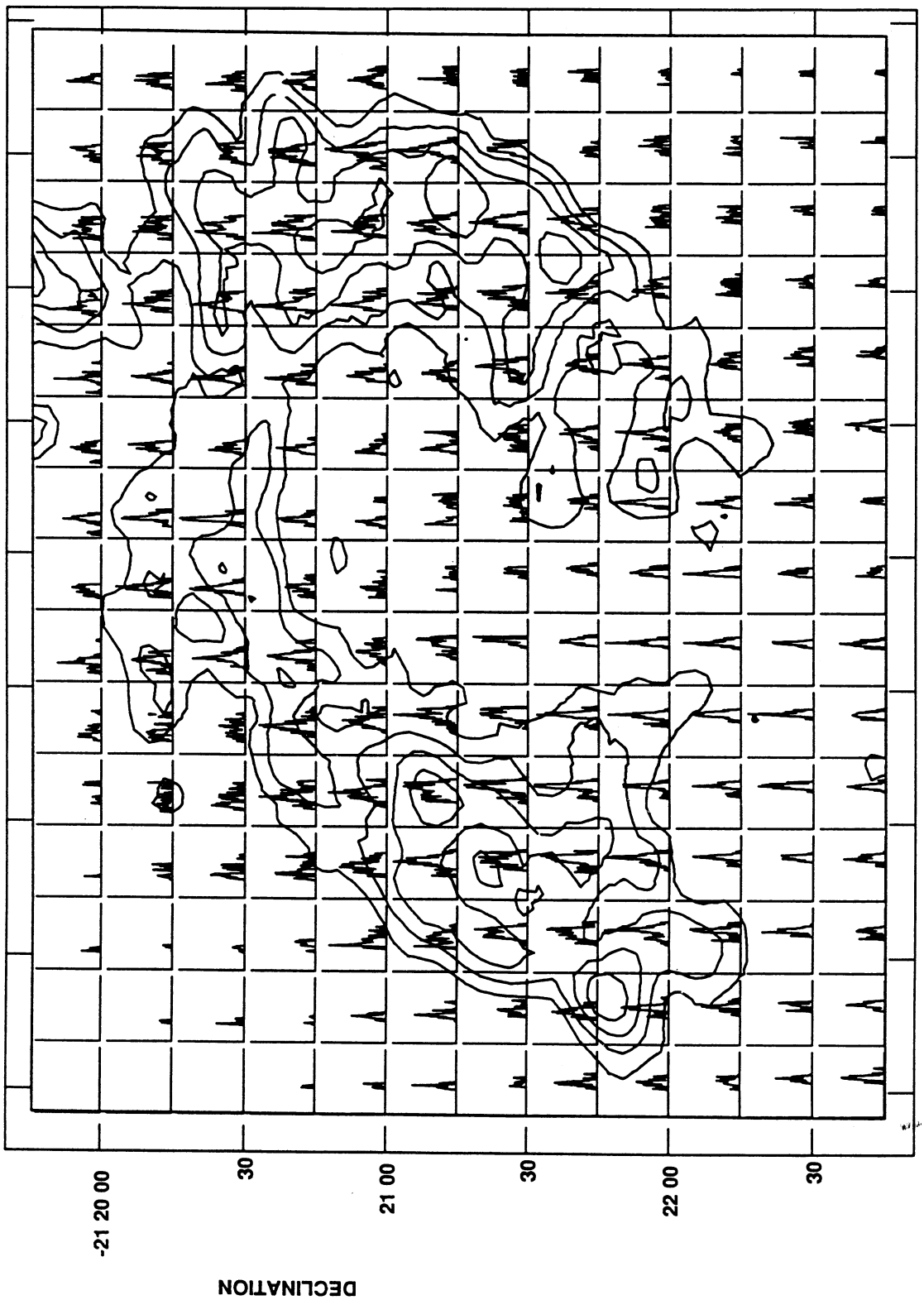

FIG. 18.—Velocity profiles for the H I ring in NGC 2207 with N(H I) contours from Fig. 17 overlaid. These profiles were made from the naturally weighted cube with 5.25 km s^{-1} velocity resolution and 13″.5 × 12″ spatial resolution after removal of the H I emission associated with IC 2163. The velocity scale on the abscissa goes left to right from 3043 to 2465 km s^{-1}, and the surface brightness scale on the ordinate goes from 0 to 10 mJy beam^{-1}. The spectra were obtained from the H I cube, in which only regions of believable H I signal were retained, as described in § 3.1.

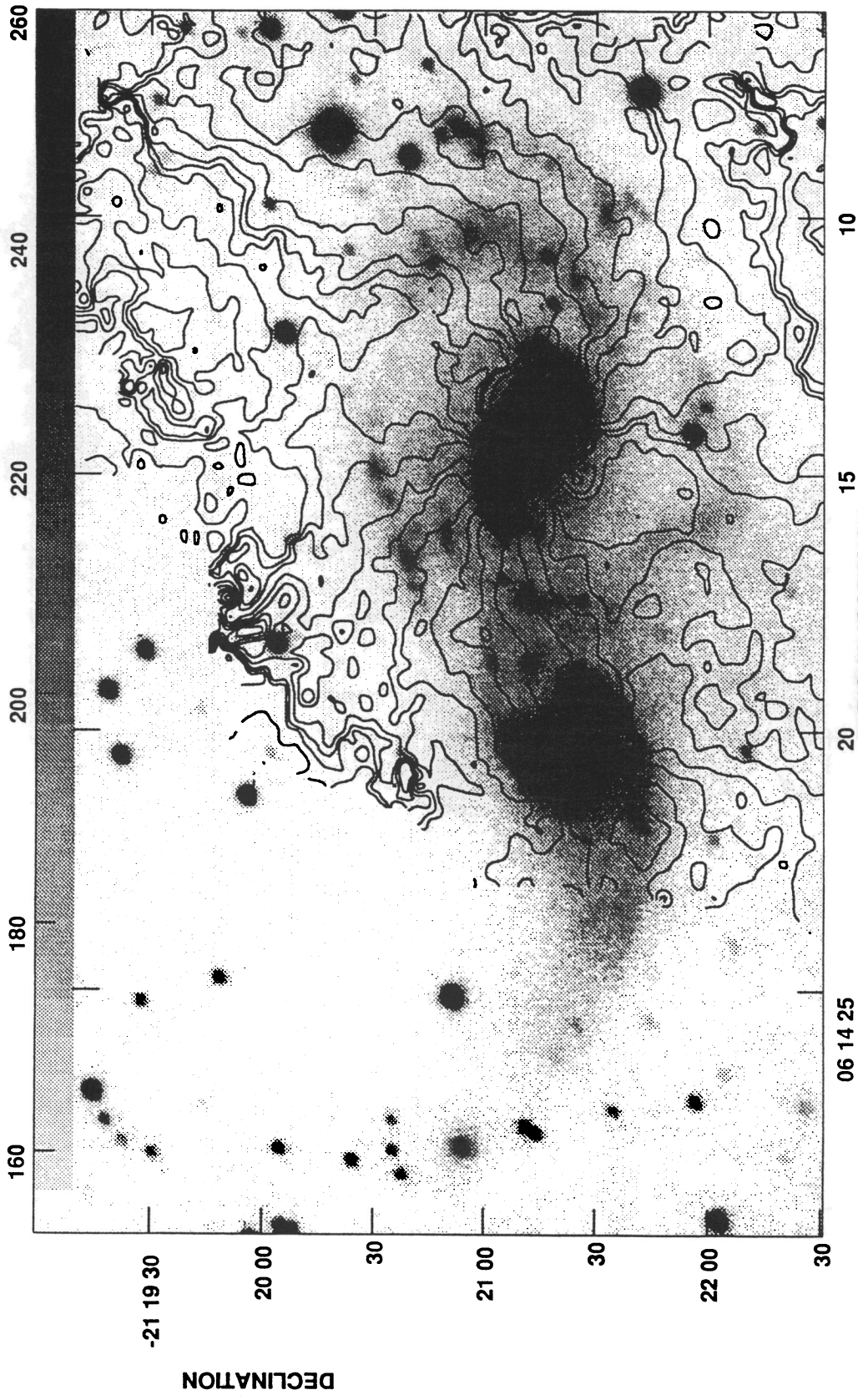

FIG. 19.—Velocity field for NGC 2207 made from the cube with 13″.5 × 12″ spatial resolution and 5.25 km s^{-1} velocity resolution. The isovelocity contours are overlaid on the *R*-band CCD image in gray scale. Contour levels are at 2620, 2640, 2660, 2670, 2680 . . . (20) . . . 2840, 2850, 2860 . . . (20) . . . 2920, 2950 km s^{-1}.

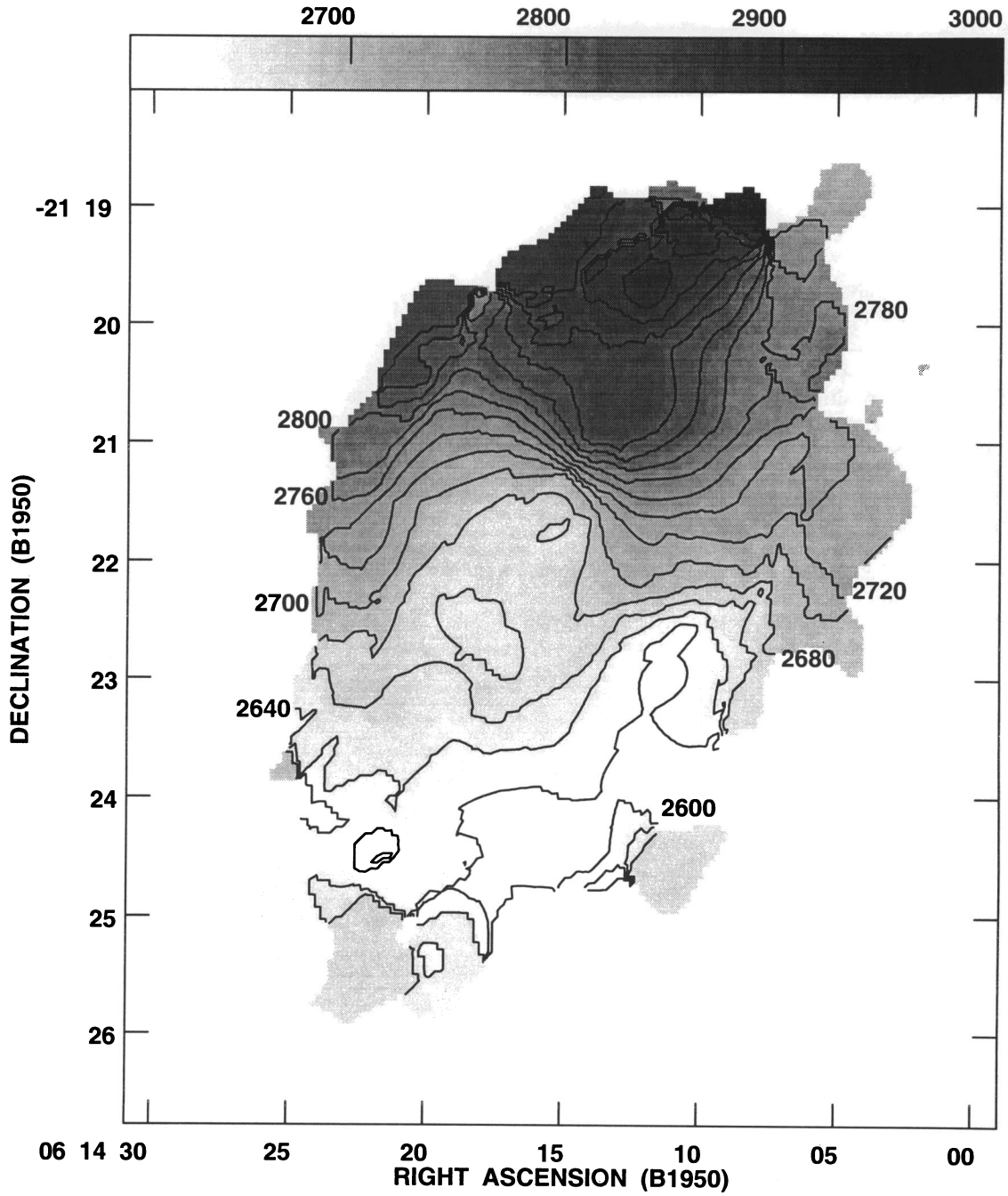

FIG. 20.—A gray scale plus contour display of the velocity field of NGC 2207 made from the cube with 30″ angular resolution and 21 km s^{-1} velocity resolution. The contour levels are 2600 ... (20) ... 2940 km s^{-1}.

dence for rapid streaming at the western end of the bar; for example, in the unseparated channel map displays at 2864–2843 km s^{-1} in Figure 4, contours jut down from the outer galaxy to the southwest end of the bar. The velocities here are higher than in the neighboring bar regions.

Figure 20 shows a gray scale plus contour display of the velocity field made from the cube with 21 km s^{-1} velocity resolution and 30″ spatial resolution. The smoothing emphasizes the large-scale structure, which will be compared in Paper II with the models for the dynamics of the galaxy. Despite the broad line profiles, we see large-scale, coherent structure in both the high-resolution and the low-resolution mean velocity images. The northern part of the galaxy is the receding side. If the spiral arms of NGC 2207 are trailing, and the sense of rotation is clockwise, then side of NGC 2207 nearest to us is in the north.

Table 2 compares various position angles of interest in this galaxy. The following all have position angles close to 60°: the major axis of the barlike feature in the center, the H I kinematic minor axis in the central regions, and the minor axis of the outermost N(H I) contour of the extended H I distribution surrounding the main disk. These axes differ in orientation by about 40° from the 20° position angle of the isophotal minor axis of the H I ring and the main optical disk, and all of these

TABLE 7

STATIC TILTED-RING FITS TO THE VELOCITY FIELD OF NGC 2207

	SOUTHEAST APPROACHING			NORTHWEST RECEDING		
R	v_R (km s^{-1})	P.A.	i	v_R (km s^{-1})	P.A.	i
15″.....	f	f	f	f	f	f
45″.....	188 ± 16	335° ± 0°.4	31° ± 3°	131 ± 11	330° ± 1°	46° ± 6°
75″.....	f	f	f	139 ± 27	339 ± 1	46 ± 8
105″.....	142 ± 13	330 ± 0.5	46 ± 4	144 ± 1	342 ± 0.4	64 ± 1
135″.....	121 ± 0.7	333 ± 0.3	73 ± 2	148 ± 1	336 ± 0.4	81 ± 2
165″.....	179 ± 3	357 ± 0.3	56 ± 2	167 ± 5	331 ± 0.3	86 ± 1
195″.....	165 ± 0.7	354 ± 0.2	71 ± 1	...[a]	...	...
225″.....	158 ± 1	352 ± 0.3	68 ± 2	...	...	...

[a] H I extends to greater radii in the south.

angles differ from the 50° position angle of the minor axis of the best-fit tilted model disk in the warping simulations.

The velocity field has a global S-shaped, or open spiral-shaped, distortion. The kinematic minor axis in the central region has P.A. = 60° ± 3° but rotates counterclockwise through a large angle as the radius increases (see Fig. 20 and Tables 2 and 7). The conclusion of Bosma's thesis (1978) is that S-shaped distortions of velocity contours can be produced either by an oval distortion or by a warp of the disk. Since the barlike feature in NGC 2207 is small, whereas the S-shaped distortion occurs throughout the whole disk, the most likely interpretation of the unusual velocity distribution in NGC 2207 is that it results from a warp in the disk.

In our first attempt to analyze the velocity field, we fitted a static tilted-ring model to the data in Figure 20 by using a version of the GIPSY routine ROTCUR that was adapted to run within AIPS. It assumes circular motions but allows for a radial change in inclination and position angle of the major axis. We restricted the solution to a cone of 25° half-angle about the kinematic major axis to reduce the inclusion of regions with very broad line profiles in the data. Table 7 gives the results when the northwest-receding and southeast-approaching sides are treated separately; annuli that failed to converge are listed with an "f." The values given here are meant to be illustrative only, but they indicate severe distortions in the disk. The model suggests that NGC 2207 is highly warped in the outer parts, with inclinations ranging from 31°–46° at small radii to 73°–86° at large radii. High inclinations at large radii are found on both sides of the galaxy, but the highest values pertain to the northwest-receding side. The asymmetry in the behavior of the velocities in the outer part of the galaxy is evident from the velocity slice along the kinematic major axis in Figure 21*b*. The warp does not appear to be a simple bisymmetric tilt, and the inclinations derived for the major axis cone may not apply elsewhere in the galaxy. The static tilted-ring model finds that the position angle of the kinematic major axis changes with radius, but the twist is not as large as we see for the kinematic minor axis in Figure 20.

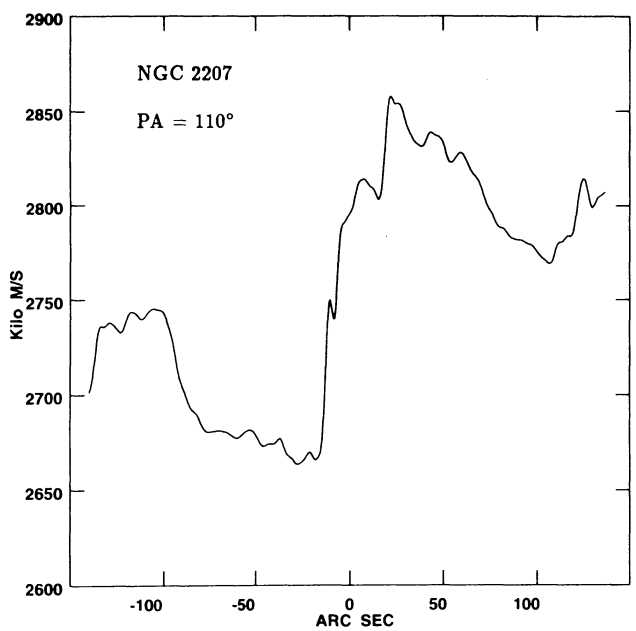

FIG. 21*a*

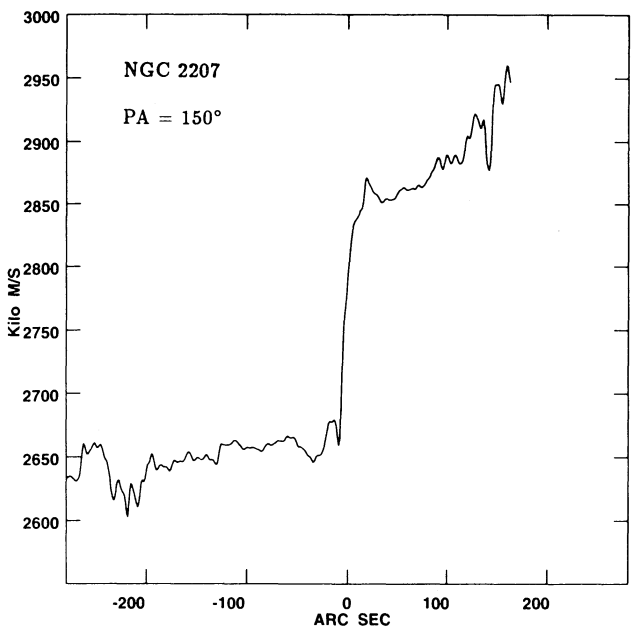

FIG. 21*b*

FIG. 21.—Mean H I velocity vs. position for slices through the nucleus (position 0) (*a*) along the photometric major axis at P.A. = 110°, with east (negative positions) on the left and west on the right, and (*b*) along the kinematic major axis for the central regions at P.A. = 150°, with southeast (negative positions) on the left and northwest on the right.

The maximum value of the rotational velocity in Table 7 is low compared to the typical value in undisturbed, large spiral galaxies.

The very large values obtained for the warp in the static tilted-ring model are problematical because for an interacting galaxy they should be accompanied by large velocities in the z direction (to make the warp), and these z motions are not included in the static model. Therefore, in Paper II, we present detailed simulations of z motions and warps responding to an interaction. These simulations reproduce the velocity anomalies in Figure 20, and they also show in a dynamically consistent way how the disk is likely to be warped in space.

V. Rubin, K. Borne, and C. Peterson (unpublished) measured an optical velocity for the nucleus of NGC 2207 equal to 2745 ± 15 km s^{-1}. The bilaterally symmetric features in the unseparated H I channel maps of Figure 4 suggest that v_{sys} lies in the 2738–2759 km s^{-1} channels. In the mean H II velocity field image in Figure 20, the kinematic minor axis in the central regions has $v_{sys} = 2750 \pm 20$ km s^{-1}. The static tilted-ring model found $v_{sys} = 2760$ km s^{-1} for the kinematic major-axis cone. All of these values are reasonably close, so we adopt the optical value for v_{sys}. Notice that NGC 2207 and IC 2163 have about the same systemic velocity within the uncertainties of the estimates.

Figure 21 shows slices through the mean velocity field (*a*) along the photometric major axis at P.A. = 110° and (*b*) along the kinematic major axis for the central regions at P.A. = 150°. The slice along the photometric major axis is fairly close to the 97° position angle for the optical slit shown in Rubin & Ford (1983) and in Figure 29 below, and the H I velocities in Figure 21*a* mimic the falling rotation curve they found. In IC 2163 the falling rotation curve in the Rubin and Ford figure is a consequence of velocity streaming on the double arm; in NGC 2207 it results from the twist of the isovelocity contours produced by the warp. In both galaxies, the velocities fall in the outer part of the galaxy at certain position angles but rise or remain flat in the outer part of the galaxy at other position angles. The slice at P.A. = 150° in Figure 21*b* appears to show a rotation curve that is flat in the southeast but rises in the outer part of the galaxy in the northwest. Thus, along the kinematic major axis, there is an asymmetry in the radial behavior of the velocities as well as an asymmetry in the gas distribution (greater elongation to the southeast). Such asymmetries can be the result of tidal forces at close range; they also suggest that the orbit of IC 2163 is not in the plane of NGC 2207.

Another way to visualize the mean velocities in NGC 2207 is to look at the velocity-gradient vector field. This is shown in Figure 22, which displays the gradient across the beam in the high resolution velocity field at each location. Proceeding outward from the nucleus along the kinematic major axis, we see the following: (1) large radial gradients near the nucleus, as expected for a spiral galaxy; (2) small gradients at intermediate radii on the northwest and the southeast major axes, as expected for a nearly flat rotation curve, and (3) large nonradial gradients at large radii, particularly on the northern side. The large outer gradients indicate again that some combination of a warp, z motions, and nonradial tidal stretching motions are present in the outer northern part of the galaxy, where the static tilted-ring model yielded high values for the inclination.

Along the kinematic minor axis, which starts at P.A. = 60° in the central regions but rotates to larger angles as the radius increases, Figure 22 shows some velocity gradients directed nearly radially; a slice through the mean velocity field along P.A. = 60° reveals that in the outer part of the galaxy the absolute value of $(v_{obs} - v_{sys})$ increases outward, with $(v_{obs} - v_{sys})$ positive on the northeastern side and negative on the southwestern side. This unusual behavior can be produced by a warp, z motions, or radial flows.

5.4. *Velocity Dispersions in NGC 2207*

Figure 23 shows the velocity dispersion in NGC 2207 as a gray scale with contours of N(H I) superposed. The H I velocity dispersion is high (40–50 km s^{-1}) in a large, butterfly-shaped region that covers much of the main disk of NGC 2207 and corresponds to the distortion of the velocity contours (compare Figs. 23 and 24). The western lobe of the butterfly has an open spiral shape. Because the distribution of the larger velocity gradients in Figure 22 resembles the distribution of gas with high velocity dispersion in Figure 23, we did two tests to see if beam-smearing could account for the unusual velocity dispersions. First, we made a corrected image, shown in Figure 24, of the velocity dispersion by taking the quadratic difference between the observed velocity dispersion and the change in the velocity field across the Gaussian radius of the synthesized beam. There is very little difference between the corrected and uncorrected images of the velocity dispersion because the average gradient is relatively small (see also examples in Table 6). Second, at each pixel in two large fields in NGC 2207, we compared the size of the velocity dispersion with the magnitude of the velocity gradient across the beam to see if there is a correlation. One of the fields is in the western part of the H I ring, 3.6 arcmin^2 in area; the other is in the southern extension, 2.5 arcmin^2 in area. Within each field, there is no correlation between the velocity dispersion and the magnitude of the velocity gradient, although the mean values of the velocity dispersion and the velocity gradient are both greater in the western-ring field than in the southern extension field. Evidently, the large velocity dispersions are not caused by velocity gradients *across* the beam, but they may still result from velocity gradients along the line of sight.

We consider whether the large velocity dispersions could result from the simple geometrical effect of intercepting the disk twice along the line of sight as the disk folds back on itself in a strong warp, as in the static tilted-ring model of Table 7. In that case, in a cone centered on the line of maximum fold, one should find double-peaked or broad line profiles and higher values for N(H I) than where the line of sight cuts through the disk only once. Of course, the line profiles in Figure 18 and the twisted shape of the high velocity dispersion region in Figures 23 and 24 imply that the warped region in NGC 2207 is more complicated than a simple fold. Nevertheless, it is interesting to look for a correlation between N(H I) and velocity dispersion in the data.

Figure 25 compares the values of the velocity dispersion and the H I column density at each pixel in the western-ring field and in the southern extension field. The mean values of the velocity dispersion and N(H I) are both greater in the western-ring field than in the southern extension field. At each value of N(H I) $> 5\ M_\odot$ pc^{-2} within the western-ring field, most of the values for the velocity dispersion lie in the range of 40–50 km s^{-1}, independent of N(H I). However, as N(H I) increases, the lower velocity dispersion tail (below 35 km s^{-1}) decreases, and this produces a weak correlation between the mean values of velocity dispersion and N(H I). Since high values of the velocity dispersion are significant for all H I column densities greater

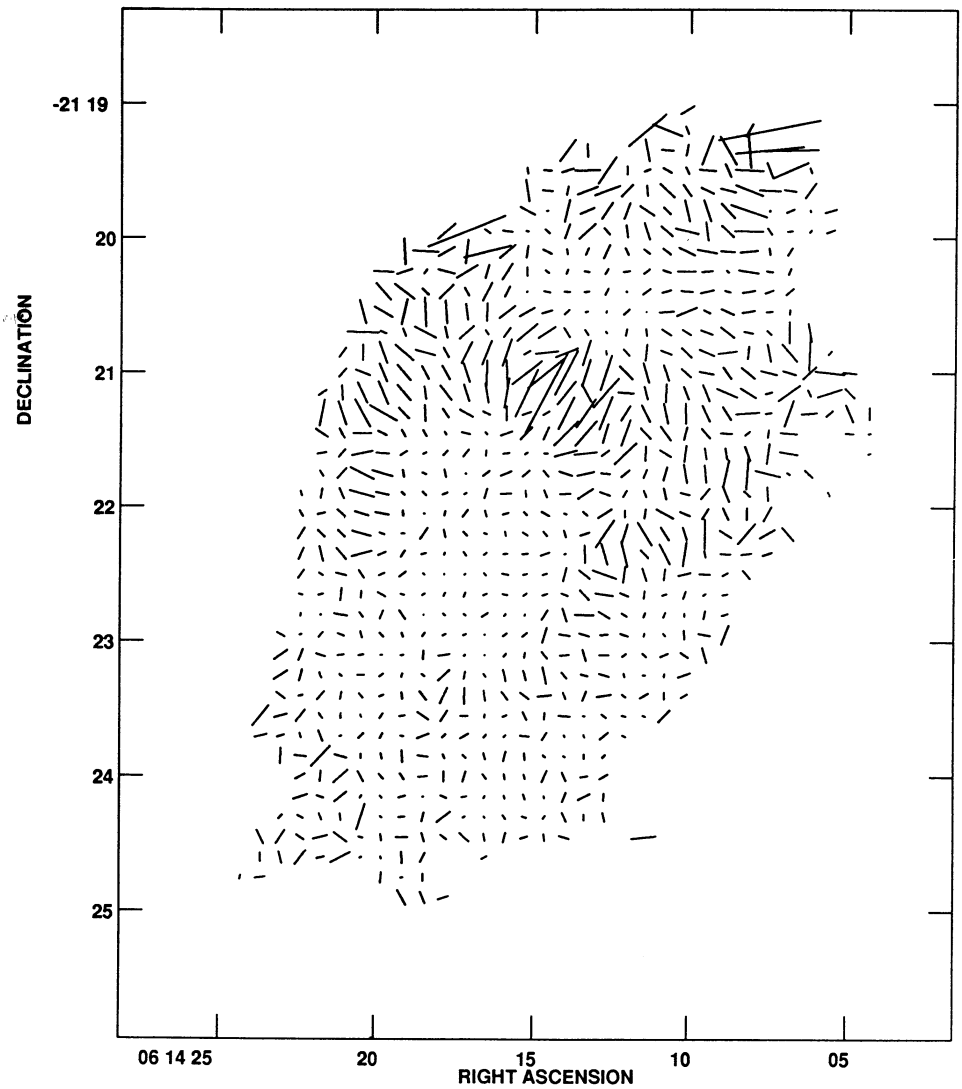

FIG. 22.—The velocity gradient vector field for NGC 2207. Each vector represents the local gradient of the velocity field across the beam; a vector of length 1″ in the image indicates a gradient of 0.333 km s^{-1} arcsec^{-1}.

than 5 $M_\odot$ pc^{-2}, it appears that a simple geometrical effect is not the only factor involved in producing the observed high velocity dispersions. Thus, tidally generated turbulence and, perhaps, stretching motions along the line of sight seem to be required. The correspondence between the S-shaped velocity contours and the region of high velocity dispersion suggests that the same tidal accelerations are involved in producing both of these velocity anomalies.

5.5. *Massive* H I *Clouds in NGC 2207*

Table 6 lists the properties of six giant cloud complexes in NGC 2207. All six occur within the butterfly-shaped region of high velocity dispersion. Like the cloud complexes on the tidal arms of IC 2163, the largest clouds in NGC 2207 have H I masses greater than 10^8 $M_\odot$, high internal velocity dispersions, and mean velocities consistent with the neighboring H I in the disk (see Fig. 18). Although we detect blue-light emission from the vicinities of these clouds on the deep *B* plate, they are not unusually bright in Hα or *B*-band. Radio continuum emission is detected from the H I ring, which contains five of these clouds, and will be described in § 7 below. The massive clouds in IC 2163/NGC 2207 range in radius from 1 to 3 kpc, and most are well resolved in our H I observations.

These clouds in NGC 2207 are somewhat more massive and have slightly higher peak H I column densities than those in IC 2163. They are all pure gas features without obvious counterparts in the old stellar population and without excessive star formation. The clumping in the H I ring in NGC 2207 looks like it was caused by a gravitational instability, as in classical ring galaxies (Theys & Spiegel 1977). In fact, all of the clouds could have formed this way, in which case their large masses would be the result of the high velocity dispersions (Elmegreen et al. 1993).

Two clouds in NGC 2207 deserve further comment. Cloud N2, with a mass of 10^9 $M_\odot$ and a radius of 2.9 kpc, is situated between the western stellar arms and has a maximum N(H I) = 36 $M_\odot$ pc^{-2}, which is high for an interarm region. Cloud N2 is larger than the arm thickness. This implies that it could have formed independently of the arms or that it formed in the arms but was not destroyed when it entered the interarm region. In normal galaxies, the largest clouds (10^7 $M_\odot$) usually occur only in the arms and have densities sufficiently low

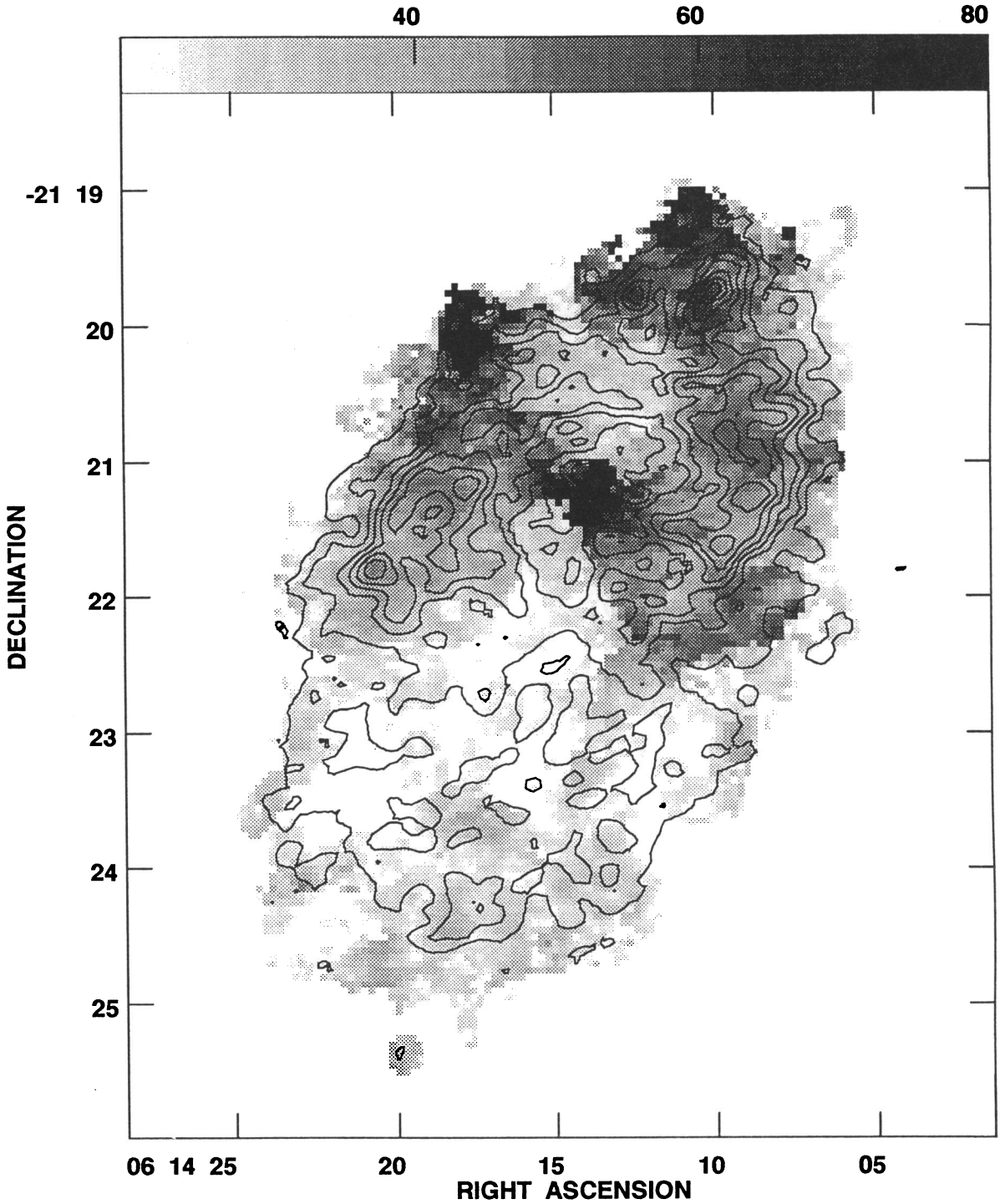

FIG. 23.—Velocity dispersion image of NGC 2207 in gray scale with contours of N(H I) superposed. The velocity dispersion is obtained from the data cube with 5.25 km s^{-1} velocity resolution and 13".5 × 12" spatial resolution. The gray-scale wedge indicates the velocity dispersion and runs from 20 to 80 km s^{-1}. The contour levels are 100 ... (100) ... 700 Jy beam^{-1} m s^{-1}.

(10–30 atoms cm^{-3}) that they can be destroyed by the increasing tidal forces as they enter the interarm region (Elmegreen 1992). The average density in cloud N2 may be similarly low, e.g., if the thickness of the cloud is 500 pc, then the average density is 2.4 atoms cm^{-3}. However, the cloud is so big that it does not fit completely into the arm-to-interarm transition region, where the large tidal force can pull it apart. In fact, the arm is probably a spiral wave that is moving through the cloud without much of a deformation to either.

Cloud N1 is located north of the H I ring but appears to connect to the northwestern part of the ring. The above analysis of the H I velocity field shows that a strong warp and perpendicular motions set in at approximately the distance of cloud N1 from the nucleus. Thus, cloud N1 could be moving

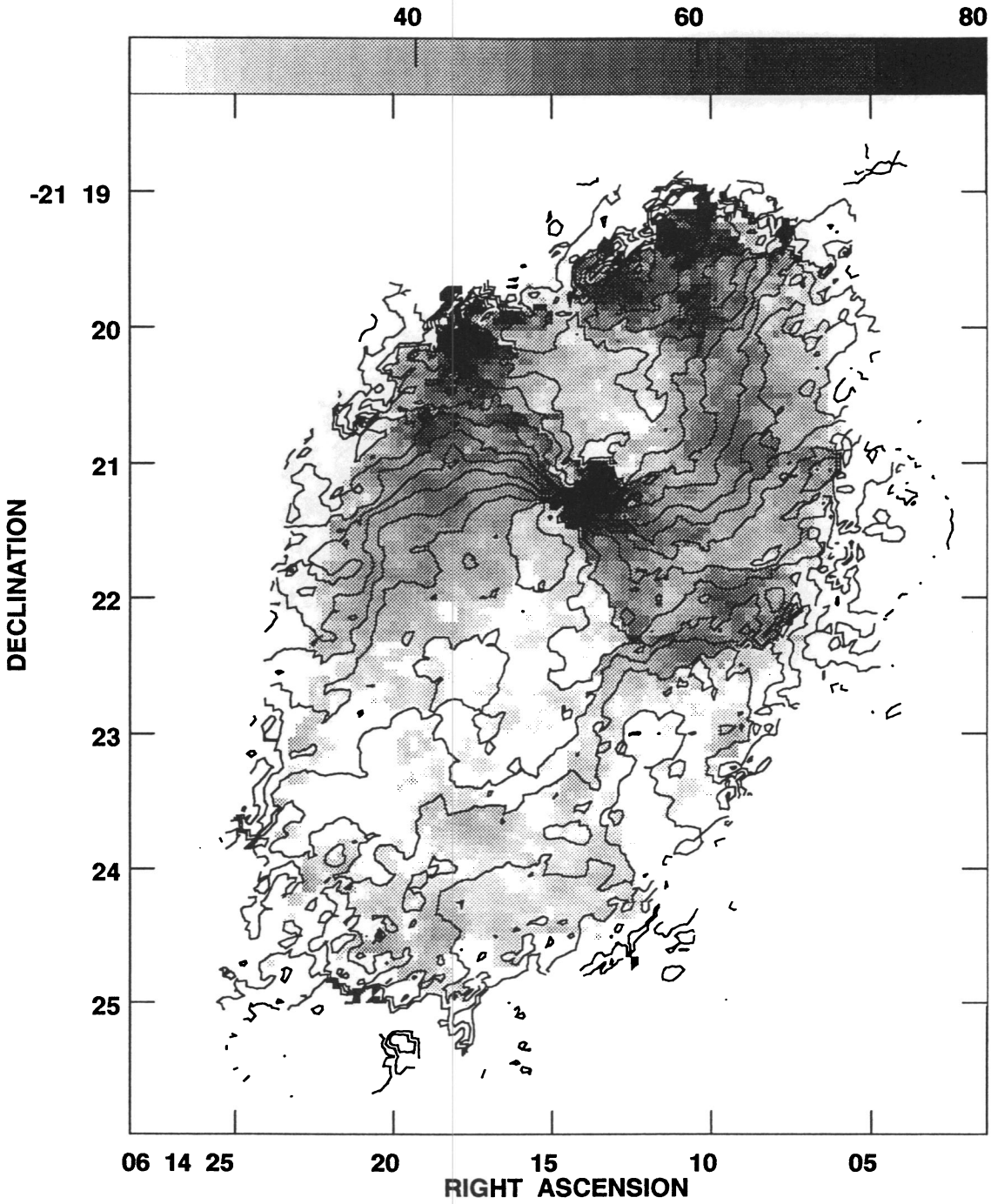

FIG. 24.—Velocity dispersion image of Fig. 23 after correction for velocity gradients across the beam. The velocity dispersion is shown in gray scale with contours from the mean velocity field of Fig. 19 overlaid. The contour levels for the velocity field are 2600 ... (20) ... 2940 km s^{-1}. The gray-scale wedge runs from 20 to 80 km s^{-1}.

away from the main disk in the perpendicular direction as a result of the tidal encounter. *N*-body simulations of outer rings by Elmegreen et al. (1992) imply that tidal encounters can destroy rings as some particles plunge to the center while others gain angular momentum and escape in tidal tails. Cloud N1 and the short, thick tidal arm containing it could be the result of such an action. Elmegreen et al. (1993) suggest that this cloud may escape from NGC 2207 to form an independent dwarf galaxy or intergalactic cloud in the future. Cloud N1 is not detected in the radio continuum, but on the deep *B* plate in Figure 1*c*, a blue-light patch (an arclike feature, too faint to be seen on the *B*-band CCD image) coincides with the northwestern part of this massive H I cloud and may indicate that some weak star formation is occurring. The mean corrected H I velocity dispersion in this blue-light patch is 49 km s^{-1}, which is somewhat smaller than in the rest of the cloud.

In NGC 5774, which is a member of the interacting pair NGC 5775/4, Irwin (1994) finds large regions with H I velocity

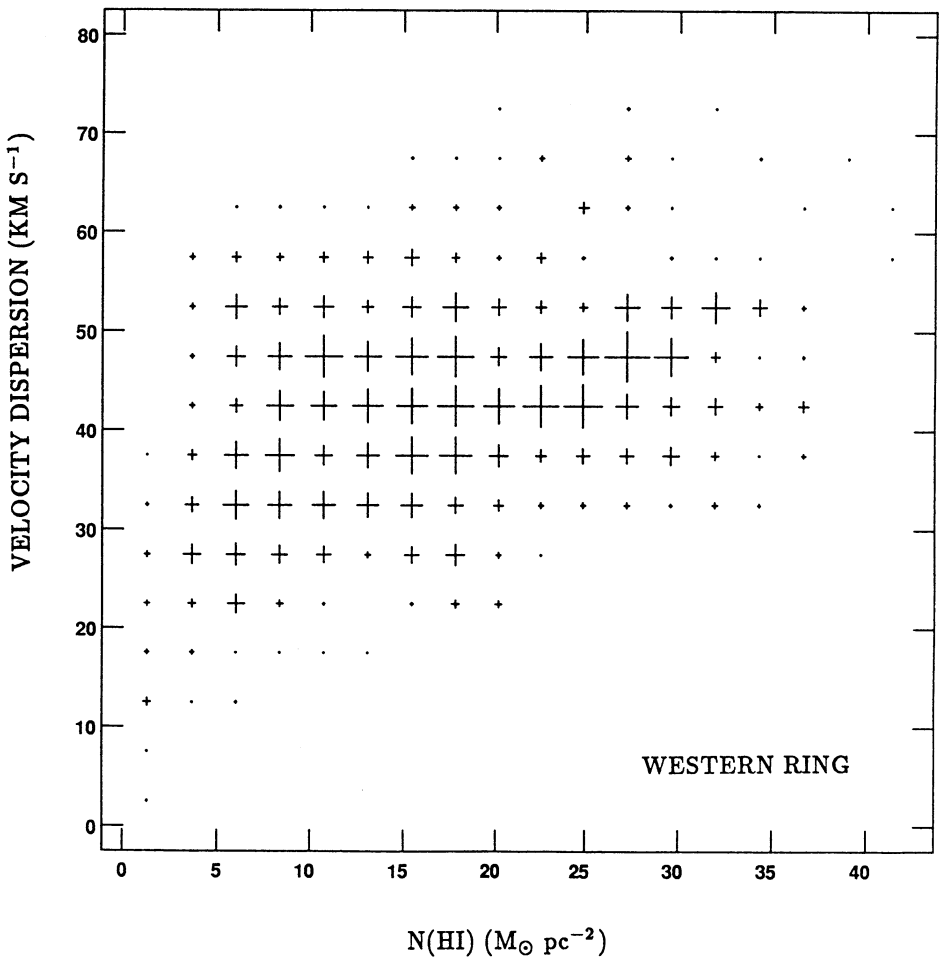

FIG. 25a

FIG. 25.—Velocity dispersion vs. N(H I) for (*a*) the western-ring field, which encompasses the western side of the ring and its short northwestern extension to cloud N1, and for (*b*) the southern extension field, which comprises the western part of the large southern extension to the H I emission from NGC 2207. In each plot, the pixels were binned, and the symbol size represents the number of points in the bin.

dispersions of approximately 50 km s^{-1}. She also identifies 3 H I clumps with these high dispersions, no apparent optical counterparts, and masses in the range 10^7 to 10^8 $M_\odot$. Both galaxies have relatively high H I velocity dispersions (it would be difficult to detect clumps in NGC 5775, which is seen edge-on), which she attributes to tidal agitation. This appears to be another example of what we see in the IC 2163/NGC 2207 system.

6. BROADBAND OPTICAL SURFACE PHOTOMETRY OF IC 2163 AND NGC 2207

6.1. *The Eastern Tidal Arm of IC 2163*

Azimuthal profiles from the deprojected, sky-subtracted *R*- and *B*-band CCD images were made in order to study the eastern arm of IC 2163. The projection parameters from § 4.3 were used: the position angle of the line of nodes of the projection equals 65°, and the disk inclination is 40°.

Figure 26 shows the azimuthal profiles around the eastern arm of IC 2163 in *B* (*bottom*) and *R* (*top*) bands at the three indicated values of the face-on radius. The profiles are averaged over radius in radial steps of 8″ = 1.4 kpc to improve the signal-to-noise ratio. The plotted angular coordinate is measured in degrees counterclockwise from the northern line of nodes of the projection. In doing the radial averages on the arm, the angular coordinate of each radial step inside the average was shifted as a function of radius so that the crest of the spiral arm is always at the same angular bin; this compensates for the spiral pitch and prevents smearing of narrow features.

In the profiles at 59″ radius, the eastern arm is the broad feature visible from 20° to 70°, while the very red feature at approximately 90° coincides with one of the southern streamers from NGC 2207. In all of the profiles, the arm is asymmetric, the *R*- and *B*-band arms are similar, and contamination by NGC 2207 is significant for azimuthal angles greater than 120°.

The surface brightness in the interarm region at angles of −45° to 0° is so low in both bands that it gets lost in the sky noise. This low interarm intensity is unusual for spiral arms, which tend to have arm-interarm contrasts of only 1 or 2 mag. Here the contrast is at least 5 mag in *B* and *R* bands for the northern interarm. Such a low interarm intensity is consistent with the model results, which show that at this stage of the interaction nearly all of the stars and gas are cleared out of the interarm regions and put into the inner oval and double arm.

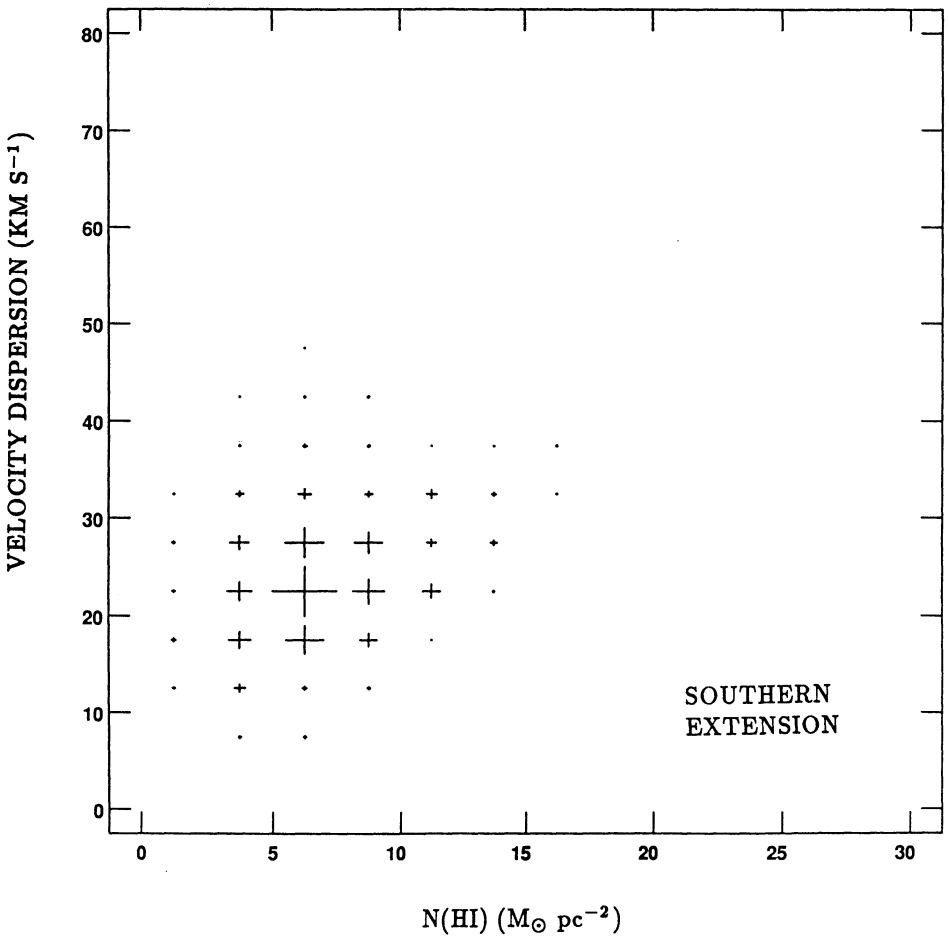

FIG. 25*b*

The arms of IC 2163 are not density waves, but young material arms that contain almost all of the stars at those radii.

The arm profiles of the tidal arm in Figure 26 have a sharper gradient at the leading edge (south and higher angles) than at the trailing edge. This asymmetry is also apparent in Figure 1. In the *B*-band profile at 59″ radius, the tidal arm ridge (the southern ridge) has an azimuthal angle of 57°, and the streaming arm ridge (the northern ridge) is at 43°. The ridge-to-valley contrasts are generally greater in H I (see Table 5) than in *B* band and greater in *B* band than in *R* band. The tidal and streaming ridges have similar $B-R$ colors, but the valley between them is redder by 0.2–0.3 mag. The color difference could result from obscuration by dust, enhanced star formation on the ridges, a change in the relative distribution of stars and gas along the line of sight, or a difference in the velocity dispersion of young and old stars, which would reduce the ridge-to-valley contrast in *R* band relative to *B* band. If a foreground screen of dust were responsible for the color difference in the valley, then the corresponding excess visual extinction would be 0.3–0.4 mag, and the corresponding excess gas column density would be about 5 $M_\odot$ pc^{-2}. If the dust were distributed as a Gaussian throughout the height of the disk, then the excess gas column density in this feature could be higher, possibly 10 $M_\odot$ pc^{-2} (Elmegreen 1980). Such gas is not in the form of H I (see § 4.2 above). Considering the velocity differences, the two ridges in the tidal arm are most likely separate crests of enhanced star and gas densities, with excess star formation on the crests and a small amount of dust extinction between them.

The upper graph in Figure 27 shows the radial surface brightness profile along the eastern arm of IC 2163. The plotted values start at the apex of the oval and measure the peak intensities on the arm. The strong emission near the end of the optical arm at a face-on radius $R = 110''$ to 120″ is from the dwarf elliptical galaxy, which is several tenths of a magnitude redder than the average color of the eastern arm of IC 2163. The optical arm extends out to at least $90'' = 15$ kpc from the nucleus. The radial arm profile has an approximately exponential decrease in surface brightness with a scale length of 29″ (or about 5 kpc) in *B* and *R* bands. There is a broad peak at radius $R = 55''$ from an emission patch (visible also in Fig. 1) that is slightly redder than the rest of the arm.

6.2. *The Radial Profile of the Western Side of NGC 2207*

The lower graph in Figure 27 shows the radial surface brightness profile of the western side of NGC 2207. The plotted values are the mean intensities at each radius, averaged inside a box west of the nucleus measuring ±26″ north-south of the nucleus. For the de-projection, we used the 110° position angle of the photometric major axis (see § 5 and Table 2) and took the inclination as 35° from model fits in Paper II (the static tilted-ring fits in Table 7 gave inclinations of 31° to 46° at small radii). The qualitative behavior of the radial profile of interest here is not particularly sensitive to these values. The western

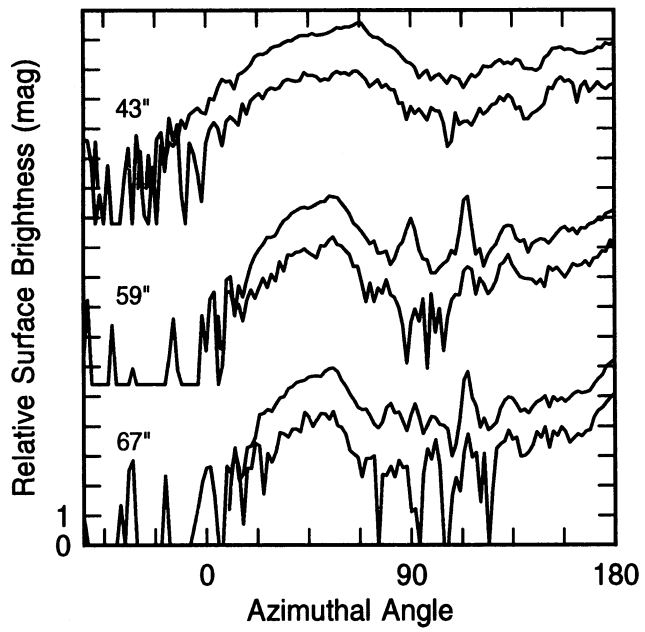

FIG. 26.—Averaged azimuthal profiles of IC 2163 in annuli of width 8″ = 1.4 kpc centered on the indicated face-on radius. The angle is measured in degrees counterclockwise from the northern line of nodes of the projection, which is taken as 65° from the north. The *R*-band profile is on top of the *B*-band profile at each radius. The tick marks on the vertical scale occur at 1 mag arcsec^{-2} intervals.

side of NGC 2207 has a relatively flat radial intensity profile. The plateau in the radial profile from 40″–90″ is not obvious from the optical images in Figure 1, although the deep *B* image shows considerable blue emission between the two arms there. The bright features at 55″ and 85″ are the two spiral arms in the west; the bright spiral stub at the end of the oval contributes near 25″ (the very bright peak at 18″ is a foreground star). There is a sudden drop in intensity beyond 90″ in the west, also apparent in the deep *B* image. The relatively flat part of the profile in NGC 2207 is unusual for galaxies, but it corresponds well to the broad ring of H I emission, which peaks at 70″. De Vaucouleurs & Buta (1980) classify NGC 2207 as having a pseudoring with radius = 25″ × 15″. This refers to the arc of H II regions visible just south of the nucleus in Figure 1*b*, not the plateau shown in Figure 27 at *R* = 40″ to 90″.

7. OTHER DATA

7.1. *Radio Continuum*

Figures 28*a* and 28*b* show our images of the combined $\lambda = 20$ cm radio continuum emission from both galaxies. In Figure 28*a*, the radio continuum image made with uniform weighting (resolution 10″ × 6.5″) is displayed as contours overlaid on an *R*-band image in gray scale; radio continuum emission is prominent from the eyelid regions of IC 2163, from the southern part of the eastern apex of the oval in IC 2163, from a ridge along the eastern to northern side of NGC 2207, and from portions of the spiral arms in NGC 2207. In Figure 28*b*, *N*(H I) contours of the H I ring in NGC 2207 are overlaid on a gray-scale display of the naturally weighted $\lambda = 20$ cm continuum image. The radio continuum image in Figure 28*b* is very similar to the $\lambda = 20$ cm maps of this galaxy pair made with 15″ resolution by Condon (1983) and Hummel et al. (1985). Condon finds a total $\lambda = 20$ cm flux density *S*(20) of 353 ± 19 mJy for the system. As his broadband continuum maps are superior to our average of the line-free channels, we rely on his published data.

In terms of resolution and sensitivity, the best $\lambda = 20$ cm image of these galaxies is Condon's (1983) 7.″5 × 6″ resolution map, which clearly shows the ocular shape of IC 2163 and the emission from the eastern arm of IC 2163, in addition to the features already noted in Figure 28. In the radio continuum, the southern ridge of the double arm is brighter than the valley. This implies that there is no strong shock in the valley and that the southern ridge has enhanced star formation and/or a compression of magnetic fields and gas. The *N*(H I) image shows the compression of the gas on the southern ridge (see the values of the ridge-to-valley contrast in Table 5), and the *B*-band and Hα images (see Figs. 1 and 26) provide evidence of some excess star formation on the southern ridge.

All of the radio continuum images have a very bright, discrete source on the outer western arm of NGC 2207. Its $\lambda = 20$ cm flux density *S*(20) is 22 mJy, which is too bright for a collection of H II regions, i.e., if the most luminous H II region in M51 (van der Hulst et al. 1988) were at the distance of NGC

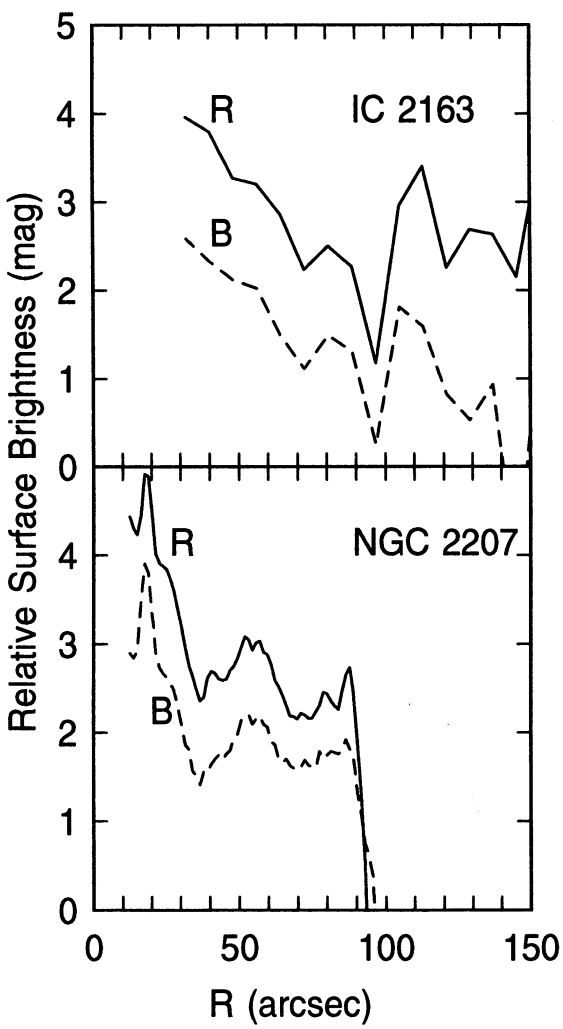

FIG. 27.—Radial surface brightness profiles for the eastern arm of IC 2163 (*top*) and for the western side of NGC 2207 (*bottom*) in *R* (*solid line*) and *B* (*dashed lines*).

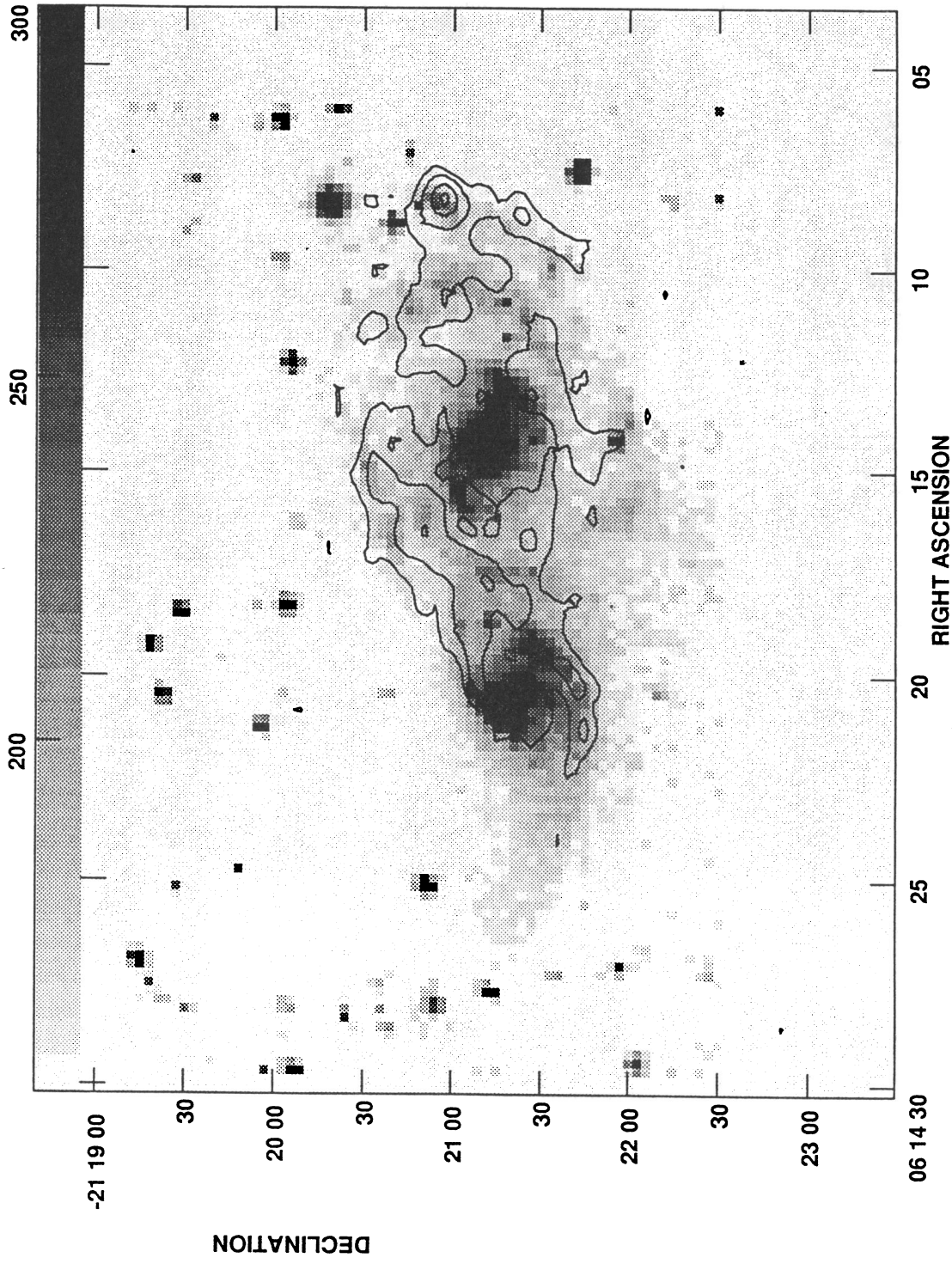

FIG. 28*a*

FIG. 28.—(*a*) Radio continuum emission at $\lambda = 20$ cm from both galaxies as contours overlaid on the *R*-band image in gray scale. The radio continuum image was made with uniform weighting and has a spatial resolution of $10'' \times 6''.5$ and an rms noise of 0.37 mJy beam^{-1} or 3.4 K. The contour levels are at 3, 6, 12, 24 times the rms noise, and the lowest contour level corresponds to a flux density of 1.1 mJy beam^{-1}. (*b*) The correspondence between the H I ring (*contours*) in NGC 2207 and the combined radio continuum emission (*gray scale*). Both images have $13''.5 \times 12''$ spatial resolution and were made from naturally weighted data. The rms noise in the radio continuum image is 0.33 mJy beam^{-1} or 1.2 K. The gray-scale wedge runs from 1 to 10 mJy beam^{-1}; the contour levels are 100 ... (100) ... 700 Jy beam^{-1} m s^{-1}.

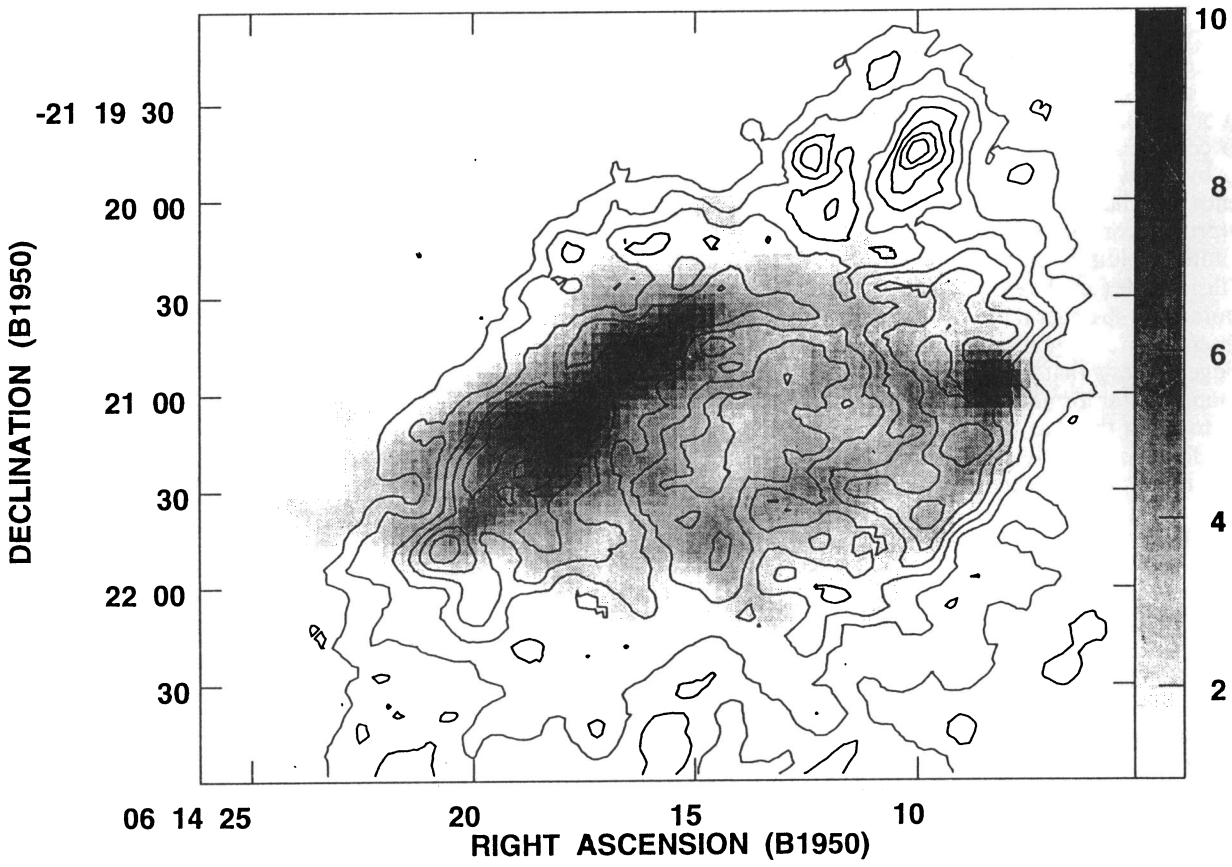

FIG. 28*b*

2207, it would have $S(20)$ equal to 0.14 mJy. In the $\lambda = 6$ cm and $\lambda = 20$ cm A-array VLA observations by Vila et al. (1990), this bright source is resolved and has a spectral index of -0.9. It is probably a background radio galaxy that accidentally coincides with the spiral arm; in the following description, we ignore it. We do not detect H I absorption against this background source.

Condon (1983) points out the central hole in the radio continuum emission from NGC 2207 (see also Fig. 28). This hole is highly unusual for radio-bright spiral galaxies with barlike distortions and indicates that the center of NGC 2207 does not contain either bright star-forming regions or an active galactic nucleus. In particular, the bright spiral arm stubs that emerge from the nuclear region in the optical images are not major sites of massive star formation.

Figure 28*b* shows that the $\lambda = 20$ cm continuum emission corresponds well with the H I ring in NGC 2207 and thus supports the idea that the H I ring is a feature of dynamical significance. But unlike the H I emission (either before or after separation of the contributions of the two galaxies) and unlike the optical emission, the radio continuum emission from this system is strongly one-sided, with the strongest emission coming from the eastern to northeastern side of the ring. We call this feature the "eastern ridge." (Note that the northeastern side is not in the region of overlap with IC 2163.) On the eastern side of the ring, the H I and the radio continuum ridges are displaced from the stellar arms. If the radio emission from the eastern ridge were mainly free-free emission, then the visual extinction, and hence the column density of molecular hydrogen, would have to be very large here. The more likely interpretation is nonthermal emission involving compressed magnetic fields and cosmic-ray gas, especially since the two galaxies have a combined spectral index of -0.92 (Condon 1983), which is strongly nonthermal. A large contribution to this index must come from the eastern ridge, which has a $\lambda = 20$ cm flux density above 6 mJy beam^{-1} (in the full-resolution, naturally weighted image of Fig. 28*b*) equal to 85 mJy, or 26% of the total $S(20)$ from the two galaxies (ignoring the point source in the west). Active star formation would give rise to a flatter integrated spectral index.

The brightest radio continuum source in the eastern ridge is the massive H I cloud N6, which is not particularly bright optically (see Figs. 15 and 17). Its location at a fork in the H I ridge suggests intersecting gas streams. The velocity structure here is complex, with overlapping features in broad line profiles (see Fig. 18). The velocity dispersion is greater in cloud N6 than in the H I fork headed east or the H I fork headed south from this cloud.

The eastern ridge of the radio continuum emission looks like a 10 kpc long shock front with some substructure. It would appear to result from the proximity of IC 2163. We consider what could have caused the compression of magnetic fields and cosmic-ray gas. Two possibilities are shocks produced by tidally generated streaming of gas within NGC 2207 and shocks produced by accretion of gas from the IC 2163 tidal bridge (currently southeast of the NGC 2207 nucleus). The accretion hypothesis needs to satisfy the time and orbital constraints discussed in Paper II. On the other hand, the high

values for the velocity dispersion on the eastern and western lobes of the ring indicate a tidal agitation of the gas that could lead to gas compression and shock fronts. In § 5.3, we noted some unusual radially directed velocity gradients on the kinematic minor axis of NGC 2207, just beyond the eastern ridge of the radio continuum emission. While such gradients can be explained by the warp and z motions, they may also indicate the presence of radial gas flows. For tidal forces at close range, G. Byrd (private communication) points out that early in the postencounter evolution, the strongest shocks should be found on the collision side (i.e., the eastern side of NGC 2207) because the tidal forces are stronger there.

The absence of strongly enhanced Hα emission from the eastern ridge suggests that either there is a time delay between compression and star formation, or there is a condition for star formation to begin that has not yet been satisfied. Indeed, the *IRAS* FIR flux from the IC 2163/NGC 2207 pair is weaker than expected from the well-known FIR/radio correlation. For this galaxy pair, the q parameter, defined by Helou, Soifer, & Rowan-Robinson (1985) as the logarithm of the ratio of FIR to radio continuum flux density, is 1.86, whereas for various samples of galaxies, the median value of $q = 2.3$ with an rms scatter less than 0.2 (Condon 1992).

Evidence for large-scale shocks between colliding galaxies was reported by Sargent & Scoville (1991) and van der Werf et al. (1993), who observed shock-heated H_2 in a merging pair. The interacting pair NGC 5775/5774 shows mass transfer from NGC 5774 to NGC 5775, which exhibits enhanced emission in the FIR and radio continuum (Irwin & Caron 1994). Huang et al. (1994) also find enhanced radio continuum emission in the parts of the disks between two interacting galaxies.

7.2. *Comparison between Optical and* H I *Velocities*

Spectroscopic emission-line velocity data at 679 points along 13 optical slit position angles covering both galaxies were obtained by V. Rubin, K. Borne, and C. Peterson (unpublished) using the 2.1 m KPNO telescope, as part of a separate study. They measured velocities from Hα and [N II] 6583 lines, with typical errors of 10 to 15 km s^{-1}, and kindly made these data available to us. For comparison with the optical velocities, we used the H I mean velocity image (13.″5 × 12″ resolution) of the combined contributions of the two galaxies and made slices along the same directions as the optical observations. If the H I disk has a substantial scale height, then the Hα velocities are more likely to represent what is going on in the central plane.

Figure 29 compares the mean H I velocities and the mean optical velocities as a function of radial distance from the nucleus of NGC 2207 for a slice at P.A. = 97° passing through the nuclei of both galaxies, i.e., along the slit shown in Rubin & Ford (1983). The displacements in this plot are given relative to the nucleus of NGC 2207. In the original plot of the optical data in Rubin & Ford (1983), there is an approximately 20 km s^{-1} range of velocities at each position. Within the uncertainties, there is very good agreement between the optical and the H I velocities along most of this slice. This is comforting, given the large velocity dispersions in much of the gas. The launch point for the streaming arm on the eastern side of IC 2163 is located at $r = -104''$, P.A. = 96.°9 relative to the nucleus of NGC 2207; the optical emission at $r = -107''$, $v = 3007$ km s^{-1} in Figure 29 comes from the vicinity of the launch point. The channel maps in Figure 4 show that there is significant H I gas here at 3011 km s^{-1}, i.e., at the same velocity

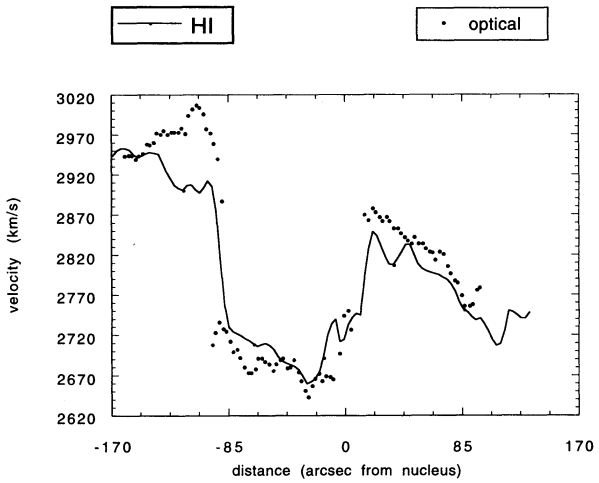

FIG. 29.—Comparison of the mean velocities obtained from H I (*solid line*) and optical (*symbols*) observations along a slice passing through the nuclei of both galaxies at P.A. = 97°. The optical data are from Rubin & Ford (1983). The H I velocities and the optical velocities include contributions from both galaxies. The abscissa gives the displacement (positive to the west) from the nucleus of NGC 2207. The nucleus of IC 2163 is at − 83″.

as the optical emission. The apparent discrepancy between optical and H I velocities at this location in Figure 29 arises because the mean H I velocity includes contributions from both galaxies here.

For the complete set of optical measurements, the optical velocity and the H I velocity measured on the mean velocity image generally differed by less than 40 km s^{-1}. Considering the large velocity dispersions in much of the gas, velocity differences of 40 km s^{-1} between Hα and H I could just represent differences between various clouds along the line of sight. In NGC 2207, we find no systematic difference between the values of v(H I) − v(opt) inside the butterfly-shaped region of high H I velocity dispersion and those outside. There is one slit which crosses the double arm in IC 2163 beyond the launch point. It gives a velocity of 2976 km s^{-1} on the northern component of the optical arm and a velocity of 2922 km s^{-1} in the valley between the tidal and streaming ridges and thus shows the same sense of velocity jump as the H I data.

In the few cases where very large differences occur between the mean H I and optical velocities, we examined the H I line profile to see if there is H I gas at close to the same velocity as the H II emission. The only location with a large discrepancy between the optical and H I velocities occurs in IC 2163 at $\alpha = 06^h14^m20^s.35$, $\delta = -21°20'52''$. In Figure 1*b*, an H II region is visible here 15″ north of the northern eyelid. The optical velocity is 45 km s^{-1} greater than the closest peak above 2 times the rms noise in the H I line profile, i.e., we detect H I but not close to the velocity of the ionized gas. Since our H I spatial resolution is too low to detect the kinematic effect of a supernova remnant, this could be an H II region in a giant molecular cloud traveling at a higher velocity than the H I gas.

8. CONCLUSIONS

The observations of IC 2163 find the following features predicted by the N-body galaxy encounter simulations of ESES: (1) two tidal arms located symmetrically on opposite sides of the nucleus, (2) an oval shape of the disk after de-projection to a face-on image, (3) two orbit streams that differ by 70–100 km s^{-1} on the tidal arm opposite the companion, (4) rapid stream-

ing along the eyelid, (5) a nearly constant velocity along the streaming ridge of the double arm, (6) a nearly constant velocity on the long extension of the tidal tail, and (7) the collection of nearly all the stars beyond the oval into the tidal arm. The observed clumping into massive cloud complexes is explained by the analysis of Elmegreen et al. (1993). The agreement with the model implies that closest approach occurred within the past half- rotation of IC 2163 and that NGC 2207 moved in a prograde, approximately in-plane orbit relative to IC 2163. This knowledge makes it easier to deduce the orbits of the two galaxies.

The observations of NGC 2207 show no obvious tidal arms but they do show (1) a prominent S-shaped distribution of H I velocities and high velocity dispersions, (2) a large ring in H I and the radio continuum, and a plateau in the distribution of optical light midway out in the disk, (3) massive cloud complexes similar to those in IC 2163, (4) a large pool of H I gas and optical filaments that extends southward to 4′ radius, which is about 40 kpc, and (5) strongly enhanced radio continuum emission from the companion side of the ring, perhaps indicating a shock front. The ring appears to open up in the south (Fig. 16), as if much of the material in the southern extension were originally in the ring. The prominent kinematic warp and lack of tidal arms suggest that the tidal forces acted mostly in a direction perpendicular to the plane.

The ring in NGC 2207 could have existed prior to the encounter. It could have been formed by the bar in NGC 2207, which may have moved some of the central gas to an orbital resonance (Schwarz 1981), or by viscous accretion to a turnover radius of the rotation curve (Icke 1979). In that case, the recent encounter with IC 2163 could have stretched the southern part of the ring on the collision side and made the southern extension from this ring gas. The ring may also have resulted directly from the collision with IC 2163 (Theys & Spiegel 1976, 1977; Lynds & Toomre 1976; Appleton & Struck-Marcell 1987; Gerber, Lamb, & Balsara 1992). Classical ring galaxies are produced by perpendicular collisions, with incomplete rings resulting when the collision is off-center. However, the simulations and basic structure of IC 2163 suggest that this galaxy did not pass through the central disk of NGC 2207; otherwise, IC 2163 would be much more distorted than it is. Also, the inner region of NGC 2207 contains an H I hole and a radio continuum hole but not a hole in the stellar distribution (see Fig. 27).

The presence of southern streamers in the deep B image of NGC 2207 and the near equality between the total H I mass north and south of the nucleus (despite the fact that the gas distribution is more elongated to the south) suggest that the southern extension of low-density H I was produced by tidal stretching.

The gas in the southern extension of NGC 2207 has a lower velocity dispersion than the gas in the butterfly-shaped region (see Figs. 24 and 25). In fact, both IC 2163 and NGC 2207 have relatively low velocity dispersions in the most extended, low-density H I structures, i.e., in the long faint part of the tidal tail in IC 2163 and in the southern extension of NGC 2207. Elsewhere the velocity dispersions are higher. Perhaps these low dispersions in the southern extension and other low-density tidal features are the result of an adiabatic decompression of the turbulent gas during the tidal expansion.

Neither galaxy is currently undergoing a burst of star formation. We propose that the main interaction is too young (4×10^7 yr) to have driven much gas accretion to the nuclear regions yet and that the giant clouds that are present in the disks are too young to have produced many new stars.

The kinematic and morphological disturbances observed in this interacting galaxy pair will be used to constrain the relative orbits in Paper II, in which we model in some detail the tidal response of each galaxy to the recent encounter.

We thank our many colleagues at the NRAO in Socorro for their help in bringing this project to a successful end, notably Gareth Hunt for his efforts to straighten out FILLM and for developing the extra routine in CLCOR to correct for the fringe rate, Phil Diamond for his help with FRING and CVEL, and Bill Junor for his relentless troubleshooting.

We are also grateful to Hans-Jörg Deeg for his expert help in obtaining and calibrating the CCD images, and the Director of Capilla Peak Observatory, which is operated by the Institute for Astrophysics of the University of New Mexico, for allocating several nights at short notice. We thank Vera Rubin and Kent Ford for their optical images and Vera Rubin, Kirk Borne, and Charles Peterson for the spectroscopic (unpublished) data. Vassar students Chad Jennings, Lauren Jones, and Laura Ruocco assisted with the optical data reduction.

This work was partially supported by AAS Small Research grants from the American Astronomical Society and NASA to D. M. E. and M. K., and by National Science Foundation grants AST 92-01640 to D. M. E. and B. G. E. and AST 89-14969 to M. K. This research has made use of the NASA/IPAC extragalactic database (NED), which is operated by the Jet Propulsion Laboratory, Caltech, under contract with the National Aeronautics and Space Administration. M. K. also acknowledges a Critical Difference for Women grant from the Ohio State University.

REFERENCES

Appleton, P. N., & Struck-Marcell, C. 1987, ApJ, 318, 103
Baars, J. W. M, Genzel, R., Pauliny-Toth, I. I. K., & Witzel, A. 1977, A&A, 61, 99
Bosma, A. 1978, Ph.D. thesis, Groningen Univ., The Netherlands
Bothun, G. D., Lonsdale, C. J., & Rice, W. 1989, ApJ, 341, 129
Bottinelli, L., Gouguenheim, L., & Paturel, G. 1983, A&A, 113, 61
Brinks, E., & Burton, W. B. 1984, A&A, 141, 195
Condon, J. J. 1983, ApJS, 53, 459
———. 1992, ARA&A, 30, 595
Corwin, H. G., de Vaucouleurs, A., & de Vaucouleurs, G. 1985, Southern Galaxy Catalogue, Univ. of Texas Monographs in Astronomy, No. 4
de Vaucouleurs, G., & Buta, R. 1980, AJ, 85, 637
de Vaucouleurs, G., de Vaucouleurs, A., Corwin, H. G., Jr., Buta, R. J., Paturel, G., & Fouqué, P. 1991, Third Reference Catalogue of Bright Galaxies (New York: Springer)
Dickey, J. H., Hanson, M. M., & Helou, G. 1990, ApJ, 352, 522
Donner, K. J., Engstrom, S., & Sundelius, B. 1991, A&A, 252, 571
Elmegreen, B. G. 1992, in Interstellar Matter, SAAS FEE Lectures, ed. P. Bartholdi & D. Pfenniger (Berlin: Springer), 157
Elmegreen, B. G., Kaufman, M., & Thomasson, M. 1993, ApJ, 412, 90
Elmegreen, B. G., Sundin, M., Kaufman, M., Brinks, E., & Elmegreen, D. M. 1995, ApJ, 453, 139 (Paper II)
Elmegreen, D. M. 1980, ApJS, 43, 37
Elmegreen, D. M., Elmegreen, B. G., Combes, F., & Bellin, A. D. 1992, A&A, 257, 17
Elmegreen, D. M., Sundin, M., Elmegreen, B., & Sundelius, B. 1991, A&A, 244, 52 (ESES)
Gerber, R. A., Lamb, S. A., & Balsara, D. S. 1992, ApJ, 399, L51
Helou, G., Soifer, B. T., & Rowan-Robinson, M. 1985, ApJ, 298, L7
Hibbard, J., van Gorkom, J., Westpfahl, D., & Kasow, S. 1992, in The Evolution of Galaxies and Their Environment, ed. D. Hollenbach, J. M. Shull, & H. A. Thronson (NASA Conf. Publ. 3190), 367

Howard, S., Keel, W. C., Byrd, G., & Burkey, J. 1993, ApJ, 417, 502
Huang, Z. P., Yin, Q. F., Saslaw, W. C., & Heeschen, D. S. 1994, ApJ, 423, 614
Hummel, E., Pedlar, A., van der Hulst, J. N., & Davies, R. D. 1985, A&AS, 60, 293
Icke, V. 1979, A&A, 78, 21
Irwin, J. A. 1994, ApJ, 429, 618
Irwin, J. A., & Caron, B. L. 1994, in International Conf. on Mass-Transfer Induced Activity in Galaxies, ed. I. Shlosman (Cambridge: Cambridge Univ. Press), 362
Lynds, R., & Toomre, A. 1976, ApJ, 209, 382
Mehringer, D. 1992, VLA Test Memo, No. 161
Mirabel, I. F., Dottori, H., & Lutz, D. 1992, A&A, 256, L19
Mirabel, I. F., Lutz, D., & Maza, J. 1991, A&A, 243, 367
Napier, P. J., Thompson, A. R., & Ekers, R. D. 1983, Proc. IEEE, 71, 1295
Persic, M., & Salucci, P. 1991, ApJ, 368, 60
Reshetnikov, V. P. 1992, Ap&SS, 191, 49
Rubin, V. C., & Ford, W. K., Jr. 1983, ApJ, 271, 556
Sargent, A., & Scoville, N. 1991, ApJ, 366, L1
Schwarz, M. P. 1981, ApJ, 247, 77
Struck-Marcell, C. 1990, AJ, 99, 71
Sundin, M. 1993, Ph.D. thesis, Chalmers Univ. of Technology, Göteburg, Sweden.
Theys, I. J. C., & Spiegel, E. A. 1976, ApJ, 208, 650
———. 1977, ApJ, 212, 616
Van der Hulst, J. M., Kennicutt, R. C., Crane, P. C., & Rots, A. H. 1988, A&A, 195, 38
van der Werf, P. P., Genzel, R., Krabbe, A., Blitez, M., Lutz, D., Drapatz, S., Ward, M. J., & Forbes, D. A. 1993, ApJ, 405, 522
van Driel, W., & Buta, R. J. 1991, A&A, 245, 7
Vila, M. B., Pedlar, A., Davies, R. D., Hummel, E., & Axon, D. J. 1990, MNRAS, 242, 379
Wray, J. D. 1988, The Color Atlas of Galaxies (Cambridge: Cambridge Univ. Press)